WIRELESS HEALTH MONITOR DESIGN

A Thesis
Submitted to the Graduate Faculty
of the
North Dakota State University
of Agriculture and Applied Science

By

Kostyantyn Volodymyrovych Koziy

In Partial Fulfillment
for the Degree of
MASTER OF SCIENCE

Major Department:
Electrical and Computer Engineering

April 2012

Fargo, North Dakota

North Dakota State University
Graduate School

Title

Wireless Health Monitor Design

By

Kostyantyn Volodymyrovych Koziy

The Supervisory Committee certifies that this ***disquisition*** complies with North Dakota State University's regulations and meets the accepted standards for the degree of

MASTER OF SCIENCE
in Electrical and Computer Engineering

SUPERVISORY COMMITTEE:

Jacob Glower
Chair

Mark Schroeder

Roger Green

Nikita Barabanov

Approved:

5/1/2012
Date

Rajesh Katti
Department Chair

ABSTRACT

In this thesis, a Wireless Health Monitor system for novel spacesuit verification and tests is presented. This system monitors the operator's health-related vital parameters and incorporates data acquisition, collecting and processing, wireless transmission, data displaying and logging. Power-saving technics for battery-powered applications are incorporated. A proprietary communication protocol for multi-node wireless network is developed and integrated. An embedded web interface for system control and data monitoring is utilized to achieve platform independence and reliability.

Calculations and simulation results for the algorithms developed for gas flow measurements are presented. Packaging for this system, sensor calibration procedures, final device characteristics, specifications and field test results are described. Finally, future work toward possible device operation, improvement, and additional features is considered.

ACKNOWLEDGMENTS

Electrical engineering has become an integral part of my life when I was twelve. First, like a hobby, and later, after getting necessary skills and background - like a profession. A wish to create stays among the primary entries in my life purpose list, and electrical engineering is a passion for me and a way of self-expression. Although it is rare that projects I have worked on did not have an immediate application, in the few instances where they have not I haven't found much satisfaction in their completion, despite being compensated for my time.

The Wireless Health Monitor project was initiated and funded by The University of North Dakota, as a part of space suit research program, conducted for NASA. The department of Electrical and Computer Engineering of North Dakota State University received part of these funds to design, manufacture and test the unit. If the prototype will meet specification, it will be later built into the space suit life support system for test and verification purposes under different external conditions. So, in this case I can be sure that my work will definitely find its place and application. Probably, nobody is going to use it in real extraterrestrial conditions, at least because non space-grade electronic components were used. But the concepts can later be projected to a more specific design (e.g. combined into a specially designed ASIC).

First of all I would like to thank Dr. Jacob Glower for his trust and belief in my background, professional skills and working attitude, and his decision to entrust this project to me. I appreciate the comparative freedom he gave to me in this work, so I could entirely fulfill myself. And also his general support and help during the entire education process with so many niceties.

Also, want to express my gratitude to Pablo de Leon and Lynn van Broock for their agreement to work with me, interesting and informative meetings and discussions, appreciation

of what was done. I really want to believe that my design has met their expectations, and will be reliable, operate long time and provide with data necessary for their experimental analysis.

I am thankful for Jeff Erickson's help with my (sometimes expanded and complex) component orders, Joel Aslakson for giving me practical experience in working on real industrial projects along with advice relative to common living problems, Dr. Mark Schroeder for inspiring me to start to learn neuroscience and biomedical engineering, Dr. Roger Green for always interesting and exciting conversations about everything, Dr. You for his help with sensor calibration equipment, Curtis Reule for teaching me Mentor Graphics PCB layout software and providing transportation, and Laura Dallmann for the keys from labs.

And of course, thanks a lot to my mother, Olga Koziy, who opened a possibility for me in my first life steps to find my way among so many interests and hobbies, supported all my initiatives, ideas and never told "it doesn't make sense" or "it is wasting of your time".

Finally, I would like to commend many semiconductor manufacturers (Analog Devices, Texas Instruments, Microchip, National Semiconductor, Maxim, KOA and others) for providing me with free samples and information support.

TABLE OF CONTENTS

LIST OF TABLES

Table Page

LIST OF FIGURES

LIST OF ABBREVIATIONS

ADC……analog to digital converter

AFE……..analog front end

API……advanced programmable interface

ARP……Address Resolution Protocol

ASCII……..American Standard Code for Information Interchange

BAT…….Battery voltage

BGA……..ball-grid array

BP…….band-pass (filter)

bpm……..beats per minute

BTP…….Body Temperature

Cap…….capacitor

Comp…….component

CRC……..cyclic redundancy check

CSCA……carrier sense collision avoidance

CSMA……carrier sense multiple access

CTS……...clear to send

DC……direct current

DHCP……Domain Host Control Port

DIV……..divider

DNS……Domain Network Service

EEPROM…….. Electrically Erasable Programmable Read-Only Memory

EMF…….electromagnetic force

EMI……electromagnetic interference

ESR……..equivalent series resistance

FHSS…….frequency hopping spread spectrum

FIFO……first-in first-out (buffer)

FRC……..fast resistor-capacitor (clock)

FW……..Firmware

GHM……Gas Humidity

GPR…….Gas Pressure

GTP……..Gas Temperature

GUI…….Graphical User Interface

HP…….high-pass (filter)

HTTP……hypertext transfer protocol

I^2C……Inter-Integrated Circuit

IC……integrated circuit

ICMP……..Internet Control Message Protocol

ICSP……in-circuit serial programming

ISR……interrupt service routine

LCD……liquid crystal display

LDO…….low-dropout regulator

LED……..light emitting diode

Li-Ion……Lithium Ion (battery)

LP…….low-pass (filter)

LSB……least significant bit

MAC……..Media Access Control

Mat……material

MCU……microcontroller unit

meas……measured

MOSFET……metal oxide semiconductor field-effect transistor

MSB……..most significant bit

NDIR……non-dispersive infrared

NiCd…….Nickel Cadmium (battery)

NiMH……Nickel Metal Hydride (battery)

NV……non-volatile

OEM……original equipment manufacturer

OLED……organic light-emitting diode

op amp……..operational amplifier

OS…….operating system

OSI…… open systems interconnection (basic reference model)

PC…….personal computer

PCB……..printed circuit board

PDA……personal digital assistant

PHY……physical layer

PLL……..phase-locked loop

p-p…….peak-to-peak

PS…….power source

PSRR…….power supply rejection ratio

PUR…….Pulse Rate

PWM……..pulse-width modulation

Quan……..quantity

REF……..reference

rel……relative

Res…….resistor

RF…….radio frequency

RMS……root mean square

ROM……read-only memory

RSSI…….received signal strength indication

RTC……real-time clock

RTD……..resistive temperature detector

RTS……...ready to send

RXD……. receive data

SNR……..signal to noise ratio

SOH…….Start of Heading

SOIC……small-outline integrated circuit

SPI……Serial Peripheral Interface

SPS……samples per second

SPST……..single pole single throw (switch)

STX……..Start of Text

TCP/IP……Transmission Control Protocol/Internet Protocol

TRC……temperature-resistance coefficient

TVS……transient voltage suppressor

TXD……..transmit data

UART……universal asynchronous receiver/transmitter

UDP……User Datagram Protocol

USB……universal serial bus

UWB……ultra-wide band

vol……...…volume

WBAN……Wireless Body Area Network

WHM……Wireless Health Monitor

LIST OF APPENDIX TABLES

LIST OF APPENDIX FIGURES

CHAPTER 1. INTRODUCTION AND PREVIOUS WORK

1.1. Introduction

Modern spacesuits represent very complex technically sophisticated hardware. Even so, there remain many uncertainties and problems to solve in their design, which in some cases must be solved using intuition. Challenges include (but are not limited to) maintaining air pressure, regulating temperature and humidity, regulating the composition of the breathing gas mixture, and developing a convenient, human-friendly environment to name a few [1].

Novel spacesuits require considerable time and effort to design. Once designed, even more time must be spent to test, verify, and possibly make necessary changes in the design. Test conditions can be extreme (e.g. organized in Antarctica) and expensive. During the test procedures, a number of human-relative parameters must be collected simultaneously and stored for future analysis. This may be for a single or multiple spacesuits operated at the same time.

During the course of this work, several meetings with spacesuit engineers took place along with discussions about their requirements and possible solutions. After these meetings, it was decided to use a "Base-Nodes" concept. With this concept, a WHM system will include the main base station module (hereinafter referred to as the Base), and a number of remote nodes (referred to as Nodes) built into the spacesuits. Information from a sensor set will be collected, processed and temporally stored by the Nodes. Later, this information is transmitted and consequently received by the Base, which is also responsible for monitoring and logging the data.

Several design options were rejected early on in this project. First, an infra-red light communications channel was rejected due to the need for a line of sight between the Base and Nodes – which may not always be the case – as well as a limit operating range. Instead, a

wireless RF channel is used. Second, the use of only node modules was rejected. This approach would require removable memory (e.g. flash memory card) in each Node. The acquired data would be stored on this removable memory, which would be been copied to and analyzed at a later date. This solution does have advantages. By eliminating the radio transmitter, power consumption is reduced and the possibility of data loss due to radio link failures is avoided. However, this approach lacks real-time monitoring, which the spacesuit engineers would like for testing and experiment activities.

1.2. WHM Requirements - Scope of Work

While this project is not related to a spacesuit design, an engineer needs to know the basic spacesuit operation parameters to define where to mount the Nodes and sensors as well as their maximum allowable dimensions and weight. To design the WMH system, the parameters which need to be measured, their range, and the required sampling rate must be specified. This information is necessary for the proper selection of sensor types and signal conditioning circuit design, and for algorithm development.

Most of the requirements for the WHM project were defined during the meetings with the spacesuit design team at the University of North Dakota. When additional information was needed, this was obtained from publications about modern US and Russian spacesuits and their design trends, and when that failed - my own intuition. These requirements are summarized in Table 1. More details for how these parameters were obtained are presented in Chapter 2.

1.3. Thesis Organization

This thesis is organized as follows. In Chapter 1, the motivation for the WHM project is presented along with a summary of the system requirements. In Chapter 2, a detailed explanation of the origin of these systems requirements is presented along with a brief summary of previous

work on spacesuit instrumentation. In Chapter 3, the design of the portion of the WHM project within the spacesuit, termed a Node, is presented including components selection, schematic design and simulation. In Chapter 4, a Node PCB layout, enclosure design and MCU firmware operation are described. Chapter 5 presents a Base unit, which monitors the Nodes, saves, and displays the data. This includes schematic, layout and firmware design. In Chapter 6, validation, test results, conclusions and future work are presented. GUI and quick starting guide, project budget and sensor calibration procedures are then presented in the appendices A, B and C.

Table 1. The Wireless Health Monitor project requirements.

Parameter Name	**Units**	**Range / Value**	**Accuracy**	**Precision**
Node-Base interface	-	Radio channel, star	-	-
Node-Base distance range	m	>3000	-	-
Max supported number of Nodes	#	10	-	-
Node-specific:				
Body Temperature meas.	°C	+25..+45	0.5	0.1
Body Surrounding Pressure meas.	kPa	20..115	0.5	0.1
Oxygen concentration meas.	% (vol.)	0..100	0.5	0.1
Carbon Dioxide concentration meas.	% (vol.)	0..5	0.01	0.01
Inner volume Temperature meas.	°C	-10..+50	1	0.1
Inner volume Humidity meas.	% (rel.)	0..100	2	1
Heartbeat rate meas.	# per min	40..240	5	1
Hemoglobin oxygenation meas.	%	0..100	3	1
Respiration rate meas.	# per min	0..60	N/A	1
Battery voltage meas.	V	1.8..4.8	0.05	0.01
Sensor Data update period	s	5	0.5	-
Power supply nominal voltage	V	1.8..4.8	-	-
Min off-line operation time	hr.	>10	-	-
Max linear dimensions, LxWxH	mm	100x70x35	-	-
Max unit weight	g	200	-	-
Base-specific:				
Power supply nominal voltage	V	5..12	-	-
Data and control interface	-	Ethernet, Web	-	-
Max linear dimensions, LxWxH	mm	200x100x80	-	-
Max unit weight	g	300	-	-

CHAPTER 2. SYSTEM REQUIREMENTS AND PREVIOUS WORK

In this chapter, a summary of previous work on developing instrumentation systems for spacesuits is presented. The measurement parameters of interest along with their desired sampling rate are then presented.

2.1. Node Requirements

One requirement for an extravehicular spacesuit is to regulate the temperature of the inner volume. External temperatures can be extreme – ranging from -127 to +121°C. For a human to function and survive, however, his/her body temperature must be kept between 27 and 42 °C, with at a nominal value of 36.6 °C [2]. Without heat removal, the spacesuit inner volume temperature will reach equilibrium at approximately 37 °C under normal conditions, which will reduce the convenience and efficiency of an astronaut's work.

A second requirement is to regulate air pressure. At least 21 kPa are needed to support life, but higher pressure is usually used to reduce the likelihood of decompression sickness.

A third requirement is to regulate the composition of the air in the spacesuit. The life support system of a spacesuit must provide oxygen or an appropriate gas mixture (such as a helium/oxygen combination) from external containers for breathing. Without oxygen, a human dies within 5-7 minutes due to irreversible changes in brain tissues. In addition, the spacesuit must regulate the amount of carbon dioxide (CO_2) along with odors from breathing volume. This is often done using special cartridges with charcoal filters and either LiOH or regenerable metal oxide adsorbent. Under the normal pressure (101.3 kPa), CO_2 concentration must not exceed 0.1% vol. (according to ASHRAE/OSHA) for normal human health state. CO_2 concentrations of up to 3% cause air lack feeling, and above 5% leads to intoxication and loss of consciousness [3].

Inner humidity control is also important. Its allowable range is between 15% and 80% [3]. An air dehumidifier must be utilized to remove extra water – which is produced by the operator's perspiration and respiration.

With this information, the requirements for the parameters to be measured and their ranges are:

- Body temperature (25…45 °C),
- Body surrounding pressure (20…115 kPa),
- Oxygen concentration (0…100% vol.),
- Carbon dioxide concentration (0…5% vol.),
- Inner spacesuit temperature (-10…50 °C), and
- Relative humidity (0…99%).

With the exception of the oxygen sensor, these requirements allow for the selection of an appropriate sensor. With the oxygen sensors, a problem was encountered: there are no compact sensors available on market for such a wide concentration range. Instead, a sensor that is designed to measure 0 to 21% vol. O_2, was used. For higher concentrations, this sensor still provides readings, but its life time is reduced.

In addition to parameters listed above, it is required to monitor

- Respiration rate,
- Pulse rate, and
- Hemoglobin oxygenation level.

This information is vital to create a more complete picture of human's health and its change over the time of an experiment.

2.1.1. Respiration rate

A human's respiratory system provides gas exchange surfaces of a distensible lungs with a warmed, humidified, and cleaned breathing gas mixture. Oxygen is diffused by the blood circulation through the alveoli from this mixture and CO_2 is removed from the blood [4]. For a normal adult at rest, the respiration rate is 15-20 per minute. This breathing frequency as well as its depth and rhythm can vary due to exercise stress, the amount of oxygen in the air, an increase in the body surround temperature, as well as a number of illnesses. In this project, full breathing cycles are measured over a range of 0 to 60 cycles per minute. With this measurement, the maximum and minimum intervals between cycles are calculated along with additional information about breathing volume by monitoring the chest displacement level.

2.1.2. Heartbeat rate

Heartbeat rate (or pulse rate, if there is no damage to circulatory system) reflects the electrical activity of specialized cells of heart auricles, located in Keith-Flack node. Spontaneous pulses in this node are distributed through specialized fibers. These provoke a contraction of auricle muscles, pushing the blood to the ventricles, which drives the blood to the arteries. The whole system works autonomously, synchronously, rhythmically, and reliably [5]. The heart operates like a pump that transports blood through the vessels, delivering it to various tissues and saturating them with oxygen.

At rest, a person's pulse rate depends on many factors including the person's age, psychological state, body temperature, body build and weight, nutrition etc. For most adults it is equal to 70 bpm [5]. For athletes and specially trained individuals, it can be lower. High pulse rates (tachycardia) can happen due to an increased physical load, due to a loss of efficiency of the heart and lungs, or due to the side effects of particular drugs. Low pulse rates (bradycardia),

which are usually associated with a giddy feel, tiredness and weakness, may indicate heart muscle injury, hypothermia or other illnesses. If left untreated, the heart may completely stop. From this, the range of heart rates that the WHM device must be able to monitor can be determined: 40 to 240 bpm.

2.1.3. Hemoglobin oxygenation level

Oxygen levels in blood are fairly small - less than 2%. This oxygen is dissolved in blood plasma and can be delivered directly from lungs to various tissues. The most vital portion of a molecular oxygen is transported by the hemoglobin molecule, which consists of protein globin and an iron group. The process of O_2 connection to hemoglobin is called oxygenation (in spite of the fact that iron doesn't change its valence). In humans, 100ml of blood normally contains 15 grams of hemoglobin that can transport about 21ml of oxygen (only 5-6ml of which will be accepted by tissues). This is termed the blood oxygen capacity. The degree of oxygenation represents a percentage of the blood oxygen capacity in use. It depends on partial pressure of O_2 and the concentration of CO_2 in breathing volume, and blood temperature [6].

The lowering of oxygenation level is a sign of hypoxia (oxygen starvation). This may result due to the reduction of oxygen partial pressure (exogenic), due to the lowering of body temperature, intoxication with carbon monoxide (hematic), high dryness, inadequate blood supply (circulatory), excessive muscle overload, and several other factors. The symptoms of hypoxia are an increase in the rate and depth of respiration and higher pulse rates. If prolonged, this can result in various organ disorders and death.

To monitor the health of the operator, the oxygenation level will be monitored over the range of 0% to 100%.

Once the ranges of each sensor are defined, proper sensor types can be selected and initial

Node description can be developed. The location of each particular sensor will also depend on the sensor type, its measurement method, and its physical dimensions.

The selection of the sensor type is based on the required parameter range, precision and accuracy, power consumption, size, and interface. In addition, every sensor must be operable within the system's general operation conditions (e.g. the oxygen sensor must be able to withstand the operating temperature and pressure ranges). Cost is of minimal importance in this project due to the small production quantity (only 5 devices were required to be assembled.) Component definitions will be provided in the next chapter along with the hardware design flow and operation.

To improve system reliability and consistency, the number of externally connected (wireless or wired) modules are minimized with as many sensors and controls being placed within the Node board as is physically and operationally possible. The only external components connected to the node module were respiration, body temperature and pulse rate sensors along with power supply and antenna connection. Figure 1 shows a general WHM system organization.

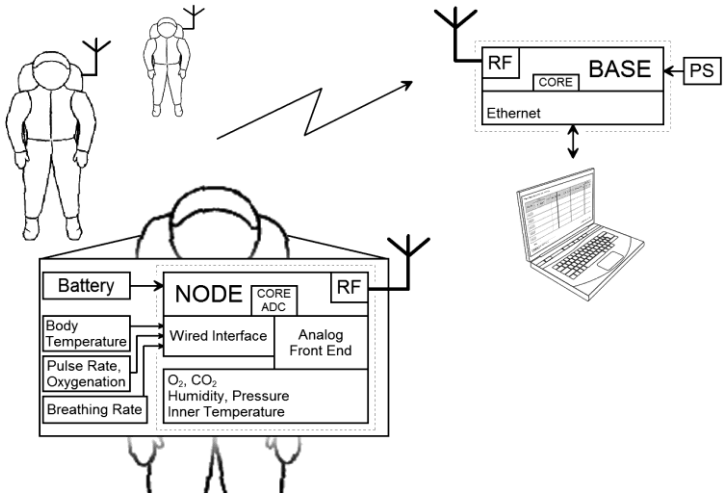

Figure 1. The WHM system general organization and block interconnection.

An alternative solution to wired connection would be to use a wireless sensor array along with a local base station which is capable of receiving data within the spacesuit, and then collect and retransmit it to the main base station. In this case, every sensor (or group of sensors) must have its own low-power transmitter, conditioning circuit, and power supply as presented in Figure 2. This system organization is called Wireless Body Area Network (WBAN) and it is widely used in health monitoring applications [7]-[8]. It gives flexibility in sensor mounting location and durability in addition to other advantages inherent to wireless solution.

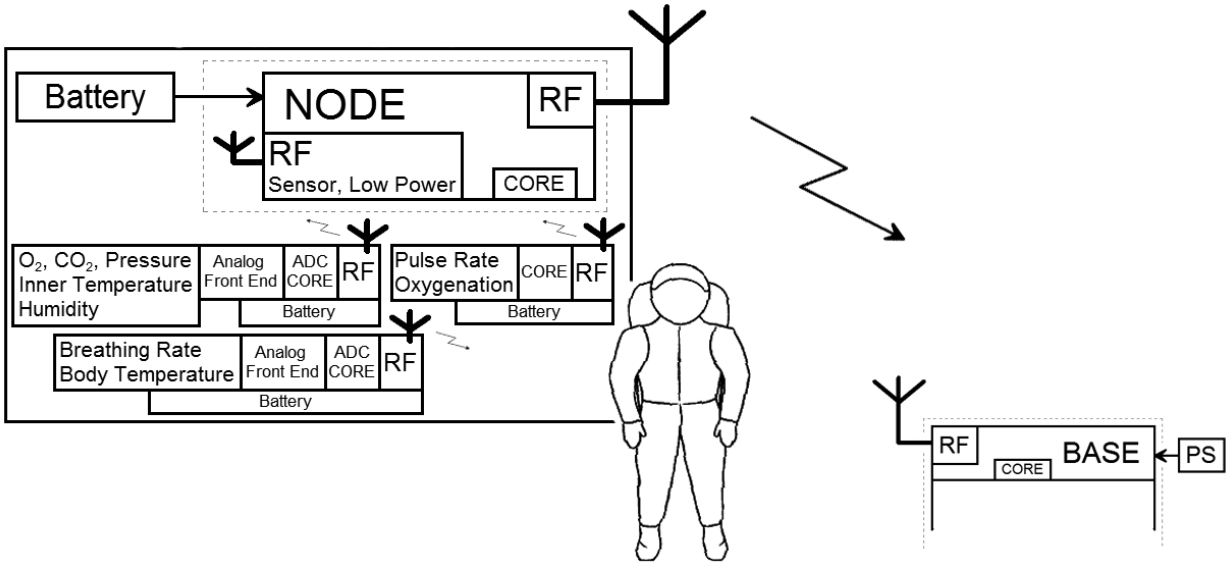

Figure 2. The overview of the WHM system based on WBAN solution.

This solution is much more sensitive to interference and may result in substantial radio signal attenuation due to the human's tissues in a wide frequency range [9], which leads to possible data loss and/or delays. It also reduces the reliability of the entire system due to the need of additional components required for every sensor node and adds complication of maintenance, troubleshooting and power supply distribution.

For spacesuit tests on the ground, a wired sensor solution will work. To accommodate

the possibility of adding local wireless sensors in future versions, the system designed herein should (and does) allow for such sensors with little or no changes in hardware: only firmware changes are required. Unused internal/external sensors then can be disconnected through firmware to save power.

Wireless radio frequency communication is not the only possible solution for WBAN. For example, bone acoustic conductivity may also be used for low-speed information delivery from sensor node array to the local base [10].

Wireless network topology is a large field in itself. In this project, due to the small number of nodes involved, there are two major ways to create the link between nodes and the Base are of primary interest: star and tree configuration.

In star configuration (Figure 3), the Node can only communicate directly with the Base. This is the most efficient solution from a software standpoint because every Node is only responsible for transmitting its own data. The Node transmitter can be woken, data packages sent, acknowledgement from the Base received (if used), and then the Node can be put back to sleep again. Typically, a star configuration has the least power consumption, especially if no feedback is expected from the Base (e.g. acknowledgment, control signals). Synchronization is relatively simple as well, as the only concern is a simultaneous transmission start of two or more nodes. This problem can be overcome by using an acknowledgement and/or listen for the channel before sending data, as is implemented in CSCA algorithm.

A star network topology has some limitations, however. In Figure 3, Node #1 and #2 can successfully reach the base station. The signal from Node #3 is lost, however, due to the obstacle. Data packets from Node #4 also can't be received due to being out of range. To overcome these problems, a tree and/or mesh network configuration can be implemented. Such a

configuration increases the power consumption, complicates the communication protocol, and increases radio channel use.

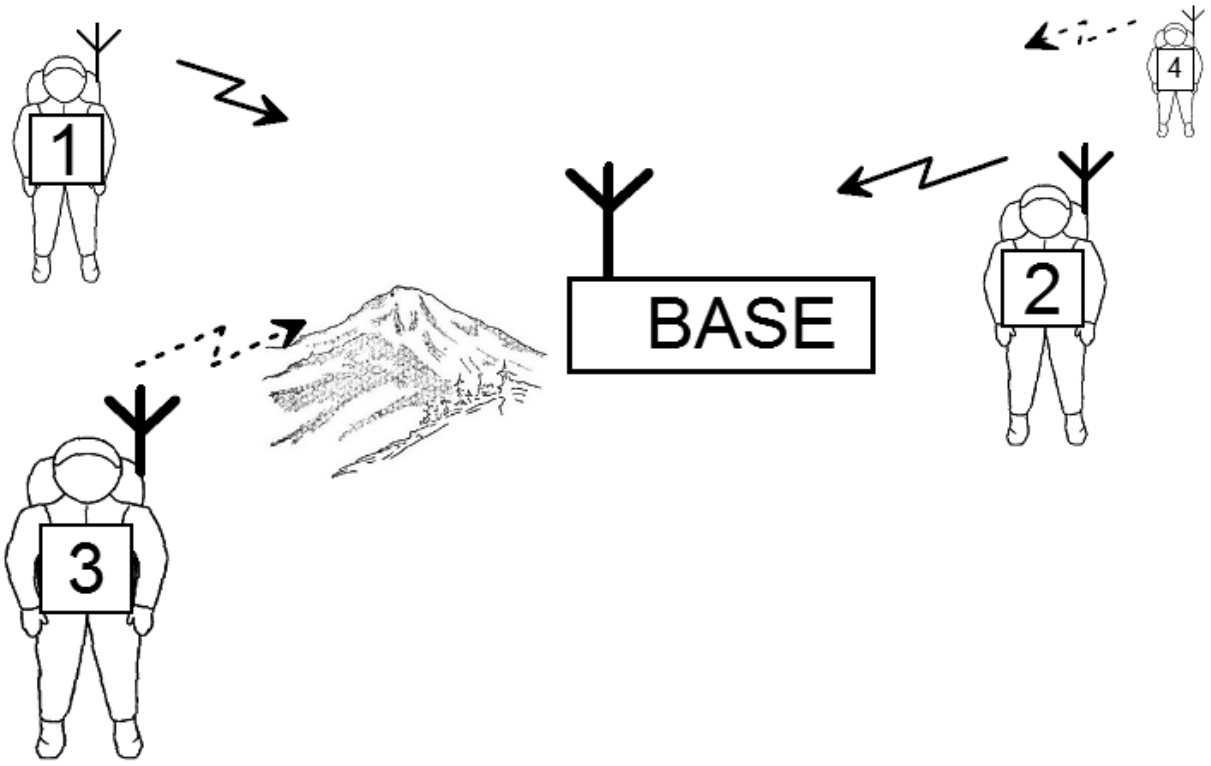

Figure 3. Star network configuration in the WHM system.

In a tree wireless network configuration, every node is capable of not only transmitting its own information, but also operates as a mediator and retransmitter for the other nodes. As an example of using a tree topology, consider one applied to the WHM system as shown on Figure 4. As can be seen, Node #3 (it is called the edge node) can route its message through the Node #1, bypassing the obstacle. Nodes #4 and #5 can send their messages through the Node #2, which clearly extends the maximum network range in particular node location. In doing so, battery life for the intermediate nodes will be significantly reduced, and power consumption calculation for such network organizations requires extensive simulation to cover all possible node locations and involves the probability consideration.

There are several problems with a tree network, however. First, the receivers have to be switched on for a longer period of time. This is necessary since each Node may have to help deliver a message to the Base. Second, the code is considerably more complex. For example, considerable work has been published regarding synchronization for all of the Node transmission events, mostly directed to minimize node wakeful state time and retransmission counts, along with ensuring a message delivery with minimum latency and avoiding package losses [11].

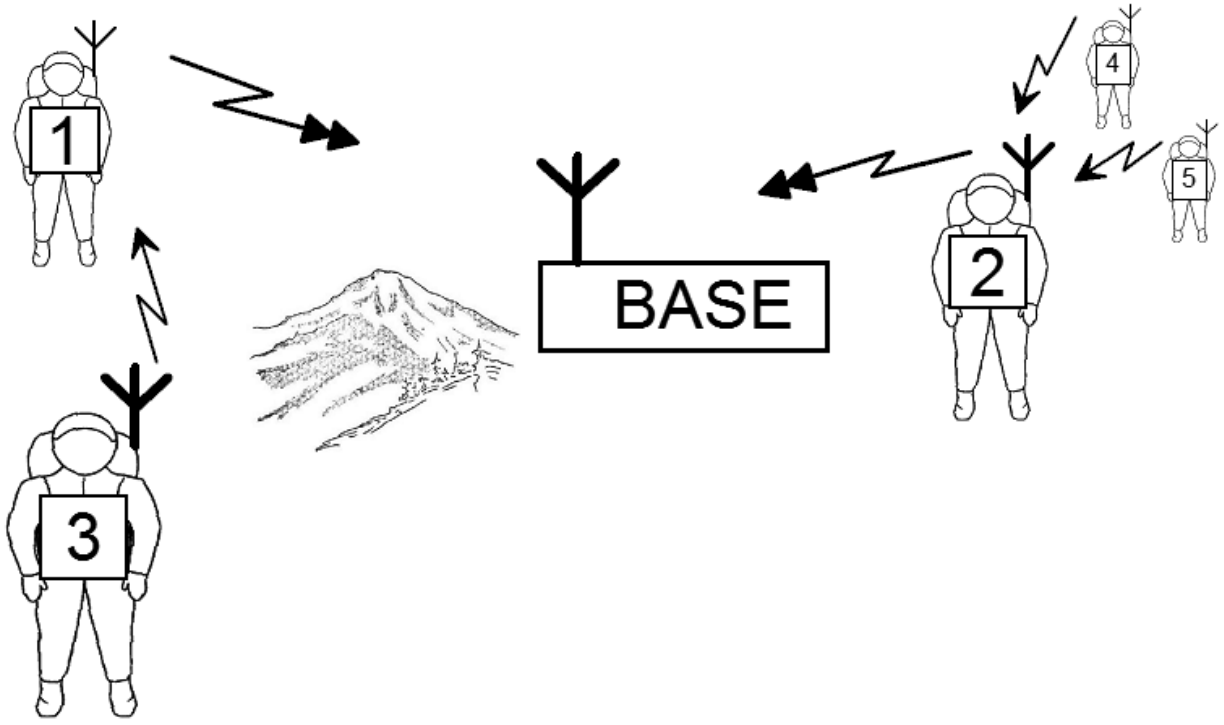

Figure 4. Tree network configuration used in the WHM system.

In the WHM project, a star topology was used due to the small number of nodes, limited operation range, and low power consumption requirements. However, because the topology can be changed at any time with a software change alone, transition to a more advanced topology at a future date is possible.

Communications from the Node to the Base is as follows. Information from every sensor

is sent to the Base asynchronously at a rate which depends on sensor type and measured parameter. For example, the body temperature sensor is processed every second whereas respiration rates are processed at a slower rate.

Once data is processed, the most recent data is placed in a packet and transmitted to the Base every 5 seconds – which is adjustable in software. Data which is processed at a faster rate is averaged while data which is processed at a slower rate use the most recent calculated values.

2.1.4. Sensor accuracy

For the respiration rate measurement, accuracy is determined as a maximum bias from a real breathing cycle number, determined under different conditions experimentally. RMS (root mean square) error may also be used for the accuracy specification in this case.

For the chest displacement measurement method used in this project, readings can be affected by the operator's state (e.g. rest, speech, walk, hands and body motion etc.) While these factors can be taken into account to improve the respiration rate measurement [12]-[13], this work assumes the operator is at rest.

Heartbeat rate and hemoglobin oxygenation measurement accuracy is taken from the OEM module datasheet that is utilized in this project. Such modules are widely used in medical applications and provide a good balance between accuracy, size, power consumption and price [14].

2.1.5. Other Node requirements

Maximum achievable distance range between the Node and the base station (besides the antenna type, operation frequency, transmitter power and receiver sensitivity) depends on many factors: obstacles along with their structure, size and location, other transmitters in close proximity and their operation mode, antenna orientation etc. To simplify computations, line-of-

sight was assumed for parameter in Table 1.

The base station must use power supply adapter for the specified voltage range. The Node may also use an adapter for developing and debugging purposes, but Nodes are intended to be used with either two AA 1.2-1.5V batteries (NiCd, NiMH, and Alkaline) or one 3.6V Li-Ion battery. Battery holder is mounted separately from the Node unit according to final discussion with spacesuit design team.

In addition to these requirements, the WHM device must not be damaged if the operator plugs a sensor into the wrong connector or if reverse polarity is applied to the power input. During normal operation, the user must be notified about sensor failure and/or low battery condition through the web interface. The WHM should also include features that prevent data corruption due to user errors, data corruption due to problems with the power supply, protection from electrostatic discharge, and protection from power line transients.

Designing the WHM to be tolerant to radiation, extensive vibration and acceleration is considered to be beyond the scope of this work.

Various other parameters which some spacesuits have monitored are also considered to be beyond the scope of this work. These include:

- An electrocardiography (heart biopotentials within the thoracic area, with amplitude of up to 2.5mV and spectral range 0.5...40Hz),
- Seismic cardiography (vibration of thoracic cage in frequency range of up to 18Hz, which follows the heart mechanical work),
- Electroencephalogram (brain activity biopotentials with up to 100uV amplitude),
- Electrooculogram (bulb of eye motion), and
- Skin galvanic reaction (skin resistance variation within 2...100kΩ).

These parameters can be added later to the WHM system, but this would require significant hardware and software modifications.

2.1.6 Node location in the space suit

The Node is installed inside a spacesuit. During discussions with the spacesuit engineers at UND, it was concluded that the best place for mounting would be in the back side of the helmet for several reasons. First, it shortens the length of an RF cable to an external antenna. Second, to analyze the breathing volume for gas concentrations it is important to install gas sensors close to the breathing area, but not directly in the breathing path to avoid abrupt changes in gas sensor readings. This location also provides a relatively short distance to the operator's ears (for pulse rate and oxygenation sensor) and chest (for body temperature and respiration sensors).

The recommended antenna is an omni-polar standard ½ wavelength antenna, mounted on the top of the helmet or on the backpack of the spacesuit. A custom antenna design was not required and consequently not covered in this work. However, future antenna designs could hide the antenna inside the helmet or make the antenna as integral part of it. This will reduce the probability of damaging the antenna when operating near an obstacle, such as a hatch [15].

The overall Node outer dimensions must be as small as possible. The maximum size of completely assembled device including external connectors and controls must not exceed 100x70x35mm. The enclosure shape in the first prototype was designed according to node internal component placements, and later can be redesigned and customized for a particular location in a spacesuit. Weight must also be minimized and not exceed 200 g (without battery, external sensors and connection cords).

2.2. Base Requirements

The Base (Figure 5) must be able to receive data messages from all nodes in range and process them through its RF engine, check message consistency, sort and store the messages, and retrieve them upon request. This communication may be unidirectional (when there is no feedback from the base station) or bidirectional (when the Base may send messages to the nodes). The former method reduces the power consumption for each Node, but takes away the node control capability. The latter method allows the operator to remotely adjust node functions such as the sampling rate, the gas sampling fan, etc. This increases power consumption, however, due to prolonged receiver operation and additional transmission packets.

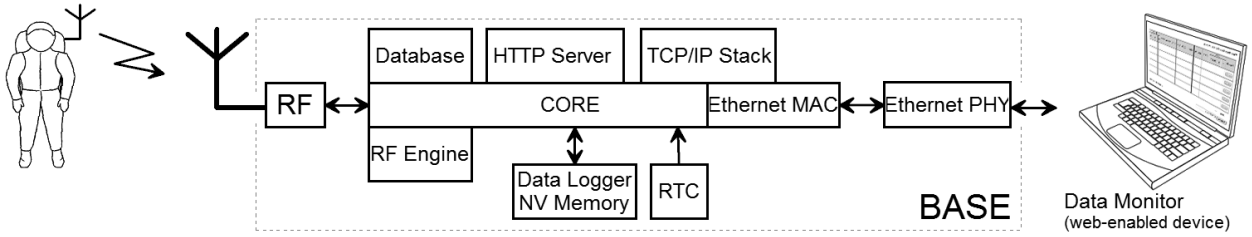

Figure 5. The Base unit internal structure overview and connection with data monitor.

The database must store received information, either with or without a time stamp. To increase reliability and minimize the influence from the user, the Base was designed to incorporate all necessary blocks within one unit, including built-in logging using non-volatile memory. This memory allows the Base to store and retrieve messages at any time, making the recent data independent from data monitor device/application at a cost of limiting the logging time depth. In the current firmware, logging is done only at the Base (web-enabled device) using local file access.

A Real Time Clock module is needed to track message arrival times and to create a timestamp, which is recorded in the database along with the sensor data. This module makes the

Base a stand-alone unit, independent from the external monitor. However, this feature has not been incorporated into the firmware. Instead, time logging is done by the external system and is available only during data logging.

There are several options for the user interface. A standalone solution may include a built-in graphical or text LCD display and control buttons as presented in Figure 6, and an external link to flash memory, or a PC for data logging purposes. The first solution makes this device completely encapsulated and very reliable. However, it will limit the convenience of use due to a small screen and buttons. A second solution uses a standard interface such as UART, USB or Ethernet, and creates a link between the Base and PC or portable device. This approach opens a wide possibility for creating a very convenient graphical user interface and data processing tools, but is limited by the PC operating system. It also reduces the reliability due to future changes in the OS, and requires OS API programming knowledge, complicating system updates.

The user interface selected for the WHM project is to use an embedded web server and Ethernet solution as presented in Figure 6. This avoids problems with supporting future (unknown) changes in the PC operating system. It also maintains the all-in-one concept and makes it easy to expand the user interface and simplifies update process.

The web server operates on the same core cooperatively with the other program blocks. The server responds to HTTP (hypertext transport protocol) requests that come from client web browsers which are connected through the Ethernet network. In our particular application, the server provides a bridge between the user, base station control, and node database information: selective data can be transferred and displayed on a client web page. In addition, user commands can be directed to the Base core for execution.

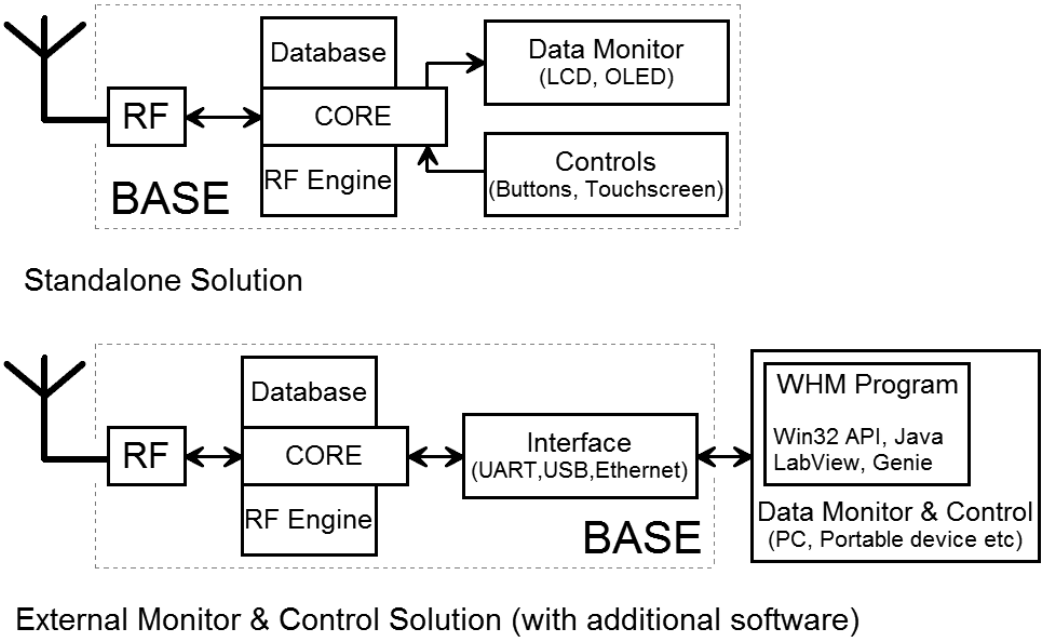

Figure 6. Alternative data displaying and control solution for the WHM Base unit.

The Ethernet network communication includes TCP/IP (Transmission Control Protocol/Internet Protocol) along with MAC (Media Access Control), which are transport and network layer protocols in the OSI structure. They are responsible for making the WHM web server reachable for web-enabled devices in a network, packing the data, coding it, and adding information required for routing and delivery. PHY is a physical layer for the Ethernet connection that is responsible for physical analog access to the link.

2.3. Previous Work

The WHM project involves sensing, processing and collecting of human's vital functions. Several other works report similar activities - a few of which are described herein.

To accommodate the monitoring of human vital parameters in a long-term way, the CodeBlue project was initiated at Harvard University [16]. This project involves the use of sensor-specific boards (pulse oximeter, electrocardiograph, and electromyograph) and MicaZ and Telos low-power transmitters (motes), which can be mounted on a patient's body, and

operate in a special mesh network. Information is delivered to the medical personal through PDAs or computers with pre-installed software. This makes it possible to monitor parameters such as pulse rate, hemoglobin oxygenation, patient movement etc. The network architecture of this system is shown on Figure 7. It involves the use of additional motes that support infrastructure, and are responsible to deliver information to/from sensor motes.

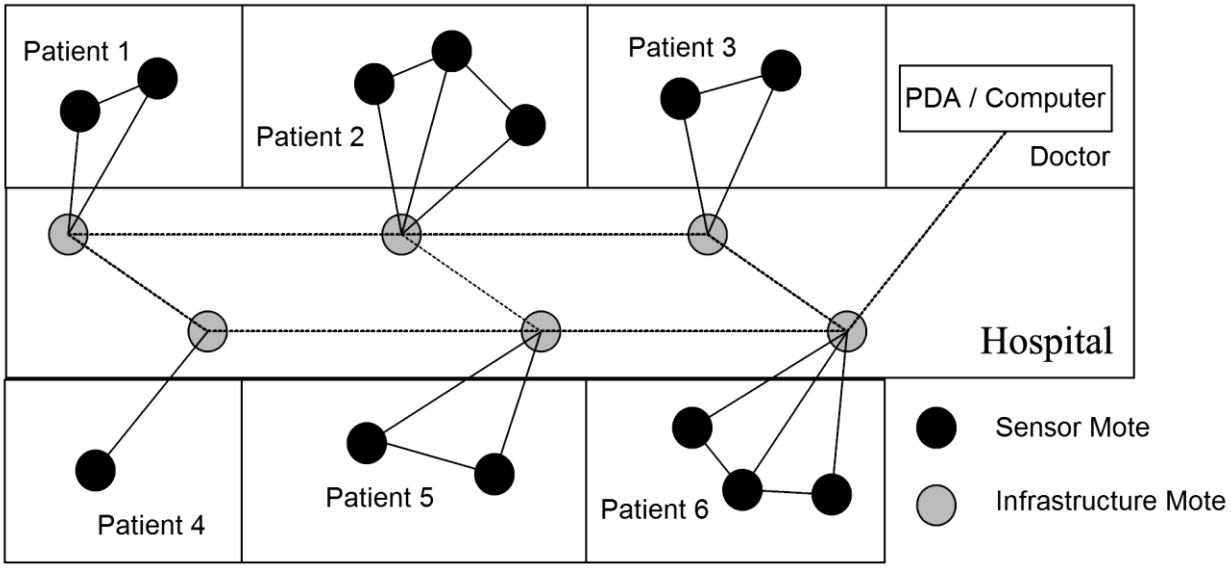

Figure 7. CodeBlue wireless sensor network organization.

The CodeBlue network uses the publish-subscribe mechanism that is based on Adaptive Demand-Drive Multicast Routing protocol. According to it, sensor motes transmit information only under specific conditions that can be remotely programmed by the user. These conditions can be reaching the preset upper and lower thresholds, a specific time interval, etc. Each node in the network is informed about the best path to deliver the information from the sensor mote to the base station, and this routing is updated from time to time to accommodate possible changes in wireless channel (e.g. patient relocation, additional sensor mounting etc.) In addition, the protocol is able to deliver the information about the approximate patient location displayed using a graphical user interface.

Another system for wireless health monitoring was presented by the group of students in the University of California, and is called CustoMed [17]. This design minimizes system customization and reconfiguration time to accommodate the patient's needs, making this process simple enough for even non-engineering staff. It supports various sensor types, including pressure, galvanic skin response, flex, and temperature. Fast configuration can be done by the physician in hardware (connecting necessary external sensors and blocks) and in software (downloading appropriate firmware that can be generated by special tool, which allows picking up a specific code variation). The authors claim that patient monitoring can now be completed in a few minutes in the doctor's office using this approach.

Med Node is another wireless health monitoring system. Med Node is a battery-powered device that contains low-power transmitters as well as a processor and conditional circuit to support analog and digital inputs from various sensor types. Every sensor or sensor group can be connected to Med Node and then placed anywhere on human's body. One mote operates like an infrastructural device, collecting information from other motes and transmitting it to a Pocket PC through the UART interface. Software on the Pocket PC is responsible to display the sensor data and control/configure sensor nodes. The fast configuration concept was verified through the number of tests [17].

Researchers at the University of Texas in Dallas designed a patient wireless health monitor system which is capable of measuring and displaying vital sign information in real-time [18]. It is intended to be used in hospitals and homes and removes the inconvenience and limitation of hard wired solution. Nodes in this wireless network are self-aware and self-configurable. A special dual-router algorithm was introduced in which infrastructure nodes operate in pairs to improve message delivery probability and reduce the number of

retransmission cycles.

The system developed made use of energy harvesting and energy saving. A special power saving algorithm was used to keep nodes in sleep mode as long as possible while avoiding the loss of data packets. The router obtained energy from small solar panels illuminated by fluorescent lamps. Plans to use piezoelectric vibration in future version were also mentioned.

Nodes have been tested to operate with different sensors including electrocardiograms and blood pressure. A graphical user interface displays data on the physician's computer connected to the base station. The absence of data packet loss and easy configuration were outlined.

2.4. Summary

Even though there is considerable work on wireless medical data collection for hospitals and private use, these solutions do not work for aerospace applications due to the relatively short link operation range and a limited number of acquired life-vital parameters.

Some sources do describe health monitoring techniques used in traditional spacesuits, including measurement methods, sensor types and location on a human's body, health parameters and their ranges [19]. These solutions do not work for our application, however, due to the limited amount of information about them and very brief and general system description, wired connectivity, relatively wide spreading and single spacesuit support.

As a result, there is a need for a custom wireless health monitoring system that can simultaneously serve up to five spacesuits. The following chapters describe the device which was developed to meet this need.

CHAPTER 3. NODE HARDWARE DESIGN AND OPERATION

3.1. Introduction

This chapter explains component definitions and schematic design procedures, along with operation principles, calculations and simulation results (when appropriate) for the Node hardware. The purpose, function, and connections of every block or group of blocks presented in Figure 8 will be explained first in a general way, then in details.

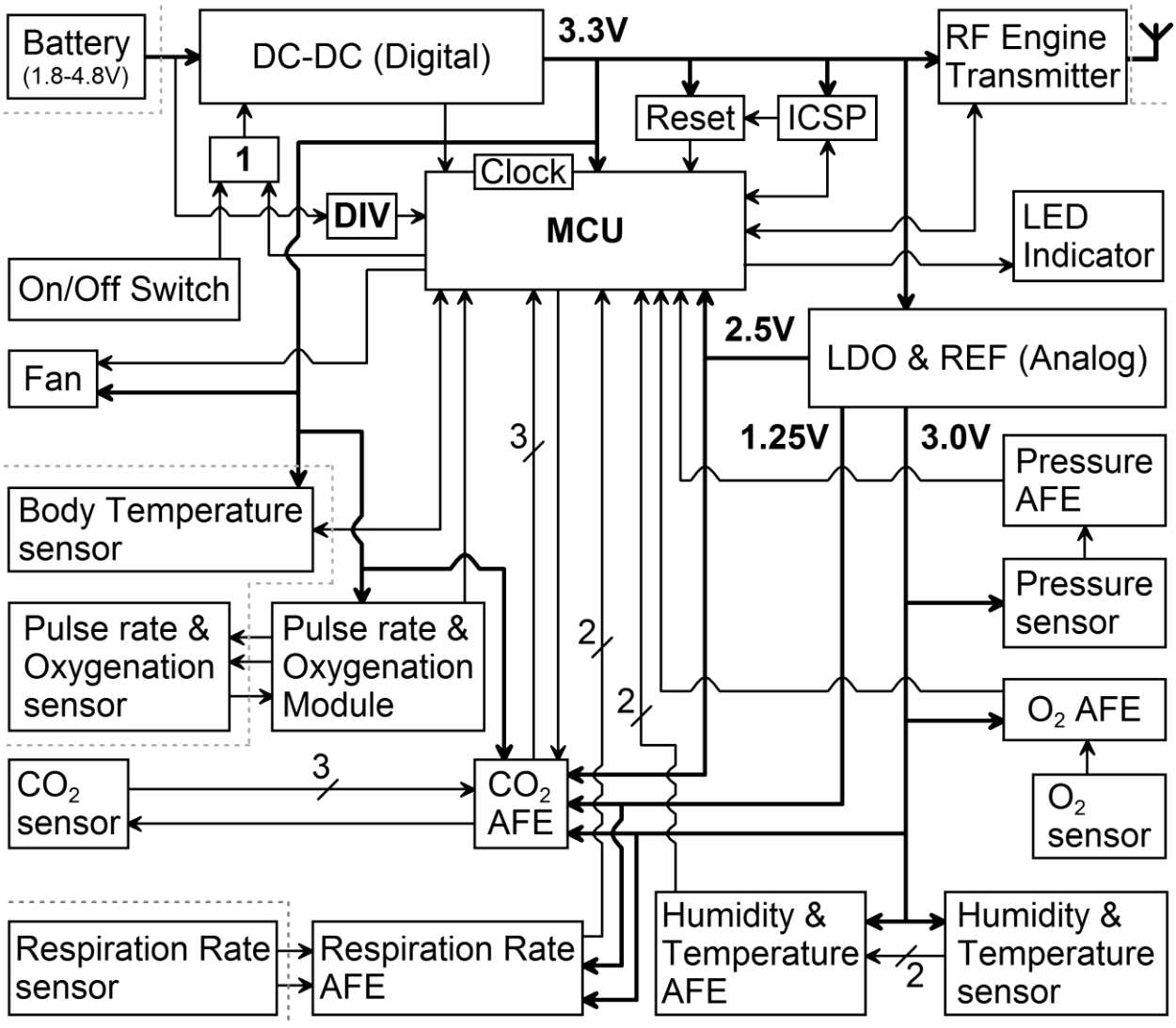

Figure 8. The block diagram of the Node unit circuit.

The Node unit is responsible for sensor signal transducing, data collection initial

processing, and transmitting. Since this is a battery powered device, powers saving techniques are paramount. These include a high-efficiency power supply design, a low-power microcontroller, and the selection of low power sensors and transmitters. For reliability, the Node units must also be protected from battery reverse polarity and ESD. Figure 8 depicts the block diagram of the Node electronic circuit, including its externally connected sensors.

3.2. Power Supply

The Battery block represents power supply. For flexible operation, the WHD can operate with a supply between 1.8V and 4.8V, allowing one to use two NiCd/NiMH batteries, one Li-Ion battery, or two alkaline batteries. To save battery life, the Node also monitors battery voltage and switches off the device if the battery is close to being completely discharged.

3.2.1. Battery selection

Modern rechargeable batteries are characterized by a high energy density, a large number of charge/discharge cycles, small sizes and long life. NiCd (nickel–cadmium) batteries have been used since the year 1950. These batteries have comparably low price, provide long lifecycle and high discharge currents in addition to wide operation temperature range (-40…+60 °C) and the shortest charge time (1 hr.) among other battery types. However they have low energy density (45...80 W/kg), high self-discharge and contain hazardous substances making them potentially dangerous for the environment. NiCd rechargeable batteries are widely used in transmitters, biological and medical equipment, professional camcorders and cameras, electric tools.

NiMH (nickel–metal hydride) elements have higher energy density (60…120 W/kg), but fewer lifecycles (300…500 cycles). They are relatively safe for the environment, and found their use in portable electronic devices [20].

Li-Ion (lithium ion) batteries have the highest capacity to size ratio and small weight, low

self-discharge. However they require strict observance of operating and safety rules.

Every battery type has its own specific discharge profile that must be taken into consideration when calculating their operation time voltage margin for the system shutdown. For completely charged NiCd and NiMH elements, cell voltage can be in a range of 1.25-1.4 V (idle) and 1.2-1.35 V (under load). For Li-Ion loaded cells, this voltage is typically 3.6 V, but depending on battery subtype can reach 4.2 V (and even higher). In order to track the Node system voltage, we use simple resistor divider (marked as DIV on Figure 8) with one side connected to the battery and the output connected to analog-to-digital converter (ADC).

The end discharge voltage is 1V for NiCd/NiMH, and 3V for Li-Ion cell, which indicates 99% battery discharge. If a battery is discharged further, its voltage will quickly drop to 0V. This condition must be avoided, because an iterative complete discharge may not only reduce battery lifetime up to 3 times, but also cause irreversibly damage to the cell. Figure 9 shows typical discharge characteristics for NiMH/NiCd and Li-Ion cells, and temperature effect on capacitance of Li-Ion cells.

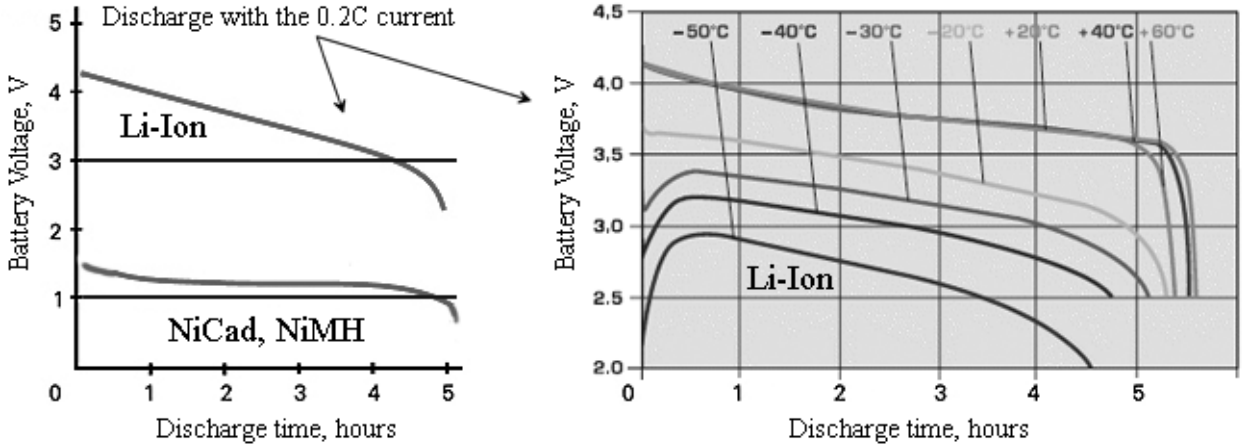

Figure 9. Typical discharge profile for NiMH/NiCd and Li-Ion cells (left) and its change due to temperature effect for Li-Ion cell (right) [21]. Discharge current is 1/5 of full capacity.

The operating temperature also affects the battery performance and lifecycle. The Node unit doesn't participate in temperature regulation (only monitoring), but the temperature range must be considered when selecting a battery type. In general, for modern batteries, lower temperatures will reduce cell capacity while higher temperatures can significantly reduce battery lifecycle (e.g. up to 20% at 30 °C for NiMH elements).

To control the operation of the power supply unit, a control signal from mechanical SPST On/Off switch is used. This signal propagates through the OR gate to the DC-DC circuit, consequently activating or shutting it down. The MCU also has a control over switching regulator using the same OR gate and a feedback signal from the On/Off switch to monitor its position. With this design, the system can sense user action and add a delay before power down if important tasks are underway, such as writing to flash or EEPROM memory.

To buffer the sensors and MCU, an LDO regulator is used after the DC-DC circuit. The output voltage from a DC-DC regulator can have ripple and spikes in excess of 20-30mV p-p depending on components used, in addition to noise caused by digital circuit loads. This is more than many sensors can tolerate. To reduce this ripple, the 3.3V power line includes post regulation through separate low-noise high power supply ripple rejection (PSRR) LDO regulator with appropriate filtration. This approach improves output stability, accuracy and transient response [22].

The LDO selected in this design is a 3.0V LDO (MAX8510, Maxim) along with 2.5V (MAX6166A, Maxim) and 1.25V (ADR127, Analog Devices) serial references (marked as REF on Figure 8). References are sourced from analog 3.0V rail. All these voltage levels are required for analog circuits and microcontroller ADC reference, described later. While it is possible to use a precision resistor divider and a buffer as replacement for ADR127, this solution

was rejected due to the higher cost.

A supervisor is important in any embedded system since a voltage drop may randomly change the next instruction memory address making program behavior unpredictable. Because of this, a circuit supervisor MAX6394 (marked as Reset in Figure 8) is included in this design. It is connected to the digital power supply rails and continuously monitors the voltage level. If the voltage drops below 3.1V, this circuit generates a reset for the MCU. In addition, this supervisor creates a delay on power up to the MCP to allow voltages to stabilize. For the Node system, the reset voltage threshold was selected at slightly higher level than the minimum voltage required for the MCU. The MCU used in this design, a Microchip PIC24FJ64GA104, can persistently operate at voltages in the range of 2.2…3.6 V. A 3.1 V threshold ensures that the MAX8510 LDO regulator that is sourced from digital rail and will get at least the 3.1 V required to produce 3.0 V for analog circuits. If the digital rail drops below this level, the analog rail also drops and signals from sensors and AFE are not valid anymore. In this condition, the MCU will keep resetting preventing data collection, processing and transmitting to the Base, until digital rail returns to normal value. Figure 10 shows power supply and reset circuit schematic for the Node device.

Power entry to the Node is provided with a standard 2.1 mm ID jack J5. Switching regulator TPS61025 absolute maximum ratings specify maximum input voltage at 7 V, and maximum operation input voltage at 5.5 V [23]. Based on this information, transient voltage suppressor (TVS) D7 was selected. It helps to reduce voltage spikes by clamping voltage higher than 5.1 V. Each node also includes reverse battery polarity protection.

Reverse polarity protection circuit is based on Q1 N-Channel MOSFET. It is possible to use low-cost Schottky diode for this purpose, but for battery powered applications this solution

reduces the voltage level available from battery and efficiency of the circuit due to the diode voltage drop and consequent power dissipation [24].

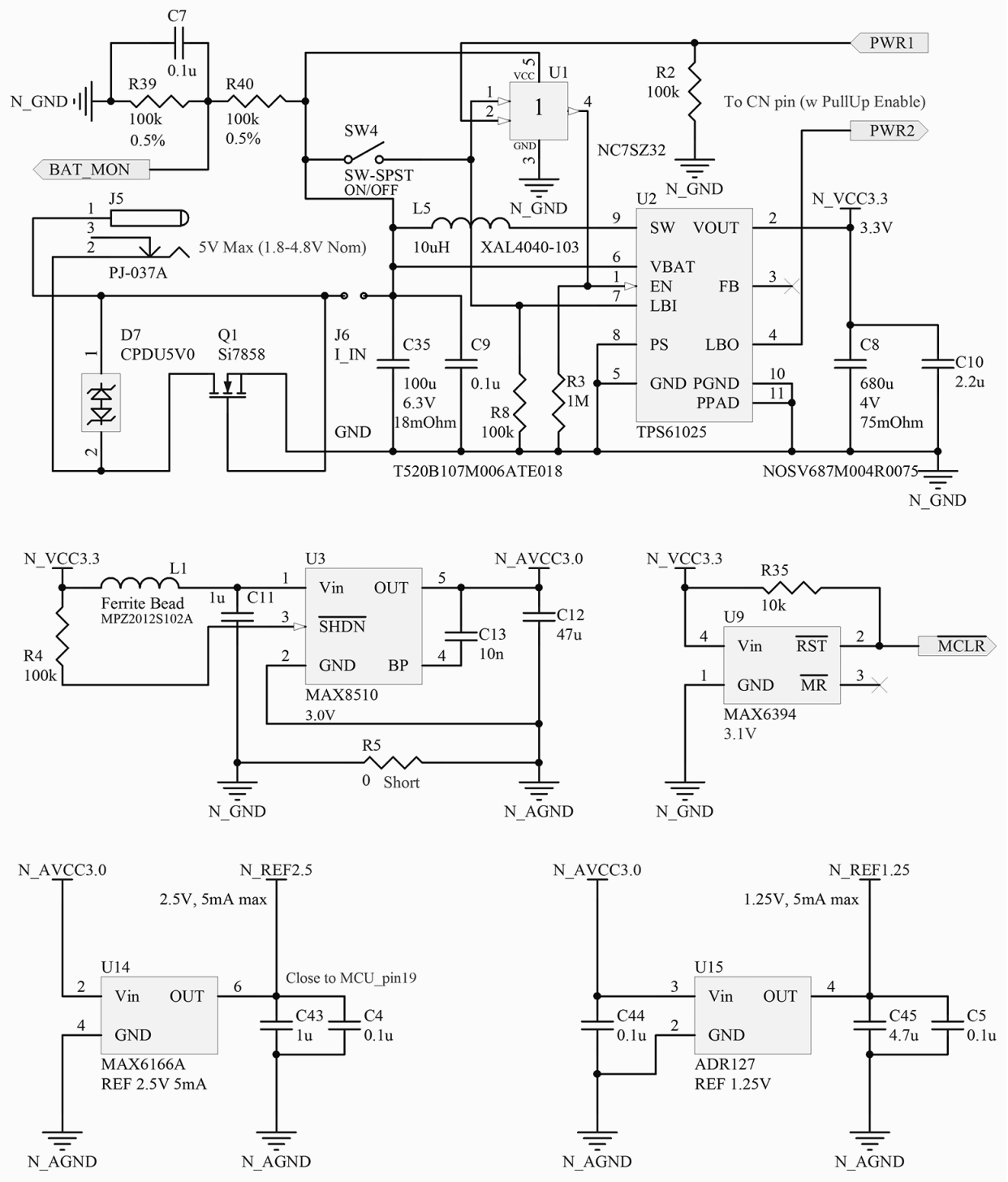

Figure 10. Power supply and reset circuit schematic diagram for the Node device.

These MOSFETs operate as follows. When a positive voltage is connected to Q1 gate, it pushes away positively charged holes in p-substrate, and attracts electrons from source, creating a conductive layer under the gate. In this case, the MOSFET is turned ON and current flows through the load. If reverse polarity is applied, and gate is negative in respect to source, then it attracts holes from p-type substrate and consequently blocks electron flow between n-type areas of drain and source. The MOSFET is turned OFF and current can't flow through the load.

For the MOSFET to turn on, a positive potential between gate and source V_{GS} has to be higher than a threshold voltage. MOSFETs with a low threshold voltage have to be used in low-voltage applications. In the ON state, the drain-source channel has some resistance called $R_{DS(on)}$ that mainly depends on V_{GS}. Obviously, power loss will depend on this parameter, and MOSFET with lower $R_{DS(on)}$ is preferable to use. In our case, Si7858 (Vishay Siliconix) MOSFETs were selected [25]. This MOSFET has $R_{DS(on)}$ = 0.003 Ω at VGS = 2.5 V, which is typical for 2 NiCd/NiMH batteries.

For comparison, if a Schottky diode was used instead, the power losses would be as follows. Assume a forward voltage V_F = 0.2 V and Si7858 N-Channel MOSFET along with an average system current I_{SUPP} = 0.1 A and input voltage V_{IN} = 2.5 V. The power dissipated on diode is equal to

$$P_{LOSS\_D} = V_F * I_{SUPP}. \quad (1)$$

Power dissipated on MOSFET can be written as

$$P_{LOSS\_M} = R_{DS(on)} * (I_{SUPP})^2. \quad (2)$$

P_{LOSS_D} = 20 mW, P_{LOSS_M} = 0.03 mW. The power loss in case of diode will be even higher due to the reduced voltage (2.3 V instead of 2.5 V) delivered to switching regulator and consequently its smaller efficiency. Dependence of TPS61025 (Texas Instruments) regulator efficiency from

the input voltage is shown on Figure 11.

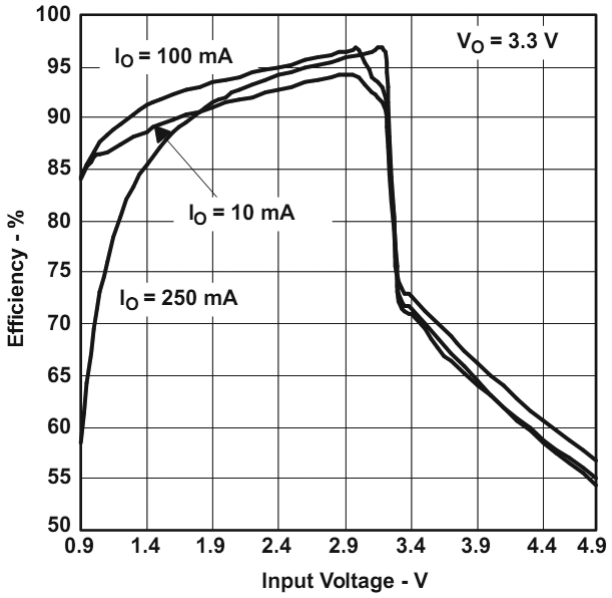

Figure 11. TPS61025 efficiency versus input voltage [23].

P-Channel MOSFETs could be used in the same manner. However it will usually have higher $R_{DS(on)}$, and must be used only when disturbing the ground return is a concern.

Connector J6 is used to measure system supplied current and is normally shorted with a jumper wire. Resistors R39 and R40 create a divider with 0.5 attenuation for battery voltage sensing (as will be explained later). The dividers accuracy can be computed as follows. The output voltage is

$$V_{DIVBAT} = \left(\frac{R39}{R39+R40}\right) * V_{BAT} - I_{LADC} * \frac{R39*R40}{R39+R40} \tag{3}$$

where V_{BAT} is battery voltage, I_{LADC} is ADC leakage current. Absolute error ΔF is determined as

$$\Delta F = \sum_{i=1}^{n} \left(\Delta x_i * \frac{\partial F}{\partial x_i}\right) \tag{4}$$

where x_i represent measured independent values with accuracy Δx_i of function F. In our case partial derivatives for V_{DIVBAT} function can be found as

$$\frac{\partial V_{DIVBAT}}{\partial(R39)} = \frac{R40*V_{BAT}}{(R40+R39)^2}\ ,\ \frac{\partial V_{DIVBAT}}{\partial(R40)} = \frac{-R39*V_{BAT}}{(R40+R39)^2}\ ,\ \frac{\partial V_{DIVBAT}}{\partial(I_{LADC})} = \frac{-R40*R39}{R40+R39} \quad (5)$$

assuming I_{LADC} equal to 0. Absolute error ΔV_{DIVBAT} is then

$$\Delta V_{DIVBAT} = \sqrt{\left(\Delta R39 * \frac{R40*V_{BAT}}{(R40+R39)^2}\right)^2 + \left(\Delta R40 * \frac{R39*V_{BAT}}{(R40+R39)^2}\right)^2 + \left(\Delta I_{LADC} * \frac{R40*R39}{R40+R39}\right)^2}. \quad (6)$$

Taking R39 and R40 equal to 100 kΩ, ΔR39 and ΔR40 equal to 500 Ω (0.5% resistor precision), ΔI_{LADC} = 500 nA (worst case analog input leakage for PIC24FJ64GA104 series MCU, taking from [26]) and V_{BAT} = 4.8 V (maximum battery voltage) we get ΔV_{DIVBAT} = 0.026 V. Because attenuation is 0.5, the resulting measurement accuracy is ± (1/0.5)*ΔV_{DIVBAT} or 0.051 V that almost fits the requirement. Accuracy can be improved by either adding buffer after divider, or reducing resistor values (e.g. by taking R39 and R40 equal to 50kΩ, accuracy is 0.03V), but this will increase power consumption/battery leakage current in small but still undesired level of degree. The above calculations ignore temperature resistance coefficient (TRC).

The boost switching regulator with step-down capability is based on a TPS61025. This IC provides a power solution for devices powered with 1-3 cells of alkaline, NiCd/NiMH, or 1 Li-Ion battery with allowable input voltage from 0.9 V to 6.5 V. The device is available in small 3x3 mm QFN package, has low 25uA quiescent current and 0.1uA shutdown current, efficiency up to 96%, a fixed 3.3V output voltage and up to 1.5 A switch current and overtemperature protection. The boost converter contains a high-efficiency synchronous rectifier with low $R_{DS(on)}$ MOSFETs, pulse width modulator (PWM) that operates on fixed 600 kHz frequency along with undervoltage lockout, softstart, and short circuit protection blocks. For light loads and in down-conversion mode the converter switches to a power save regime that uses frequency variation to improve the efficiency. The regulator is switched off (with battery disconnected from the load side) when EN pin is low. Resistor R3 pulls it down to prevent pin floating. To switch it on, the

voltage equal to at least 0.8*VBAT has to be applied to EN pin. This condition happens if OR-gate U1 (NC7SZ32, Fairchild) output is high. This happens when either the user toggles SW4 switch or when PWR1 control signal is high. Two-input OR gate NC7SZ32 can operate in wide power supply range (1.65 to 5.5 V), and its inputs tolerate voltages of up to 6 V independently of operating voltage. This feature eliminates the need in additional components on PWR1 line (that goes directly from MCU, and has 3.3 V active high level).

The TPS61025 also contains a battery-low detection circuit that is essentially a comparator with a 500mV reference connected to positive input, LBI pin connected to the negative input and an open-drain output connected to LBO. In the Node device this comparator participates in SW4 position detection and has a function of a voltage level translator. When SW4 is shorted, LBI is higher than 0.5 V, and LBO, connected to PWR2 line and pulled up to 3.3 V inside the MCU, is released, signaling to microcontroller about user switch action.

Power save mode is enabled by connecting the PS pin to ground and is activated under small output current and down-conversion conditions. Input capacitors C35 and C9 are required to improve the transient behavior and EMI of the entire power supply circuit. Their selection was based on general recommendations from datasheet and experimentally. Output capacitor (C8 and C10) selection depends on maximum allowed output voltage ripple ΔV. Ignoring the ESR, minimum capacitance can be found from the formula

$$C_{min} = I_{OUT} * \frac{V_{OUT} - V_{BAT}}{f * \Delta V * V_{OUT}} \quad (7)$$

where I_{OUT} is the maximum load current, V_{OUT} is regulator output voltage, V_{BAT} is minimum battery voltage and f is regulator operation frequency (at high loads with the minimum value taken from the datasheet). In our case assuming I_{OUT} = 500 mA, V_{OUT} = 3.3 V, V_{BAT} = 1.8 V, f = 480 kHz and ΔV = 5 mV (this high demand value is based on the fact that digital rail is used not

only for MCU supply, but also for carbon dioxide and pulse/oxygenation sensors), we get C_{min} = 100uF. Additional output ripple ΔV_{ESR} caused by non-zero capacitor ESR R_{ESR} is

$$\Delta V_{ESR} = I_{OUT} * R_{ESR}. \quad (8)$$

Inn our case (ignoring C10) using low-ESR Niobium-Oxide 75 mΩ capacitor C8 is 38 mV. To reduce this ripple component, ceramic capacitor C10 with R_{ESR} = 10 mΩ was added in parallel to C8. During power supply test at constant 500 mA load and 2.4 V input voltage, the output ripple was less than 15 mV. To improve sensor reading accuracy, the measurement sequence has to be done when there is no high current supply (e.g. when RF transmitter and NDIR sensor lamp is off). Load transients (such as those created when the RF module transmits the message or the carbon dioxide sensor infrared lamp and/or air fan switches on and off) create additional ripple. To prevent this ripple from affecting the sensor data, a delay after these events is added before sensor data acquisition.

The last important component of the switching regulator power supply is the inductor. Its selection can be estimated from the maximum average inductor current

$$I_L = I_{OUT} * \frac{V_{OUT}}{0.8 * V_{BAT}} \quad (9)$$

Assuming the same 0.5 A load peak current, this leads to I_L = 1.15 A, which is below the current limit threshold (1.5 A) of the power switch. From this, the minimum inductance can be calculated as

$$L_{min} = \frac{V_{BAT} * (V_{OUT} - V_{BAT})}{\Delta I_L * f * V_{OUT}} \quad (10)$$

where ΔI_L is the desired current ripple in the inductor, which affects its magnetic hysteresis losses, regulator output voltage ripple, EMI and regulation time. It is recommended to work with a current ripple of less than 20% of average inductor current I_L. Following this, ΔI_L = 0.2*1.15 A

= 0.23 A. Then L_{min} found to be 7.5 uH. In our design, 10uH shielded power inductor XAL4040 (Coilcraft) was utilized. It has low DC resistance and 2 A saturation current, which meets our requirement. Inductor core is fabricated from composite material, significantly reducing the part size.

The microcontroller reset circuit is based on MAX6394 active-low supervisor with 4 uA supply current, a factory-trimmed reset threshold of 3.1 V, and 1% accuracy [27]. The manual reset input is not used and left unconnected. The RST pin is an open-drain output connected to MCLR line that is tied to 3.3 V digital power rail through 10kOhm resistor to meet PIC24 MCU requirement. MCLR line is shared with the microcontroller debugger device (marked as ICSP on Figure 8) in wired OR fashion. Reset timeout period is around 100ms.

The power supply for the analog blocks was designed around ultra-low noise high PSRR linear regulator MAX8510 that is available in space-saving package SC70-5, and is able to deliver 3 V at up to 120 mA load, has internal overtemperature protection and current limit circuit. It is powered from digital 3.3V rail source through ferrite bead L1 and capacitor C11 filter that reduces input voltage ripple and increase supply-noise rejection. External bypass capacitor C13 reduces noise at the output, and C12 is required for regulator stability and improves load-transients. Shutdown control pin SHDN is pulled up to activate the circuit. The power supply system in the Node uses analog and digital ground separation technique to prevent the mixing of digital ground noise with analog current paths. For that reason R5 zero-Ohm resistor is used as a point where two grounds are connected together.

Two reference sources are available for device analog blocks: 2.5 V and 1.25 V. Both get a supply from the analog power rail. The 2.5 V source is provided by U14 MAX6166 circuit, a low-dropout precision voltage reference with a very low temperature coefficient of 5 ppm and

initial accuracy of 2 mV for a wide temperature range. It can provide a load current of up to 5mA and doesn't need an output capacitor. However, to improve circuit transient response, C43 was added. This reference determines the ADC input voltage range of the microcontroller as well as the carbon dioxide sensor pyroelectric detector supply. The second reference source determines the middle point of ADC range, which is required for some sensor conditional circuits (carbon dioxide and respiration rate AFEs) to shift bipolar signals for a unipolar range. It is based on U15 series band gap reference ADR127, a highly accurate and temperature compensated IC. The reference does require small output capacitor for stable operation, and an input capacitor was added to improve transient response.

3.3. Sensors

Gas concentration can be measured in a number of different ways, with all their advantages and disadvantages. The most accurate method is chromatographic. Unfortunately, this requires heavy and expensive equipment, is time consuming, and therefore is only recommended for "gold standard" measurements. Optical methods are the fastest and are based on light absorption. Every gas has a particular wavelength with maximum absorption, which makes it possible to design sensors with relatively high selectivity. The disadvantage of this method includes the high dependence on environment conditions like temperature, humidity and pressure. To compensate the sensor output for these parameters, special compensation is required that consequently complicates the sensor design and increases its weight, cost, and power consumption. Thermomagnetic gas concentration measurement methods are based on changes in the magnetic properties of molecules depending on temperature. This method can be characterized by no need for calibration, a low selectivity, and high power consumption due to the need of gas heating. Thermoconductometric methods use gas thermal conduction change

depending on its concentration in a gas mixture. Due to a lack of selectivity, it can only be used for two-component gas mixtures to determine their concentration ratio.

3.3.1. Oxygen sensor

To measure the oxygen concentration in the air, electrochemical sensors are primarily used. These sensors can be divided into solid-electrolyte, polarographic, and galvanic type. In a solid-electrolyte sensor, zirconium dioxide heated to 500-800 °C is used as the electrolyte, which makes it inefficient in taking measurement in room-temperature environment due to the high power consumption and fire risk. Polarographic oxygen sensors are usually referred to as Clark cells and are most widely used in scuba and medical equipment. They contain a liquid electrolyte, have a high selectivity and accuracy, a small size and weight, and a long storage life when stored in an oxygen-free environment. The problem with this type of oxygen sensor is the electrolyte is directly engaged and used in a chemical reaction - the speed of which depends on the oxygen concentration. As the electrolyte is gradually used up, at some point it needs to be replaced. A second problem is that these sensors require external precise voltage source [28]. A galvanic oxygen cell, in contrast, doesn't need an external power supply. The output voltage/current is directly proportional to oxygen partial pressure, which makes it simple to use and calibrate. They have acceptable (for the most needs) accuracy but relatively slow response time to concentration change.

The sensor type selected for the Nodes is a galvanic sensor. Galvanic sensors possess small size and have long lifecycle of up to 10 years (under certain conditions), and therefore are widely used in portable gas analyzers. However, galvanic cells have an aging problem regardless of oxygen presence, which leads to gradual decrease of sensor output signal and the need of periodical recalibration. The lifecycle is significantly reduced by higher oxygen

concentrations, so these sensors are not the best choice when working with a pure oxygen environment for a long period of time.

An oxygen galvanic cell contains two electrodes separated by an electrolyte and oxygen-soluble membrane (Figure 12). One electrode is called sensing, and it is usually made from material that supports the electrochemical reduction of oxygen – silver, gold etc. The following equation represents this process:

$$O_2 + 2H_2O + 4e = 4OH^-. \quad (11)$$

The opposite electrode is manufactured using easy-corrodible metal like lead, which reacts with hydroxyl ions and releases electrons, creating current through the external load:

$$2Pb + 4OH^- = 2PbO + H_2O + 4e. \quad (12)$$

The whole electrochemical reaction over the cell is then

$$2Pb + O_2 = PbO + current. \quad (13)$$

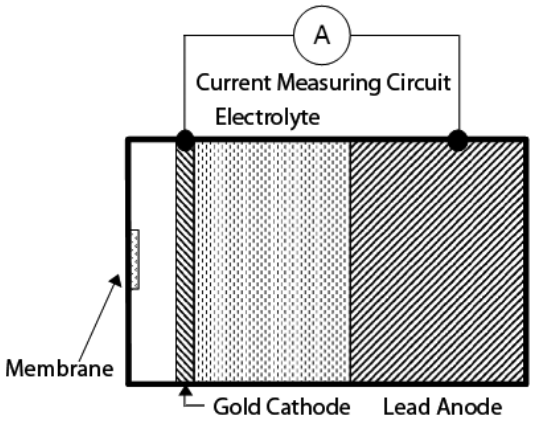

Figure 12. Oxygen electrochemical sensor structure.

The membrane between the sensing electrode and environment creates a diffusion barrier to make the cell operate in a diffusion-driven regime. It is made from some sort of polymer and is very important as it determines the sensor characteristics. For metalized solid polymer (e.g. Teflon) membranes, oxygen partial pressure at the sensing electrode side is zero, making the

barrier concentration gradient equal to the partial pressure of oxygen in the environment. This leads to a linear dependence between the current flow and oxygen partial pressure. These sensors also tend to have a high temperature coefficient (up to 3% per °C), requiring temperature compensation.

Using porous membranes as a diffusion barrier, current flow is then proportional to the volume fraction of the gas instead of partial pressure, which is a preferred characteristic for gas measurement applications. With a porous barrier, the temperature coefficient drops to 0.2%/°C. Porous barriers create significant non-linearity for the gas concentrations of more than 20%, but for lower values can be considered linear and only a small (or no) compensation is required [29].

Oxygen galvanic cell sensors are produced by many companies. Figaro Engineering KE-series sensors have a long life expectancy of up to 10 years in 21% vol. oxygen atmosphere and provide internal temperature compensation along with linear voltage output. Accuracy is up to 2% at full scale, the response time is 14s, operation range is +5…+40 °C and 80…121 kPa [30]. The company provides engineers with a very detailed documentation about these sensors. The disadvantage for using KE cells in the WHM device is its relatively large size, 50x23x24 mm.

City Technology proposes a wide range of oxygen sensors for automotive, industrial, medical and indoor use. CiTiceL® series oxygen cells are used for gas monitoring within 1…25% vol. range, have extended operation temperature range of -20…+50 °C, 2 year life expectancy and small size [31]. While they are suitable for the current project, an alternative sensor was chosen due to its lower cost.

Alphasense A, C, G-series cells are extremely suitable for safety applications due to relatively good temperature and pressure (0.2% vol. O_2 per 10 kPa) dependence. These sensors can operate between -30 and +50 °C and have a low sensitivity to humidity and CO_2. In

particular, the O2-A3 sensor that was selected in this project generates 2.5…85 uA current through the 47 Ω load over 0…20.9% vol. oxygen concentration range along with 15s response time, has a small size (20x17 mm) and 3 year lifetime [32].

Even though the requirement is to monitor 0% to 100% oxygen concentration, a narrower range of 0…42% is supported to prolong sensor life. Later this range can be extended by either using another sensor type or by sacrificing the sensor lifetime. O2-A3 documentation doesn't give any numbers for lifetime reduction, but according to [30], 100% vol. O_2 in comparison to 21% will reduce the life of KE-50 by 4 times. In addition, use at concentrations above 42% will necessitate hardware changes (i.e. adjustments in circuit gains) as well as software changes (i.e. linearization, compensation, and limit computations).

The signal conditioning circuit for the above sensor is shown on Figure 13. Precise low-ppm resistor R72 provides the load for the cell. R71 is used for operational amplifier (op amp) balancing to compensate for circuit output offsets caused by the difference in base currents of the input stage bipolar transistors. It is sufficient for R71 value to be close to R73||R74 to make the op amp "feel" the equal input resistance on both input terminals and create an optimal condition from circuit offset point of view. The DC gain of non-inverting circuit is 309, which gives the output voltage of 2.15 V at 41.8% vol. O_2. C17 reduces the gain at higher frequencies, filtering out the noise and preventing possible self-oscillation. Precision op amp U23 LT6003 (Linear) was selected based on ultra-low input bias current (90 pA max), single power supply operation, and very low power consumption [33]. Due to using output calibration, there is no need to consider variations in resistor values. However, temperature affects do need to be taken into account.

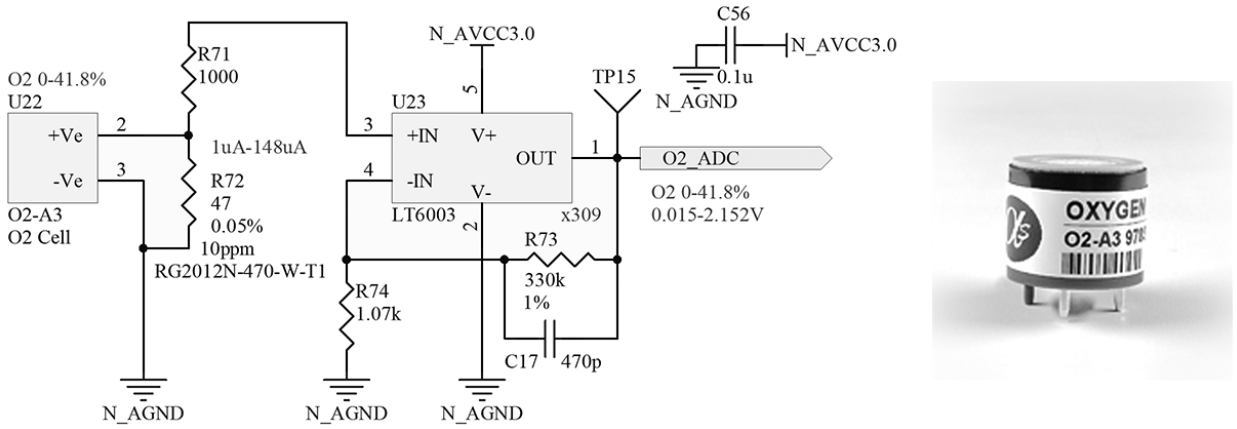

Figure 13. Oxygen concentration sensor O2-A3AFE (left) and sensor general view (right) [32].

The LT6003 has maximum input offset voltage drift about ±2 uV/°C. In the range of -10 to +50°C, this leads to its maximum deviation of 35*2 uV = 70 uV and consequently circuit output voltage deviation of 70 uV*309 = 21.7 mV. This produces an error of ±(21.7 mV/(2.15 V/41.8% vol. O_2)) = ±0.43% vol. O_2. According to [32], oxygen sensor itself without temperature compensation has up to 8% output error (1.6% vol. O_2) for the same temperature range. This gives us the total accuracy of ±2% vol. O_2 and means that software temperature compensation is necessary to keep it close to 0.5% and meet the requirement.

3.3.2. Carbon dioxide sensor

For carbon dioxide (CO_2) detection, an electrochemical method also can be used. A classic example of this sensor type is TGS4160 (Figaro Engineering), which is a small solid-state sensor with long life, high selectivity, resistance to humidity changes, and is operable under low-temperature conditions [34]. The disadvantage of this sensor is a long warm-up time (>2 hrs.) and the need of gas heating, which leads to relatively high current consumption.

The physical structure and schematic designation of this sensor is shown on Figure 14. A cation solid electrolyte fills the gap between the gold-plated lithium carbonate cathode (pin 3) and the gold-plated anode (pin 4). At the top there is a gas-permeable membrane, absorbent

material (zeolite) that reduces the influence of side gases, and the platinum heater (pins 1, 6). Also, the sensor contains a thermistor (pins 2, 5) to monitor the inner gas temperature for compensation.

The cathodic, anodic and the overall reactions are:

$$4Li^+ + 2CO_2 + O_2 + 4e = 2Li_2CO_3, 4Na^+ + O_2 + 4e = 2Na_2O \quad (14)$$

$$Li_2CO_3 + 2Na^+ = Na_2O + 2Li^+ + CO_2. \quad (15)$$

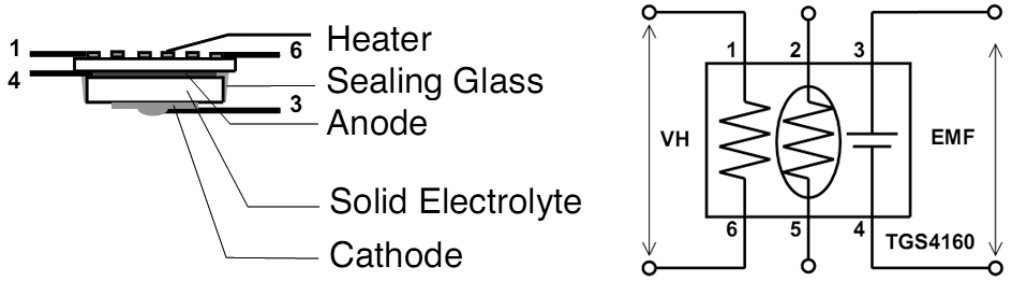

Figure 14. CO_2 concentration electrochemical sensor TGS4160 internal structure (left) and schematic view (right).

As a result of the reaction, an electromagnetic force (EMF) is generated proportionally to the partial CO_2 pressure and the temperature. In order to make accurate measurements, it is important to keep the heater voltage at a precise level and to ventilate the sensor with fresh air periodically to set zero EMF. Temperature compensation using a thermistor is not necessary if instead of measuring absolute EMF (which changes with temperature). Temperature-independent ΔEMF is monitored and used in calculations. However, this requires a more sophisticated algorithm that is implemented on signal-conditioning board AM-4, manufactured by Figaro Engineering for evaluating and testing purposes.

The TGS4160 sensor was rejected for the use in the Node device due to the power consumption (1.25 W) and sensor end-of-life. At the same time when the WHM system was completely designed and fabricated, a new solid-electrolyte CO_2 sensor CO2-D1 (Alphasense)

appeared on market. As opposed to the above, it doesn't require power supply and can operate within a wide range of CO_2 concentrations [35]. However, temperature operation range is limited to +1 to +35 °C, the sensor sensitivity changes with concentration, the response time is relatively long, and regular zeroing is required.

The non-dispersive infrared (NDIR) absorption method is a popular spectroscopic approach of gas concentration measurement that is best suited for gases with absorption lines in 3…5 and 8…12 um ranges [36] (e.g. CO_2, CO, N_2O, hydrocarbons and hydrogenated fluorocarbons). Basically, a dual-beam NDIR system consists of an infrared (IR) emitter that can be either light-emitting diode (LED) or tungsten lamp, an optical narrow-band filter to create a wavelength selective beam, a chopper to split the beam and create two identical beams, an optical absorption paths one filled with the analyte gas and the second filled with reference gas, and a thermal IR detector (refer to Figure 15). The optical filter is tuned to the wavelength on which a strong absorption occurs for the target analyte gas. The amount of light intensity detected by IR detector will then be inversely proportional to target gas concentration in sample cell.

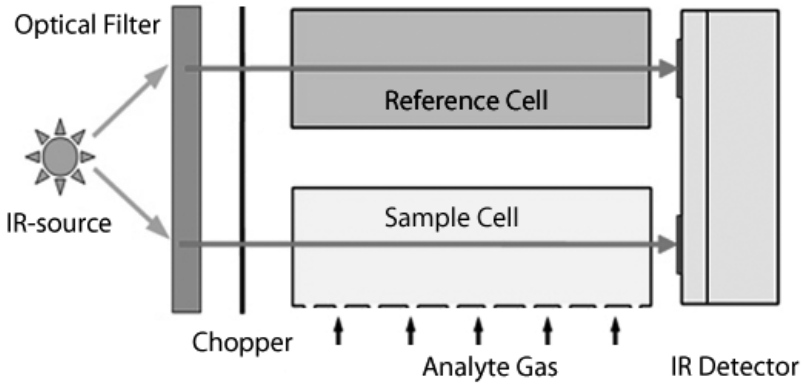

Figure 15. Principle diagram of dual-beam NDIR gas concentration measurement [37].

Usually, NDIR sensors will contain a temperature sensor for compensation due to the gas

inside the cell will have higher temperature due to the IR source heat.

IR detectors used in NDIR sensors can be of thermopile or pyroelectric type. A pyroelectric detector contains a sensing element that is made from pyroelectric material. Because this material is also a piezoelectric material, it can generate a voltage in response to thermal expansion caused by thermal energy transferred to its body [38]. The advantage of these detectors is that they have a very high sensitivity and wide heat energy dynamic and frequency ranges. However they are only sensitive to thermal energy flow change, and have a slow response. This leads to IR source control and pyroelectric AFE circuit complication along with the processing algorithm complication due to the need of low-frequency pulse generation, filtration and AC signal acquisition. The other problem is that being a piezoelectric, material is also sensitive to any mechanical stress (produced by vibration, loud sound etc.), making it hard to distinguish the sensor output caused by IR heat waves. To overcome this problem, pyroelectric sensors must contain 2 symmetric elements with electrodes connected in such way that any mechanical in-phase force will produce out-of-phase signals cancelling each other.

A thermopile thermal radiation detector is a device that produces DC voltage proportional to the incident radiation. Its construction is essentially a pair of thermocouples serially connected. The sensor has a large thermal mass base on which a “cold” junction and temperature sensor (or thermostat) is placed. This base supports a thin membrane on which a “hot” junction is located. High sensitivity and low noise can be achieved by using junction materials with high thermoelectric coefficients (e.g. bismuth, antimony) of opposite signs. Instead of double-metal junctions, semiconductors can also be utilized to build a thermopile. For example, silicon has a very large thermoelectric coefficient and relatively low volume resistivity. In this case IR detector can be embedded in an IC circuit itself.

NDIR CO_2 sensors are fabricated by such companies like Figaro, Alphasense, Dynament, City Technology, Apollo and many others. Sensor models vary in measured gas concentration range, resolution, accuracy, operation conditions and price. Typically, pre-calibration is an important feature since it eliminates the need of manual calibration. Some pre-calibrated sensors like IRCEL-CO2R (City Technology) store linearization coefficients in read-only memory (ROM) located within the device enclosure and accessible though the electrical data interface (like 1-wire or I^2C) pins [39]. More advanced sensors like MSH-P-CO2 (Dynament) have a built-in circuit that takes care about all sensor data processing and generate final gas readings available through the serial interface (UART, I^2C, SPI) or analog voltage proportional to concentration value [40]. These sensors are easy to use, but they are usually overpriced and power consumption is higher.

For the Node unit, IRC-A1 (Alphasense) NDIR CO_2 sensor was selected due to its low power consumption, high accuracy, detailed documentation, affordable cost, and availability. This is a dual-beam device that uses a pyroelectric sensor and a tungsten lamp as the IR source [41]. The manufacturer builds these sensors for four CO_2 concentration measurement ranges and related field of use: indoor air quality (0…0.5% vol.), safety (0…5% vol.), combustion (0…20% vol.) and process control (0…100% vol.) For our application, the range of 0…5% vol. is appropriate. Sensors for this range give the resolution of 0.01% vol., and accuracy of 1.5% full scale with appropriate temperature correction and calibration [42]. Sensor general view and AFE schematic (lamp control only) is shown on Figure 16.

The tungsten lamp (pins 1,2) has to be sourced from 5 V power supply with 50% duty cycle pulses at 2…2.5 Hz. The lamp can be driven by a lower voltage by sacrificing the detector output level and consequent signal-to-noise ratio (SNR) at the same time increasing lamp

lifetime and reducing the power consumption [43]. Sourcing the lamp from 3V reduces the sensor resolution to approximately 0.02% vol. and average power consumption to 0.07W. The sensor warm up time will also be reduced due to the less heat and gas temperature raise and, consequently, time required for stabilization of the internal sensor temperature. Lamp life will be prolonged in excess of 50 times as well. The disadvantage of 3V operation is that the tungsten filament will gradually cover the inner surface of lamp glass reducing the output. Solution for this problem is to use higher voltage at start up for couple minutes during the device warming up. Unfortunately, this feature has not been implemented in the current version.

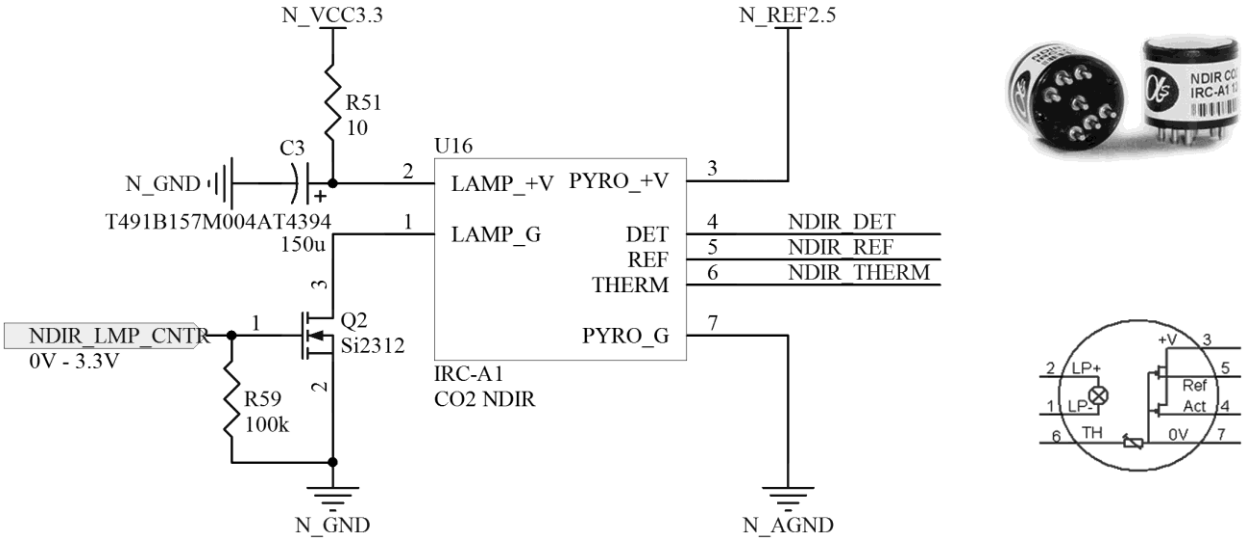

Figure 16. CO_2 concentration sensor IRC-A1 AFE (lamp control) (left) and sensor general and schematic views (right) [41].

The lamp is controlled by the NDIR_LMP_CNTR line connected to the microcontroller and the MOSFET switch Q2 Si2312 (Vishay) with a low $R_{DS(on)}$. Filter C3, R51 is used to reduce ripple on power supply rail caused by high start current through low-resistive cold filament. In future revisions of the Node, it is recommended that R51 be removed and replaced with PWM techniques for current limiting to improve power consumption of the system. R59 is needed to

prevent MOSFET gate from floating when MCU pin is in high-impedance state.

3.3.3. Air temperature

An NDIR sensor contains built-in thermistor (pins 6, 7) to monitor inner gas temperature that is higher by a few degrees C due to the IR source heat. Thermistor AFE is shown on Figure 17. Ideally, a current source would be used and is recommended for the next revision of the Nodes. Thermistor resistance changes over the range of -10…+50°C from 14 to 1.2 kΩ. Assuming safe current of 200 uA, R63 = 11.3 kΩ. R65 = R68||R67 = 21 kΩ balances the op amp, and along with C55 also works as 7.5 Hz low-pass (LP) filter to reduce the noise. Op amp U20 OPA333 (Texas Instruments) is low voltage offset and drift, single-supply device [44]. Its gain was set to fit 2.5 V ADC range.

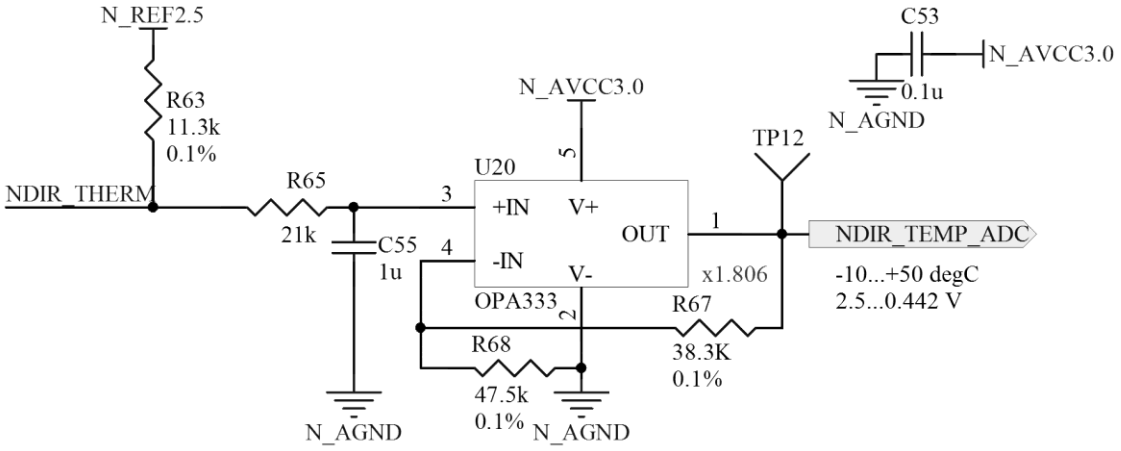

Figure 17. CO_2 concentration sensor IRC-A1 AFE (thermistor conditioning).

In the simulation of this circuit, a thermistor model using Steinhart-Hart equation [45] and table data from [46] was used. According to it, thermistor temperature-resistance dependence can be described as follows:

$$R_{TH}(T) = e^{(\beta-\alpha/2)^{\frac{1}{3}}-(\beta+\alpha/2)^{\frac{1}{3}}}, \alpha = \frac{A-\frac{1}{T}}{C}, \beta = \sqrt{\left(\frac{B}{3*C}\right)^3 + \frac{\alpha^2}{4}} \quad (16)$$

where T is temperature in Kelvin. Coefficients A = 1.04m, B = 289u and C = 1.3n were

calculated to produce an accurate IRC-A1 thermistor resistance-temperature model. Micro-Cap software package optimization feature was used to derive these coefficients. Figure 18 shows simulating schematic and dependence of circuit output NDIR_TEMP_ADC from temperature.

From (16), the temperature measurement accuracy can be computed. Assuming (16) has no error and ignoring thermistor and resistor noise along with op amp temperature parameter deviation (OPA333 offset temperature drift is close to zero), the thermistor temperature T_{TH} can be expressed in Kelvins (using the above coefficients) as

$$T_{TH} = \frac{1}{A+B*\ln(R_{TH})+C*(\ln(R_{TH}))^3} \tag{17}$$

where R_{TH} is thermistor resistance equal to

$$R_{TH} = -\frac{R63*V_{DIV}}{V_{DIV}-V_{REF25}+I_B*R63}. \tag{18}$$

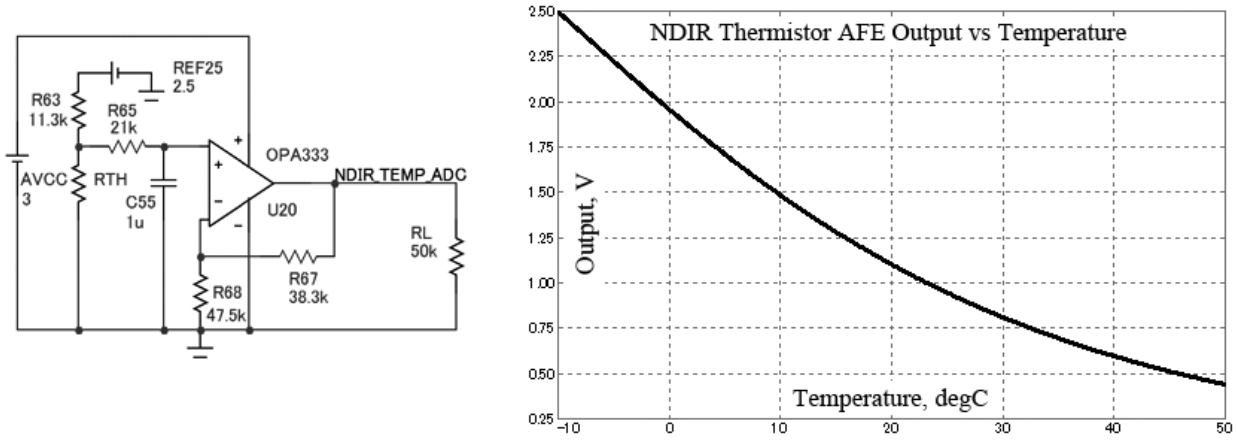

Figure 18. IRC-A1 sensor thermistor AFE simulation schematic (left) and circuit voltage output versus temperature dependence (right).

In (18), V_{REF25} is a thermistor voltage source, IB is op amp input bias current, V_{DIV} is a potential at point R_{TH}, R63 (refer to Figure 18). The last step will be to write an expression of V_{DIV} in terms of circuit output NDIR_TEMP_ADC:

$$V_{DIV} = \frac{V_{NDIR\_TEMP\_ADC}}{1+\frac{R67}{R68}} - V_{OS} + I_B * R65. \quad (19)$$

Here, $V_{NDIR\_TEMP\_ADC}$ is U20 output and V_{OS} is op amp offset voltage. We can now estimate the absolute accuracy ΔT_{TH}:

$$\Delta T_{TH} = \sqrt{\left(\Delta R63 * \frac{\partial T_{TH}}{\partial R63}\right)^2 + \left(\Delta R67 * \frac{\partial T_{TH}}{\partial R67}\right)^2 + \left(\Delta R68 * \frac{\partial T_{TH}}{\partial R68}\right)^2 + \left(\Delta R65 * \frac{\partial T_{TH}}{\partial R65}\right)^2 + \left(\Delta V_{OS} * \frac{\partial T_{TH}}{\partial V_{OS}}\right)^2 + \left(\Delta I_B * \frac{\partial T_{TH}}{\partial I_B}\right)^2}. \quad (20)$$

Taking 0.1% resistors (except R65, which is 0.5%), and assuming OPA333 ΔV_{OS} = 10 uV, ΔI_B = 70 pA, ΔT_{TH} = 0.038 °C. This error will be used in CO_2 concentration accuracy calculations.

The operating frequency of the infrared source is 2.25 Hz at 50% duty cycle. Two pyroelectric detectors monitor the IR signal luminosity passed through the reference and sample cells. Detectors are internally connected to FET followers (sensor pins 3, 4, 5, 7), which are appropriately connected to power supply and load as presented in Figure 19. Load resistors R52 and R60 limit the current through FETs to approximately 20 uA with a low-noise stable 2.5 V reference being their source. The output signals NDIR_DET and NDIR_REF consist of a DC offset voltage of 1 V, and an AC voltage of 10-30 mV p-p that is in phase with IR source pulses. To calculate CO_2 concentration, the AC component is needed.

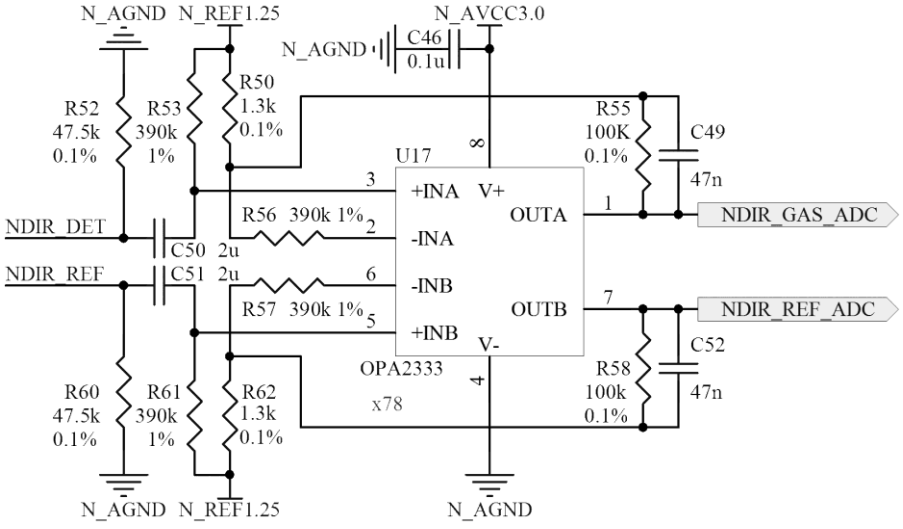

Figure 19. CO_2 concentration sensor IRC-A1 AFE (pyroelectric detector conditioning).

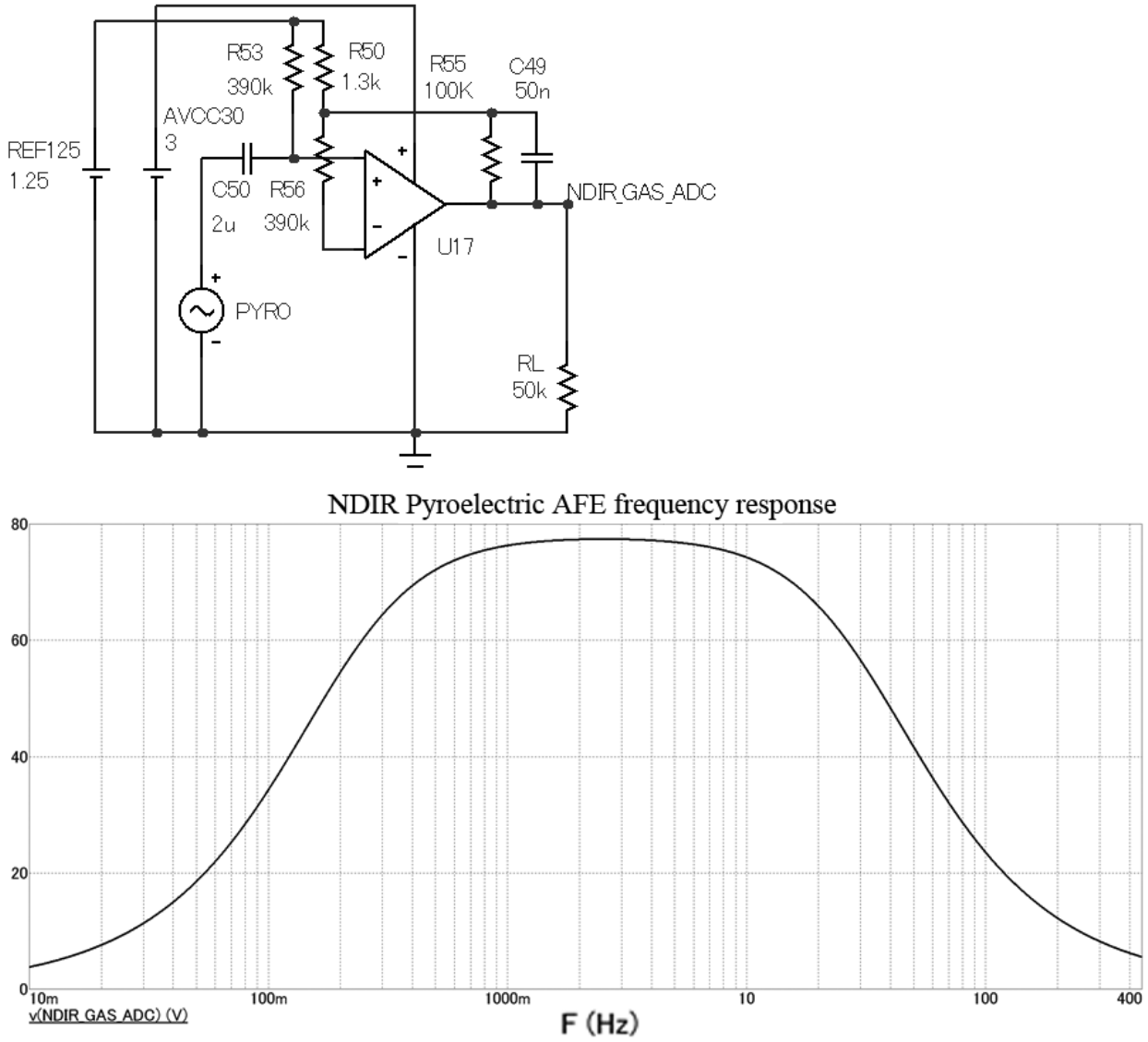

Figure 20. IRC-A1 sensor pyroelectric detector AFE simulation schematic (top) and its frequency response (bottom).

Figure 21 depicts signal output versus signal input in the time domain. Since both channels are identical, only one channel is shown on the simulation. Filter design details are omitted since they were done using Filter Solutions (Nuhertz) software package without manual calculations. Also, there is no need to make accuracy calculations for the pyroelectric AFE because coefficients for gas concentration will be derived though the calibration. However, both

channels must have matched characteristics, and for that reason 0.1% precision resistors were used.

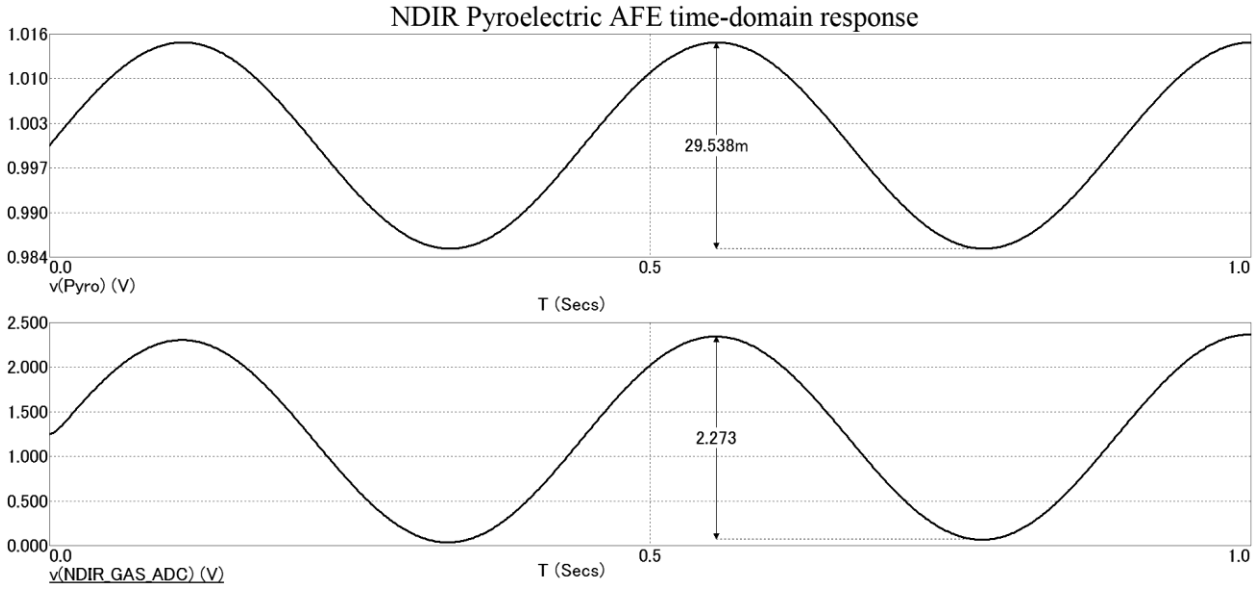

Figure 21. IRC-A1 sensor pyroelectric detector AFE time-domain response.

3.3.4. Pressure sensor

Absolute pressure (defined as a pressure difference between the measurement point and vacuum) gas sensor for the WHM application was selected based on the required pressure range, accuracy, power supply requirements and size. This parameter can be monitored by measuring the displacement of the sensing element due to air pressure. Sensing elements of various types (diaphragms, bellows and tubes) are currently used in pressure sensors. Deformation transducing can be accomplished using linear-variable differential-transformers (coil inductance changes when a magnetic core inside the coil linearly shifts), piezoelectric effect (charge appears on crystal edges when it deforms), vibrating wire (resonant frequency change of wire that vibrates in magnetic field due to the AC current flowing through it), piezoresistive (electric resistance change of mechanically stressed material) and capacitive method (capacitance change due to the

variation in gap between solid plate and sensor membrane). The last method gives the highest accuracy (0.1% and better) and wide pressure range (up to 10^7 Pa), but needs a sensitive electronics to detect a small capacitance variations. Current methods allow registering a membrane shift of a fraction of nanometer [47].

The most common pressure sensor type is piezoresistive (also called strain-gage) sensors. Piezoresistive material is usually placed on flexible membrane. The sensitivity of such device is expressed by the gage factor GF:

$$GF = \frac{\Delta R}{R} * \frac{L}{\Delta L} \tag{21}$$

where ΔR/R represents the fractional change in material resistance, and ΔL/L is an extension per unit length. Longitudinal gage factor (the resistance change is monitored through current flow parallel to the strain) for many metals is ~2 and for single-crystalline silicon is up to 150: that is why silicon is a material of choice for many strain gages with currently 80% of pressure sensors being of this type. The advantages include silicon's high strength, elasticity and hysteresis absence, precision dimension control and fabrication, and ability to integrate signal conditioning circuit on sensor chip which leads to a lower cost.

A typical absolute pressure piezoresistive sensor is presented in Figure 22. A sensor chip is micromachined out of a single-crystalline silicon wafer. Diaphragm thickness is controlled using timed etch. A strain gauge is formed on an n-type diaphragm at stress-sensitive locations by diffusion of a p-type dopant such as boron. In the same way, the signal conditioning circuit can be produced. The vacuum cavity for sensor reference pressure is also fabricated using etching. To prevent mechanical drifts and undesirable temperature behavior, a material with characteristics close to silicon must be utilized for bottom isolation plate. The common practice is to use second silicon or glass wafer. After pumping out the air, fusion composite is used to

hermetically seal both plates together forming a firm sensor die that can be put into plastic, ceramic or metal package of lead or leadless type.

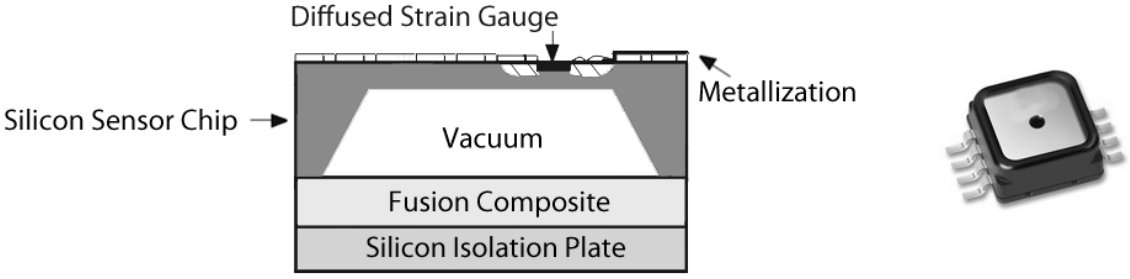

Figure 22. Absolute pressure piezoresistive sensor structure (left) and MP3H6115A6U sensor general view (right) [48].

The main disadvantage of the above pressure sensors is a low sensitivity (1…2% resistance change over the full scale) and consequently low unamplified output voltage (10…20 mV/V). In addition, silicon strain gauges have non-linear pressure response and are very sensitive to temperature changes, and therefore necessary compensation (either on-chip or off-chip) is required to achieve accuracy better than 0.1% full scale and long term stability. One example of an internally-compensated and calibrated sensor which is suitable for the WHM application is MP3H6115 (Freescale Semiconductor), pipe-less version of which is also shown on Figure 22. It can operate over the 15…115 kPa pressure range generating proportional output voltage signal of 0.1…2.8 V and accuracy of ±1.5 kPa (0…85 °C), with 3 V power supply and 4mA current consumption [48]. This sensor is ratiometric, and therefore a stable power supply has to be provided. In addition, the sensor internal amplifier circuit can source at most 500 uA without the limiting of output signal, which must be taken into consideration. A schematic diagram of the pressure sensor AFE is shown on Figure 23. Capacitors C6, C57 are used to reduce power supply noise. TP16 is a test point for troubleshooting procedures. Voltage divider R75, R76 attenuates signal by 0.82 so at maximum pressure of 115 kPa circuit output is 2.31 V.

C58 along with R75 also create a low-pass filter to suppress sensor noise. To estimate absolute accuracy, we can use equations (3) and (4):

$$\Delta V_{DIVGPR} = \sqrt{\left(\Delta R76 * \frac{R75*V_{GPR}}{(R75+R76)^2}\right)^2 + \left(\Delta R75 * \frac{R76*V_{GPR}}{(R75+R76)^2}\right)^2 + \left(\Delta I_{LADC} * \frac{R75*R76}{R75+R76}\right)^2} \quad (22)$$

where ΔV_{DIVGPR} is circuit absolute voltage error, and V_{GPR} is maximum pressure sensor output. With 1% precision resistors, $\Delta V_{DIVGPR} = \pm 0.006$ V. If circuit sensitivity is 27 mV/kPa*0.82=22.14 mV/kPa, then the total accuracy ΔGPR = 1.5 kPa + 0.27 kPa = ±1.8 kPa. Maximum divider (in addition to ADC leakage) current is less than 340 uA, which doesn't violate sensor requirements.

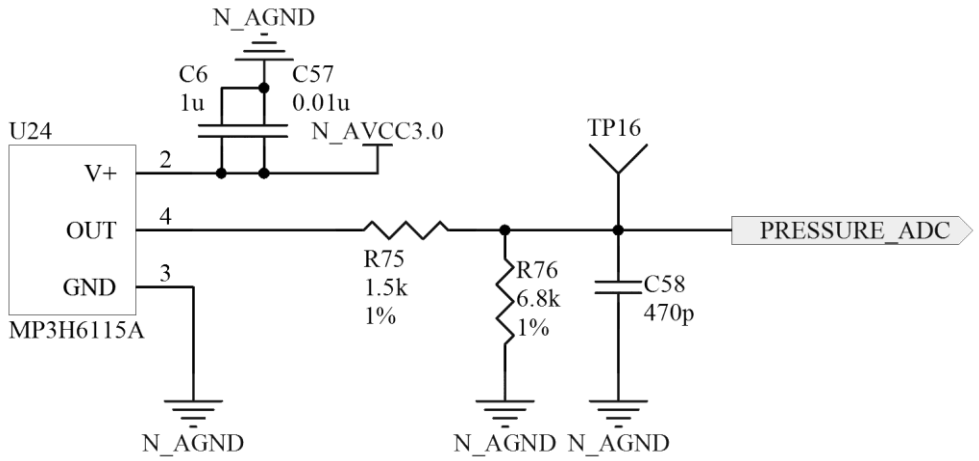

Figure 23. MP3H6116 absolute pressure sensor AFE schematic.

3.3.5. Gas temperature sensor

For absolute temperature measurement of gaseous medium, contact sensors are usually utilized. These sensors can be organized in four groups: resistive temperature detectors (RTD), p-n junction detectors, thermistors, and thermocouples [49]. RTD sensors are based on the change of a metal's resistance with temperature, have an accuracy of ±25 m°C typically, and can be fabricated in form of wire or thin film. Platinum is used most widely in RTDs, due to its long-

term stability and predictable response.

Thermistors are metal-oxide temperature sensors and can have a positive or negative temperature coefficient. These sensors are highly nonlinear and suffer from large component variations, requiring each sensor to be calibrated separately. Several mathematical models exist for thermistors, including simple single-point calibration model, Fraden model, Steinhart-Hart model, etc. The selection of this model depends upon the accuracy required and computational load. Self-heating is also a problem for these devices, resulting in a current limit of less than 200uA.

In thermocouples, two metal conductors of different type (e.g. copper/iron/nickel-chromium with constantan) create a voltage due to the thermoelectric effect. At least two junctions, one put in a reference medium with known/controlled temperature and the other one attached to medium where measurement must be carry out, are required to produce a voltage output proportional to junction temperature difference.

Semiconductor p-n junction sensors are based on strong temperature dependence of forward-biased device voltage drop under constant current. This dependence is relatively linear, which allows the use of simple two-point calibration technique. For a silicon diode, for example, the temperature-voltage relation and its slope b can be determined as

$$V = \frac{E_g}{q} - \frac{2*k*T}{q}(lnK - lnI),\ b = \frac{dV}{dt} - \frac{2*k}{q}(lnK - lnI) \tag{23}$$

where E_g is silicon energy band gap at absolute zero temperature, q is an electron charge, K is a constant, T is the temperature in degrees Kelvin, and I is a junction current. Figure 24 depicts a simple diode temperature sensor and its voltage-temperature characteristic for I = 10uA. Bipolar transistor can be used for the same purpose with equal success. It is possible to build this simple but accurate sensor as a part of IC device, adding necessary signal conditioning and digital

circuits within the same chip. Examples include AD590 (Analog Devices, current output), LM35 (National Semiconductors, voltage output), ADT7410 (Analog Devices, digital output).

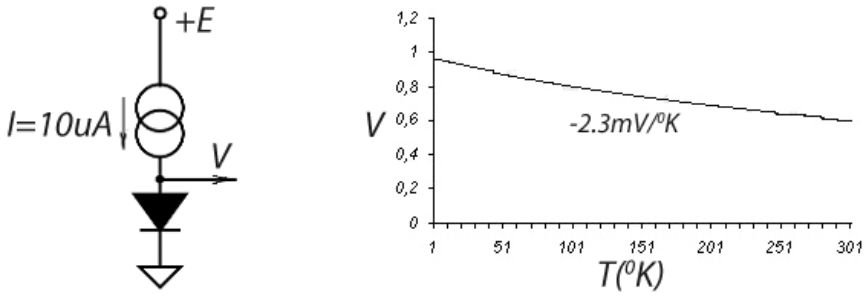

Figure 24. Diode-based temperature sensor schematic (left) and its voltage-temperature dependence (right) [50].

3.3.6. Relative humidity sensor

Relative humidity RH represents the percentage ratio of current water vapor pressure of the air Pw to the maximum possible vapor pressure P_s at the same temperature:

$$RH = \frac{P_w}{P_s} * 100. \quad (24)$$

It can also be expressed as ratio of the mole fraction of water vapor in air to the water vapor in air at saturation. Together P_w+ P_s are equal to atmospheric pressure (if the enclosure is open). At normal pressure (101.3kPa) and a temperature of 100 °C maximum possible RH is 100%, at 200°C it can only reach 6%, and above 374 °C it can't be determined. The dew point DP is determined as a temperature at which relative humidity is 100% or, in other words, the temperature that the air must reach to be able to keep the maximum amount of moisture. It can be approximated through the saturation water vapor pressure EW and temperature T:

$$EW = 10^{0.66077+\frac{7.5*T}{237.15+T}}, EW_{RH} = \frac{EW*RH}{100}, DP = \frac{237.3(0.66077-\log_{10} EW_{RH})}{\log_{10} EW_{RH}-8.16077} * T. \quad (25)$$

A device that measures humidity or moisture is called hygrometer. There are several methods that can be used for relative humidity transducing. One of the most popular approaches

is to use a capacitor with air gap as insulator. Moisture affects air dielectric permittivity ε_r that can be expressed as

$$\varepsilon_r = 1 + \frac{211}{T}\left(P + 48 * \frac{P_s}{T} * RH\right) * 10^{-6} \quad (26)$$

where T is absolute temperature in degrees Kelvin, P is moist air and P_s is saturated water vapor pressures, both in mm Hg. This equation shows that capacitance will be proportional to the relative humidity. An appropriate isolator (like some hygroscopic polymers) whose dielectric constant is significantly affected by humidity can be used instead of air gap, and capacitor electrodes can also be formed using thin-film technology on silicon substrate as presented in Figure 25 along with capacitance-to-voltage converting circuit.

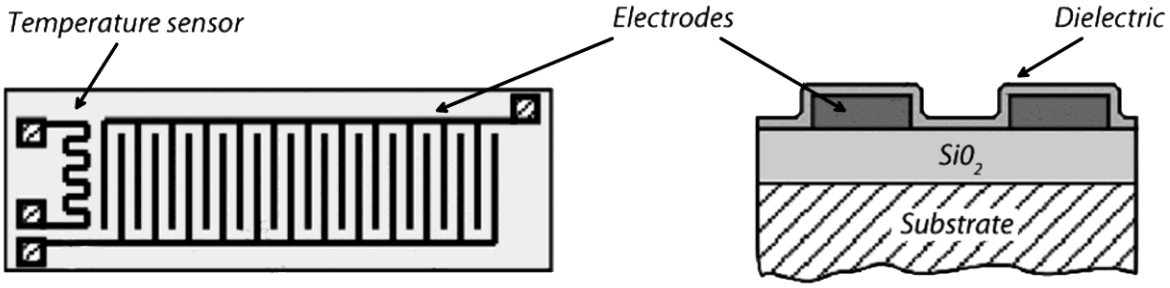

Figure 25. Capacitive thin-film humidity sensor structure [51].

In addition to capacitive sensing, electrical conductivity sensors can be used to measure humidity. In these sensors, non-metal conductors (e.g. hygroscopic film with a LiCl solution, a polystyrene film with sulfuric acid, or solid polyelectrolytes) with relatively low resistivity that changes significantly when moisture is present are used. Thin-film technology can also be applied for this kind of transducer. Even though they are not widely used in commercial devices due to the low long-term stability and life time, some thin-film conductivity sensors based on interpenetrating polymer networks also show promise as RH sensors with a demonstrated resistance change from 10 MΩ to 100 Ω at humidity variation 0…90%.

Other humidity measurement techniques also exist. Changes in thermal conductivity dry and moisturized air can be used. A Peltier heat pump that cools down a chilled-mirror causing a condensation of water vapor and appearing of droplets on it can also be used. Here, an optical channel is used to measure the luminosity of the beam, reflected from the mirror. The dew point is then detected by controlling the cooler and sensing the moment of condensation and consequent abrupt photodetector signal output reduction. If the temperature and ambient pressure are known, humidity and vapor pressure can be computed. Changes in a quartz crystal's resonance due to the additional weight of water droplets related to humidity can also be used, with such devices termed oscillating hygrometers.

In most of cases, temperature and humidity sensors are combined in single device such as CHIPCAP (GE). This sensor utilizes a capacitive polymer sensing technology and has an accuracy of ±3% for RH and ±1 °C for temperature [52]. The device is fully calibrated, manufactured in standard 14-pin SO package and consumes less than 0.5 mA. Three versions are available that differ in output signal configuration: linear (0…1 V), ratiometric (10…90% of power supply) and digital (using ZACwireTM interface). The linear version (CHIPCAP-L) is used in the WHM system, and its AFE schematic is shown on Figure 26.

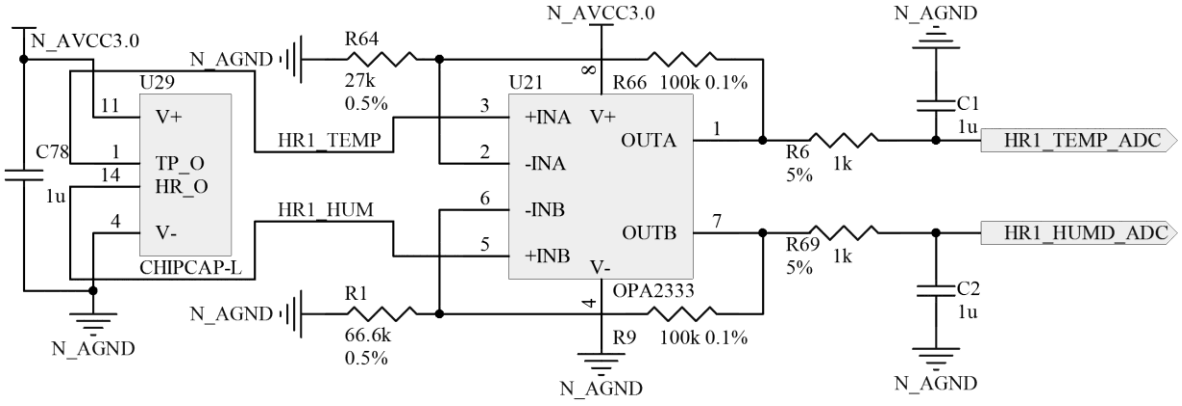

Figure 26. Temperature and humidity sensor CHIPCAP-L AFE schematic.

Resistors R66, R64 set U21 op amp gain of 4.7 for the temperature channel (making the circuit output 2.35 V at 50 °C) while R1 and R9 set the gain of 2.5 for humidity channel (producing 2.5 V at the output at 100% RH). Filters R6, C1 and R69, C2 reduce the noise on signal lines. This circuit's absolute error can be calculated as follows:

$$\Delta V_{GTP} = \sqrt{\left(\Delta R66 * \frac{V_{GTP\_SENS}}{R64}\right)^2 + \left(\Delta R64 * \frac{R66 * V_{GTP\_SENS}}{(R64)^2}\right)^2 + (\Delta I_{LADC} * (-R6))^2} \quad (27)$$

$$\Delta V_{GHM} = \sqrt{\left(\Delta R9 * \frac{V_{GHM\_SENS}}{R1}\right)^2 + \left(\Delta R1 * \frac{R9 * V_{GHM\_SENS}}{(R1)^2}\right)^2 + (\Delta I_{LADC} * (-R69))^2}. \quad (28)$$

In the above equations, ΔV_{GTP} and ΔV_{GHM} are absolute circuit voltage errors for temperature and humidity channels respectively, V_{GTP_SENS} and V_{GHM_SENS} are maximum sensor output voltages (1V in both cases). Using resistor tolerances specified on Figure 26, $\Delta V_{GTP} = \pm 19$ mV and $\Delta V_{GHM} = \pm 7.7$ mV. Circuit temperature resolution is (1 V*4.7)/200°C = 24 mV/°C, and humidity resolution is (1 V*2.5)/100% = 25 mV/%. Therefore, final temperature measurement absolute accuracy $\Delta GTP = \pm (1°C + \Delta V_{GTP}/24 \text{ mV/°C}) = \pm 1.8$ °C, and relative humidity measurement absolute accuracy $\Delta GHM = \pm (3\% + \Delta V_{GHM}/25\text{mV/\%}) = \pm 3.3\%$. Using 0.1% resistors for R1 and R64, ΔGTP can be improved to ±1.2 °C, ΔGHM to ±3.1%.

3.3.7. Human body temperature sensor

To measure the human's body temperature, an external digital sensor was utilized. Figure 27 presents the schematic of both the Node side (left) and remote sensor side (right). U30 ADT7410 (Analog Devices) is an accurate high-resolution thermometer in 8-pin SOIC package that operates over 2.7…5.5 V supply voltages, consumes less than 50 uA (in 1 SPS mode) and uses I^2C bus for communication with the host controller [53]. This device contains a user selectable 13- or 16-bit temperature-to-digital converter, provides ±0.5 °C accuracy over the range of -55 to +150 °C, and an accuracy of ±0.2 °C over the range of +25 to 55 °C. The bus

address can be selected with A0 and A1 inputs. In the current design, these inputs are grounded setting the address at 0x48. Interface pins SCL and SDA are clock input and data input-output respectively. Critical overtemperature indicator CT and interrupt INT output pins are not used and left floating. C79 and L11 create a power supply filter for the chip, and connector P11 is used to attach 4-wire flexible cable. Opposite side of this cable is connected to mini USB type B plug that was found to be very convenient for the application due to its compact size, high reliability and availability.

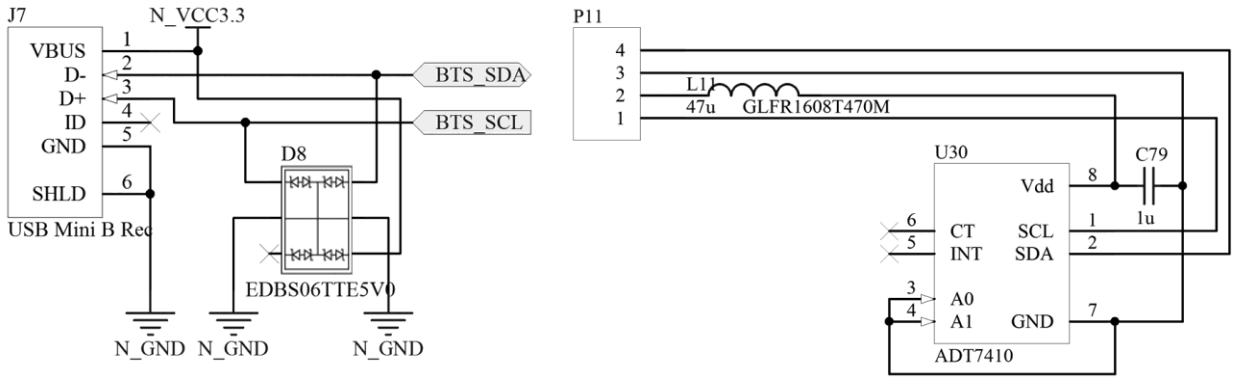

Figure 27. Digital temperature sensor ADT7410 front end schematic.

Connector J7 is a mini USB type B receptacle to which the remote temperature sensor block is connected. Diode ESD and transient voltage suppressor array D8 EDBS06TTE5V0 (KOA) protects the input circuits of the Node from possible damage. Pull-up resistors that are required for I^2C interface operation are included and are shown on microcontroller schematic page (see below). All other details regarding the software configuration and operation of the chip will be discussed in Chapter 5.

3.3.8. Blood hemoglobin oxygenation sensor

Blood hemoglobin oxygenation can be measured using invasive (taking blood sample for further analysis) and non-invasive methods. It is clear that for continuous monitoring of this

parameter in the WHM device, only non-invasive methods are appropriate. Polarographic O_2 partial pressure measurement and oxygen saturation optical measurement are two methods to measure this parameter. A polarographic oxygen sensor's operation concepts have already been discussed. It is known as Clark cell and is used to measure oxygen partial pressure in liquid or gas. Such a sensor requires an external bias voltage of about 0.6 V and generates a small current proportional to partial pressure. For transcutaneous operation, the effect of blood oxygen diffusion through skin is used as presented in Figure 28 (left). Because diffusion is normally very low, a small heater and temperature sensor are embedded into the device enclosure to warm up local skin area to temperature about 45°C, which leads to increasing of capillaries local blood flow. This method is extensively used in newborn babies monitoring, however skin of adults is too thick that leads to slow oxygen diffusion and significant errors in measurements.

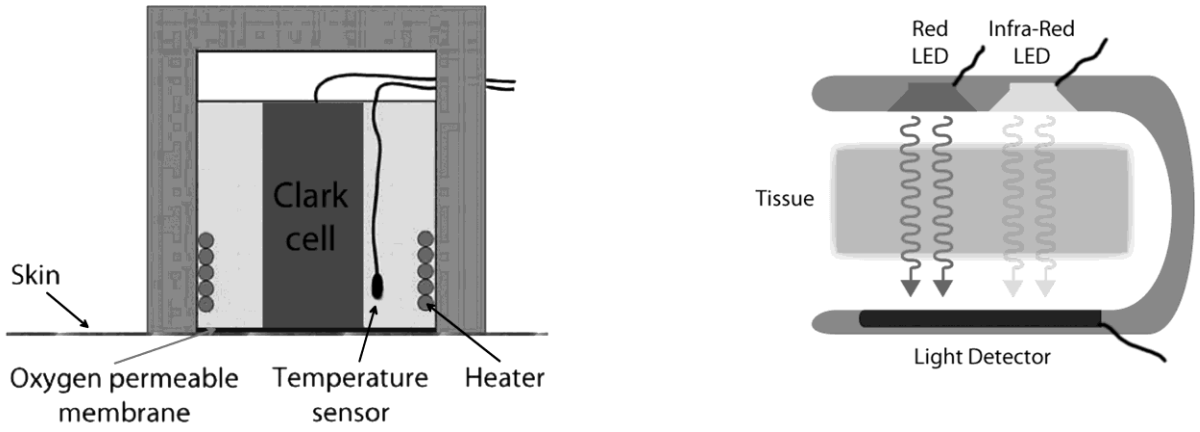

Figure 28. Transcutaneous oxygen sensor (left) and transmission optical oximeter (right) [54].

Another method for measuring the relative amount of oxygen carried by hemoglobin is called oximetry. It is based on the light absorption properties of oxygenated (HbO_2) and deoxygenated (Hb) hemoglobin [54]. Optical oximeter contains two LEDs and a sensitive light detector (refer to Figure 28, right). The first LED emits red wavelength (around 660nm), on

which HbO2 has smaller absorbance than Hb. The second LED generates infrared light (940-960 nm), on which absorbance properties are reversed (or equal). A cuvette with blood sample or, in case of non-invasive measurement, live tissue (fingertip or earlobe) is inserted between LEDs and photo sensor. Light transmission coefficient T and optical density (absorbance) OD can be expressed through transmitted (P_t) and incident (P_0) light power using Beer-Lambert's law:

$$T = \frac{P_t}{P_0} = 10^{-a*b*c}, OD = \log_{10}\frac{1}{T} \quad (29)$$

where a is molar absorptivity of the sample, b is light path through the sample and c is sample concentration. Hemoglobin oxygenation SpO_2 is then can be derived from

$$SpO_2 = A - B * \frac{OD(\lambda_1)}{OD(\lambda_2)} \quad (30)$$

where λ_1 and λ_2 represent the LED's wavelengths, A and B are coefficients that depend on Hb and HbO_2 absorptivity. Control circuit switches LEDs alternately, measuring the signal output from the detector and separating it into pulsatile and nonpulsatile components. Signal normalization leads to the deriving of red/infrared ratio that is independent from skin pigmentation and thickness, arterial pulse and can be used in Eq. (30) to calculate SpO_2.

3.3.9. Blood pulsation sensor

Optical oximeter is usually combined with a pulse rate meter because the pulsatile AC component from photo sensor also monitors blood pulsation. Figure 29 (left) shows the light absorption in live tissue along with Nonin® OEM III module and earclip sensor (right) that is capable of performing these measurements [55] and was selected to be used in the WHM project.

The module itself has a small size (35x25x5 mm), requires a 3.3 V power supply, consumes only 30mW, is shielded, and can be embedded in any system. Measurement range is

0…100% for oxygen saturation and 18…321 beats per minute (bpm) for pulse rate. Accuracy depends on sensor mount and the human's mobility. For earclip sensor model 8000Q and assuming that person is in motion, absolute error for SpO_2 is ±4% (RMS error is 1.7) and for pulse rate is ±5 bpm (40…240bpm range) [56]. This module communicates with the host controller using UART. Data format and measurement statistics level of details can be configured by the user. Figure 30 shows module connection schematic for the Node device.

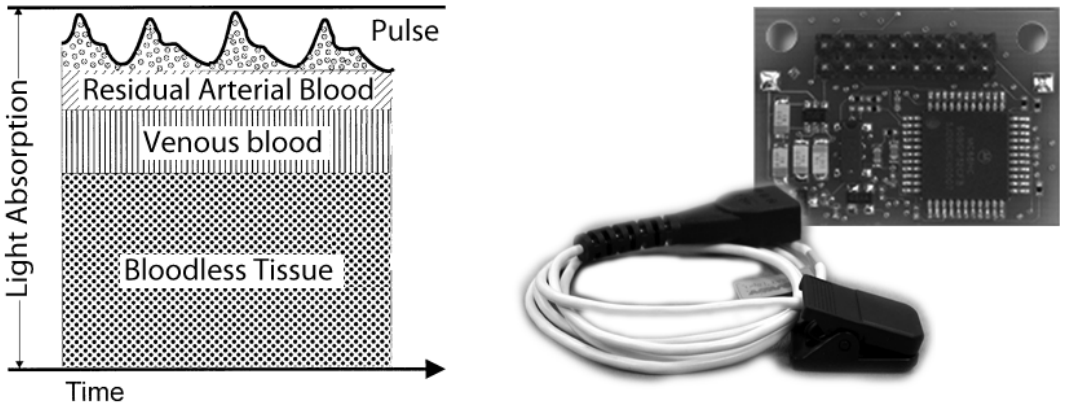

Figure 29. Light absorption by live tissue (left) [57] and Nonin® OEM III module with earclip (right) [55].

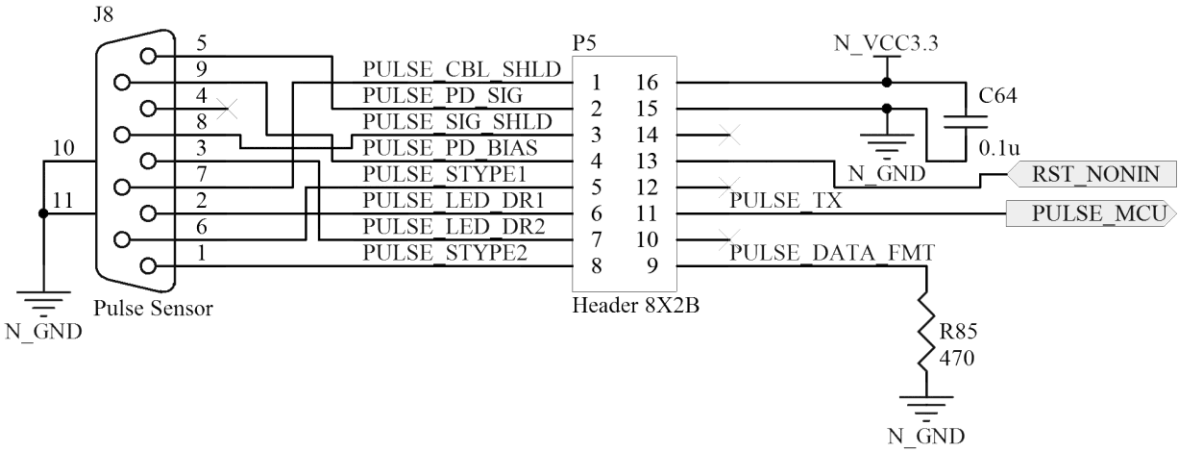

Figure 30. Nonin® OEMIII module and sensor interface schematic.

Connector J8 is used to attach the external earclip sensor (other sensors with alternative

mounting also available from the manufacturer) and route signals to the module that is plugged into P5 header, located on the Node main board. Resistor R85 selects the module data format #1 (simple format with minimum statistics, takes 3 bytes that are transmitted once per second). Signal RST_NONIN is used to reset the module, and PULSE_MCU is UART transmission line.

3.3.10. Respiration rate

One of this project's requirements is to measure the human's respiration rate. Unfortunately, there is no compact and low power sensor solution available at this time. Furthermore, most of the available methods assume that person is resting. However, for spacesuit experiments it is important to monitor the operator's respiration rate both at rest and in motion. Likewise, a novel approach had to be developed in this work.

When a human breathes, he/she pushes a breathing gas mixture in and out of their lungs. This causes pressure fluctuation inside the suit which can be sensed by an absolute pressure sensor. The change is small however in comparison to static pressure. This offset can be removed by using a differential pressure sensor, connecting one terminal to isolated cavity with small hole that will work as flow integrator, and the other terminal left open to inner spacesuit volume. The hole's diameter and cavity volume will determine how fast and for how long the air will be pushed in and out of the cavity when inner pressure changes (refer to Figure 31, left). From variations in the pressure measurement, the operator's breathing rate can be calculated. Unfortunately, this method will work only if human inside the suit is stationary.

A second approach uses a sensitive gas flow meter which can be located in front of mouth (for example, on the microphone). Such sensors use thermal conduction effect: by measuring the temperature drop in a thin high-resistance wire, air speed can be determined. This approach also has a problem; however, the spacesuit life support system creates an additional air flow in helmet

area above the head. This additional air flow makes the component due to breathing difficult to distinguish. To alleviate this problem, special pipes can be stuck into nose as is done in hospitals. This isolates the air flow due to breathing. Obviously this is not a solution for a spacesuit.

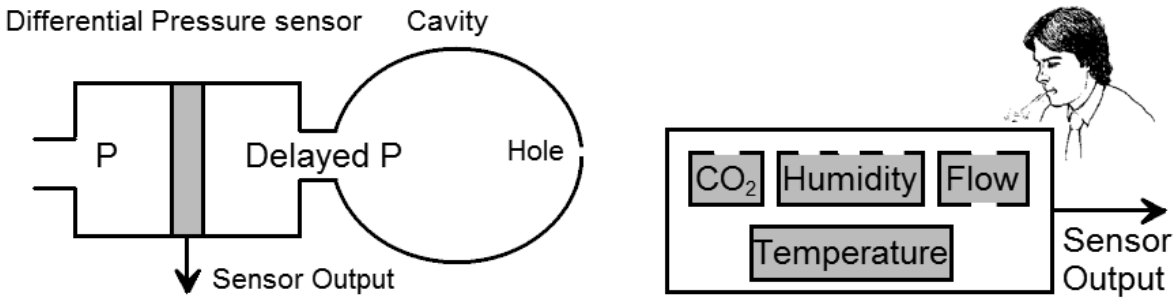

Figure 31. Respiration rate sensor constructions. Solution based on delayed differential pressure measurement (left) and exhalted air properties monitoring (right).

A similar approach could use a fast-response temperature sensor, humidity sensor, or CO_2 sensor located close to nose and mouth. Exhaled air has a higher temperature, humidity, and CO_2 levels than ambient air, causing the sensor's response change.

A third approach detects respiration by monitoring chest displacement. This can be accomplished using both contact and contactless sensors. Doppler-based sensors use an ultrasound generator which is directed toward the chest. The reflected sound waves are then received and processed. Chest movement toward and against the receiver produces frequency shifts between incident and reflected signals, which allows the sensor to detect breathing cycles. Ultra-wide band (UWB) radars for short-range remote object detection can also measure chest motion as well as heart beats [58].

For the WHM device, a contact piezo-electric chest displacement transducer was selected: Pneumotrace II Model 1132, manufactured by UFI. This sensor generates a linear

signal proportional to changes in thoracic circumference. It consists of a flexible distensible belt with built in piezo element, which is typically an ionic bonded crystal (barium titanate and seignette salt are classical examples of such structure). Its positive and negative ions form dipoles that balance each other in rest condition, when crystal structure symmetry is not disturbed. But under mechanical stress, the crystal deforms and a net dipole moment takes place producing an electric field across the crystal.

During breathing in cycle, the sensor belt stretches and a mechanical force is then passed to the crystal. Charge appeared on its edges can be converted to voltage and amplified using a corresponding circuit. The sensor input resistance is 100 MΩ, capacitance is 2.2 uF. Its peak level ranges from 20 to 200 mV and depends on many factors and parameters such as humidity, temperature, human's lungs volume, and breathing deepness. A picture of this sensor is presented in Figure 32.

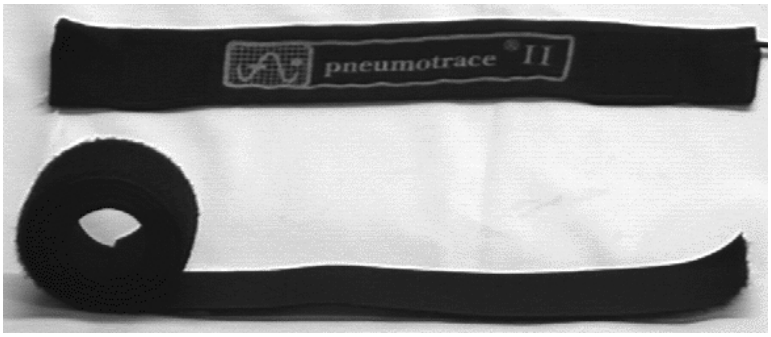

Figure 32. Respiration sensor Pneumotrace II Model 1132.

One problem with measuring chest displacement is that some people breath by expanding their stomach more than their chest. For that reason, the Node respiration sensor AFE contains two independent channels, and signals from two sensor belts must participate in respiration rate calculation algorithm. In Figure 33, a mini USB type B receptacle is used to attach both sensors. A charge mode amplifier circuit is built around U25 OPA2347 (TI) rail-to-rail high-input

impedance op amp. By charging C60 and C67 feedback capacitors, it balances the injected into the negative input charge. R78 and R82 are required for negative terminal DC biasing and feedback capacitor leakage, preventing the op amp from drifting to saturation. These components define the low cutoff frequency of the circuit. R79, R83 and internal sensor capacitance (along with connection cable capacitance) determine the high frequency roll off. Charge produced by a piezo crystal decays with time due to its internal and AFE impedances. Since the signal may reverse its polarity during deep breathing out and fast belt constriction, the output signal is biased at +1.25 V, making it convenient for unipolar ADC to digitize the signal. Transient voltage suppressor D11 protects the input circuit from ESD spikes.

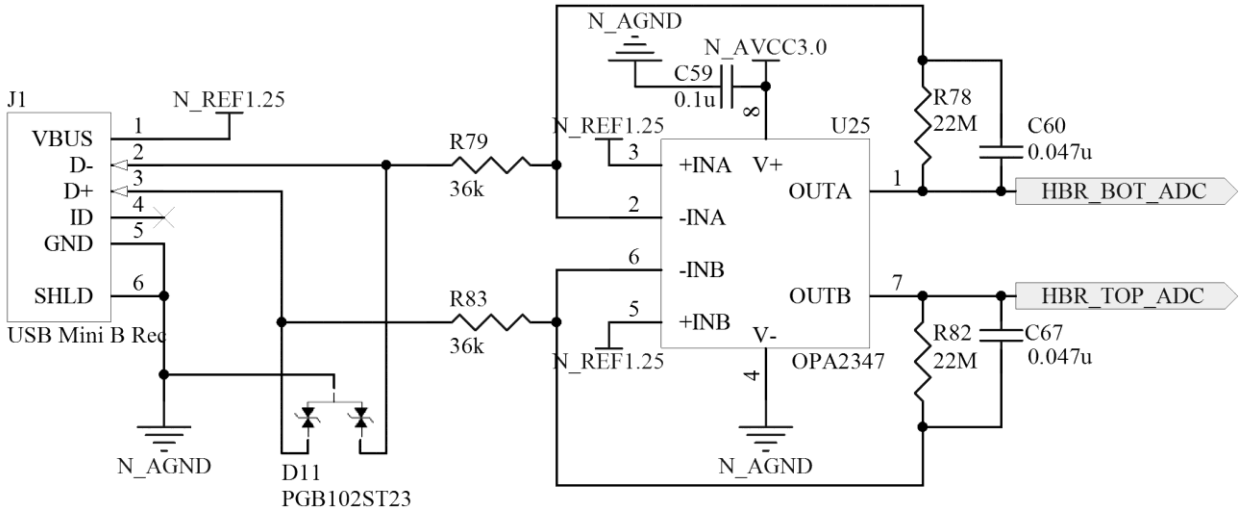

Figure 33. Respiration rate sensor AFE schematic.

Respiration sensor AFE simulation schematic and frequency response is presented in Figure 34. To model the piezo sensor behavior, a voltage model was used (VS, RS and CS). The gain of approximately 45 is needed for respiratory sensors we purchased to deliver a strong signal to the ADC. Amplifier components were selected to create a 0.15…2 Hz band-pass region, which corresponds to human's respiratory rate range.

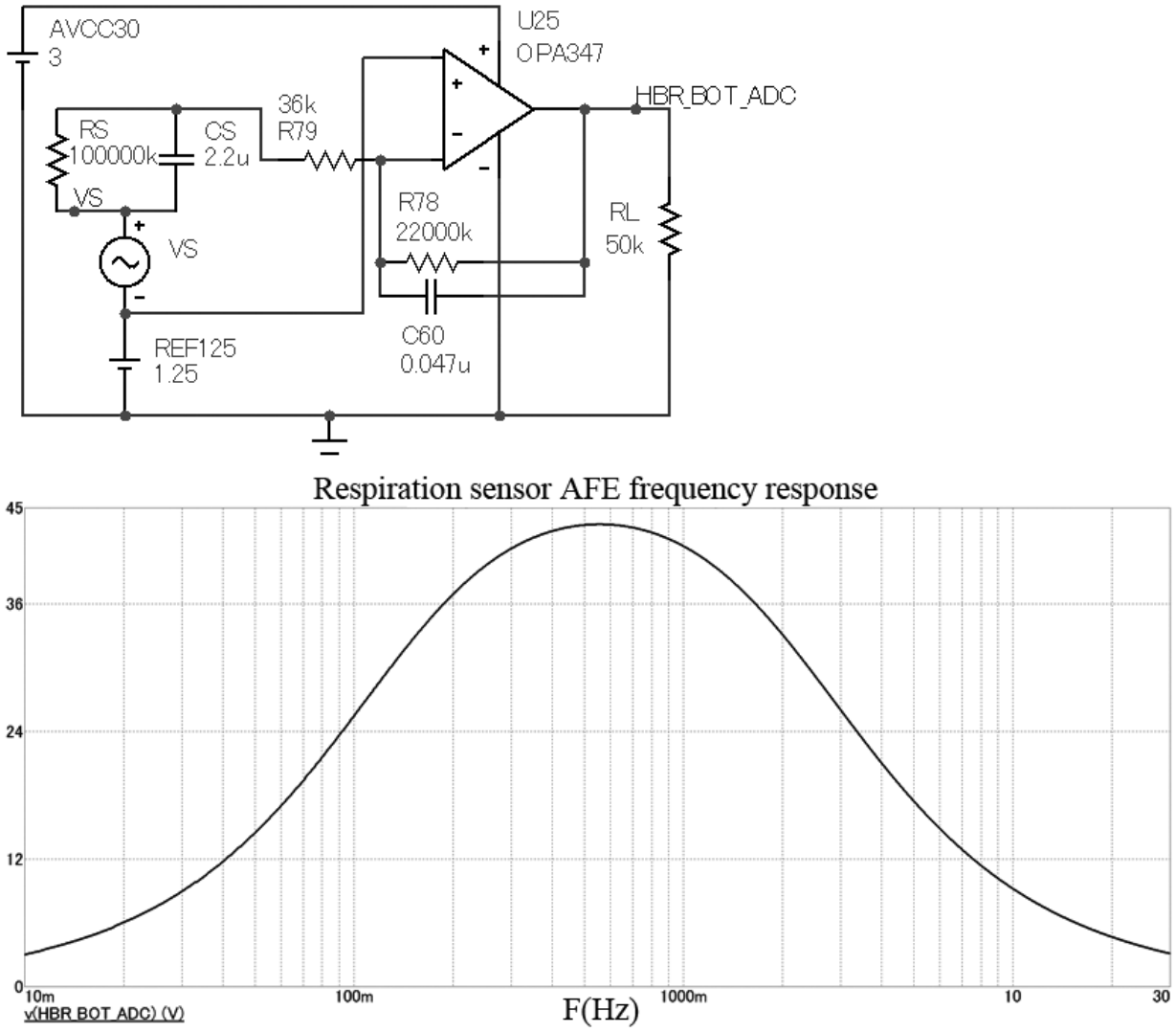

Figure 34. Piezoelectric respiration rate sensor AFE simulation schematic (top) and its frequency response (bottom).

As a sidelight, UFI used to make respiration sensors based on resistive-strain sensing elements that changes resistance under deformation. These elements produce much more predictable parameter change and the aging problem is not so significant. However this product is currently positioned as obsolete because it requires an excitation voltage. On author's opinion, this is not a major problem whereas the piezo sensor's two year operating life is. The author would like to see the resistive strain sensors brought back.

Figure 35 presents the signal conditioning circuit time-domain response using an input signal with 40mV amplitude which was obtained during the test of particular respiration sensors. The sensor's high-frequency noise is considerably reduced by filtering. Once filtered, the respiration rate is determined in software.

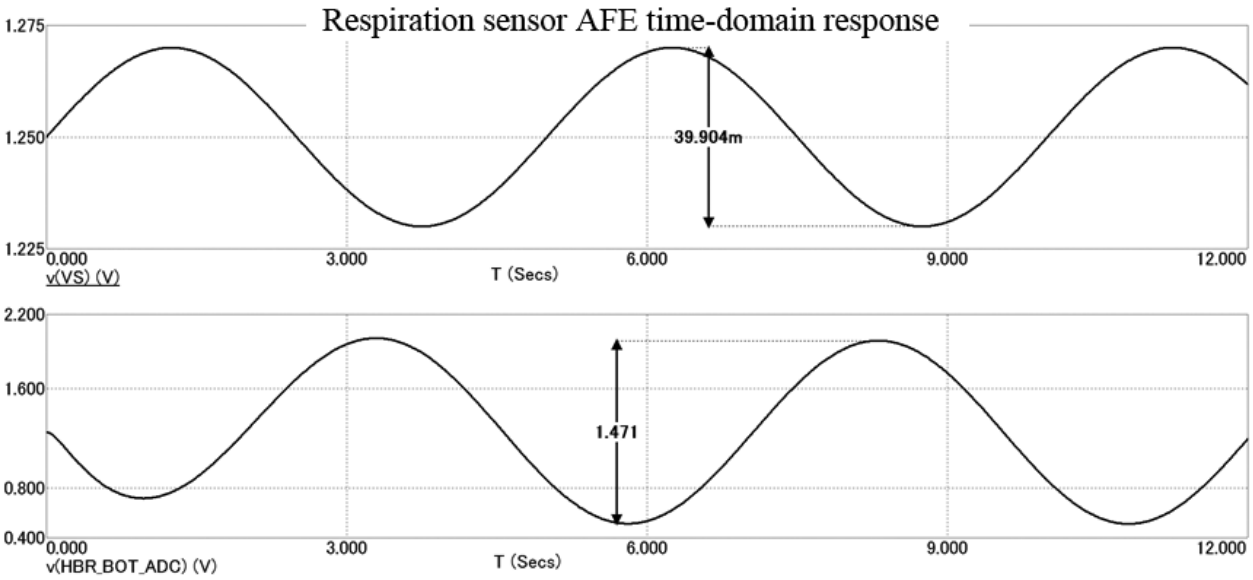

Figure 35. Piezoelectric respiration sensor AFE time-domain response.

3.4. Gas Sampling Chamber

The Node device also contains a gas sampling chamber where CO_2 and O_2 concentrations, temperature and humidity analysis are performed. This chamber represents a separate section inside the enclosure, isolated from the rest of the inner volume. By locating sensors within the chamber, a sample of the breathing mixture can be taken not only at the Node mount place, but also 10-15cm away from it using flexible pipe. The life support system of the spacesuit constantly injects fresh air into the helmet area, which creates a normal air movement along with normal gas convection due to the temperature differences. In spite of this, the air must be additionally pushed to the sampling chamber to ensure the minimum volume flow rate (5…15 mL/min) required for gas sensors and an adequate response time. This task can be

accomplished using either a pump or a fan.

A very attractive solution is to utilize a gas micro pump. Xavitech manufacturers such devices, with the P200 model being a candidate for the WHM application (Figure 36, left). This pump has a small size (37x21x21 mm), weighs 40 grams, operates over the range 3.2…26 V, and only 50 mA is required to produce 400 mL/min air flow and 45 kPa static pressure [59]. The axle motion frictionless motor has a long operation time which is the main concern for this kind of devices. The pump is calibrated at the factory and the control is done through the UART interface. The advantage of using this pump is high reliability, precise air flow and pressure control along with high static pressure it can create, which means that long small-diameter pipe resistance can be simply overcome. This is the reason why it is widely used in aerospace applications.

The disadvantage of this micro pump is its cost: around $450 as of Nov 2011.

Other micro pumps do exist, such as those made by Parker, Alldoo, Hargraves etc. However, most of these have a relatively high power consumption of 0.35 W or more and tend to be noisy and vibrate. Many such models are not designed for long-term continuous use as well.

One exception is the mP-5 (Bartels), shown on Figure 36 (right). It has very low power consumption and is extremely small weighing only one gram. This pump contains an embedded control circuit that allows the user to program operation parameters ranging from zero to 15 mL/min flow and 6kPa static pressure for gases [60]. This pump uses a flexible diaphragm that is supported by piezo element. High voltage applied to its edges cause crystal deformation and diaphragm fluctuation. Valves control the propagation direction of gas or fluid. Analogous pumps can be purchased from Microjet, Microbase and other companies.

Figure 36. Micro pumps: Xavitech P200 (left), Parker T2-05 (middle), Bartels m-6 (left).

A fan can be used instead of pump, if air flow channel length is short and diameter/section is wide enough. This low-cost solution is used in current Node version. The ultra-compact fan used F16EA-03 (Copal) produces 12 L/min air flow and 4.7 Pa static pressure [61]. Power consumption is 20 mA at 3.3 V and free air flow. Figure 37 (left and middle) shows fan control circuit and fan general view.

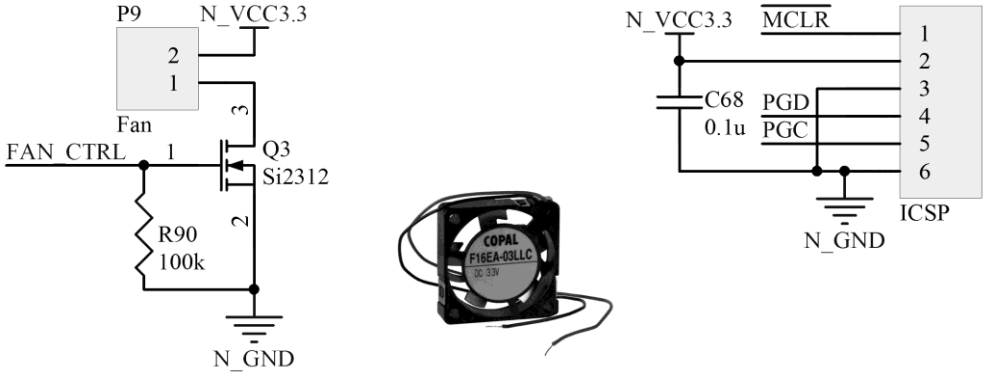

Figure 37. Fan control circuit (left), F16EA-03 fan (middle) [61], MCU ICSP debugging port (right).

Transistor Q3 operates like switch, and R90 prevents its gate from floating. Current device version has no air flow sensor and hence no control of the fan's rotational speed. This could be added in the future using PWM and a flow sensor, however. The fan is mounted inside the gas sampling chamber, and is connected to the main board through P9 connector.

3.5. Radio Transmitter and Microcontroller

Figure 37 (right) depicts schematic for the microcontroller in-circuit serial programming interface (ICSP). It is used by PIC24 MCU for flashing/debugging operations, and utilizes MCLR (reset), PGD (bi-directional data) and PGC (clock) lines. The power supply line is also routed to the ICSP port and is used by the external device to determine MCU operation voltage to generate signals of an appropriate level. Microchip makes a number of hardware debuggers with different features and functionality. The most popular of these are the ICD2 and ICD3 debuggers and their modifications that basically differ in programming speed and list of supported microcontrollers as presented in Figure 38.

Figure 38. PIC MCU family debuggers: ICD 2 LE (left), ICD3 (middle), Olimex ICD2 (right).

Radio communication between the Node and the Base is done using a special module. This solution was selected in order to reduce the design time and avoid the need of matching circuit and antenna calculations which is considered outside the scope of this thesis. Various OEM modules are available from manufacturers, with various frequency operation range, modulation type, transmitting power and receiver sensitivity, and communication protocol. For the Node device, the 900MHz frequency band was selected since it doesn't require a license (in the US) and signal propagation is fairly good for non-line of sight communication conditions in

comparison to 2.5GHz range. Communication speed is not critical for the WHM application, due to the small amount of data and low update rates being used.

Digi International makes the XBee-PRO® 900 radio module, which is suitable for the WHM. It covers the range of up to 10 km under line-of-sight condition. The transmitter power is 50 mW, receiver sensitivity is -100 dBm, power supply voltage is 3.3 V. With the WHM, this module uses 210mA in transmission and 80mA in receiving mode. Frequency hopping spread spectrum (FHSS) method is used for transmitting the data. Another module XBee-PRO® XCS offers twice the transmitter power and higher sensitivity which significantly extends the range, but also increase power consumption. Both modules use IEEE 802.15.4/ZigBee® - reliable, scalable and secure communication protocol that supports self-healing and self-organizing wireless network operation. They can be programmed to operate in point-to-point and point-to-multipoint network topologies, and support various addressing modes. Module configuration and data transmitting/receiving is done using UART interface and simple AT commands. The disadvantage of these modules is relatively high price and power consumption.

Atmel fabricates the ZigBit 900 compact modules that offer 120 dB link budget to cover 6km range in addition to the wide range of supporting analog and digital interfaces (general IO, ADC lines, UART, SPI etc.) Additional features can be activated by adding user-defined code to the same ATmega1281 microcontroller that drives ZigBee stack. Low power consumption (15/20 mA) and small size make it very attractive for the current application, however it is preferred to use a module with some transmission power reserve and adjustment that can be used if wider range is needed or worse environment conditions occur.

Radiotronix makes WI232FHSS radio communication modules that were found to be an ideal solution for the WHM. They can operate in true UART to antenna mode, which means that

after configuration, the microcontroller uses the UART interface to send and receive the data. The WI232FHSS handles the rest of the communication without user intervention save the reading of some additional status lines. WI232FHSS-250 version has 250 mW adjustable transmitter power output and 105 dBm receiver sensitivity (at lowest possible data rate of 2400 baud), which in case of using 2.2 dBi ½ wave dipole antenna, gives 133 dB link budget. Free space loss L can be estimated using the reduced Friis equation

$$L = 36.56 + 20 * \log(f) + 20 * \log(D) \quad (31)$$

where f is link operation frequency in MHz, and D is distance between the receiver and transmitter antennas in miles. From this equation, distance can be expressed:

$$D = (e^{0.115} * L - 4.209)/f. \quad (32)$$

The rule of thumb is to have theoretical margin of at least 15 dB, so L is then 118 dB. Line of sight distance under ideal conditions is then around 13 miles. According to the information from this module's datasheet [62], field tests have shown communication range of more than 3 miles outdoors, but at maximum data rate, which assumes much worse sensitivity. Figure 39 shows module's connection schematic (left) and device general view (right).

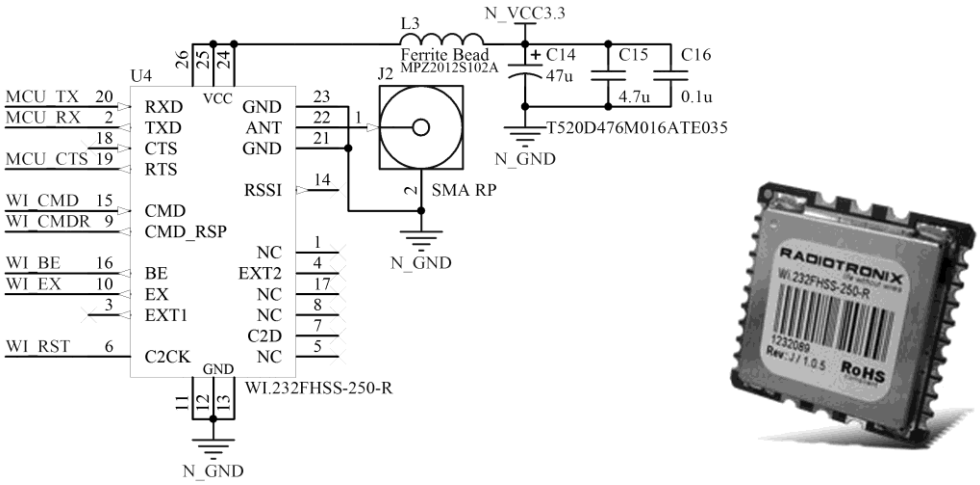

Figure 39. WI232FHSS-250-R module connection circuit (left) and general view (right) [62].

This module needs 3.3 V and 25 mA when receiving, 190 mA when transmitting at maximum power and 3uA when in deep sleep mode.

The WI232FHSS contains internal registers for configuration which are located in both non-volatile flash memory and in shadowed RAM. After reset (either software or hardware), information from flash registers is copied to RAM and can be quickly adjusted, if required, during normal module operation to take immediate effect. Flash registers can also be programmed by the user, allowing the initial pre-configuration to be hard coded.

The UART interface uses TXD (data transmit), RXD (data receive) and RTS (ready to send, which indicates that module is currently busy and no data must be directed to module) lines. The CTS (clear to send) line is not implemented in the current module firmware version. Full duplex operation is supported at baud rates from 2.4…115.2 kbps. The internal buffer size for incoming data is 256 bytes, and data is transmitted over RF in packets. The UART module can be configured to initiate the transmission either when the incoming buffer receives a set number of bytes or when the delay between consecutive bytes is longer than specified value. BE line indicates if receive/transmit buffer is empty.

The receiver module utilizes carrier sense multiple access (CSMA) mechanism, which checks if any other module is transmitting before initiating its own transmission. If this happens, the UART module receives the data and if address in received header package corresponds to the module's address then the data is extracted, verified, and directed to the receive buffer. Otherwise the data is discarded. After this, the module postpones transmission for a random period of time and tries the procedure again.

FHSS is a special radio communication protocol that provides a reliable high-quality link for use in the presence of electromagnetic interference and reflected signals. The concept of

FHSS is as follows. The operation frequency range of 902…928 MHz is split into 32 narrow, non-overlapping sub-ranges called hop indices, the sequence of which is determined by a hop table. Six unique hop tables are available for user selection, each containing 26 hop indices. Each data packed which is scheduled for transmission is split into chunks, each of which is then transmitted using a frequency range that is determined by the current hop index. For the first chunk transmission, a random hop index from the table is selected. After it is transmitted, all devices in the same network switch to next hop index in table, and transmission of the next chunk is done on its corresponded frequency. If transmission was not successful, it will be repeated in next hop index frequency. Synchronization is lost after the last chunk has been transmitted or the module has detected two consecutive hop indices without the data. Hop indices are only known to devices that share the same network.

Three different addressing modes are supported by WI232FHSS: MAC (media access control), User, and User Extended. The MAC mode is best suited for point-to-point communication and uses a unique 4-byte address that is programmed at the factory. When any message is received, the RF engine checks if the destination MAC address (which is located in the message's header) matches the module's factory MAC address or 0xFFFFFFFF (which indicates a broadcast message). If so, the message will be processed.

This method is used in the WHM to create a network star topology and can be easily extended to a tree topology. The latter two access methods (User and User Extended) work best for mesh networks with many nodes. They use a customer defined module ID and masking for routing, which allows it to create subnets. For all modes it is possible to enable the acknowledge feature, which ensures message delivery by requesting confirmation from the addressee module. If acknowledge has not been received, the module will retransmit message after random delay.

To prevent a message from being sent indefinitely, a maximum number of retransmissions can be specified.

The receiver module supports three low-power states: standby, sleep and deep sleep. These states differ in power consumption, wake up time and method. Since wake up time is not critical for this application, deep sleep is used in the Node to save power. The UART module is put into this state by sending special command over the UART, and is woken up using C2CK pin assertion. An exception engine helps to monitor failure conditions such as an internal buffer overflow, a register write error, a bad message CRC (cyclic redundancy check) etc. The output pin EX will be set high if one of these errors occur and will not return low until the exception register is read by the host. Selective exceptions can be masked out to prevent the EX pin from going high when they occur.

The receiver module can be configured to operate either in automatic or manual gain control mode. High gain adversely affects the linearity of the receiver. Higher linearity improves module performance in high-interference environment, and higher gain does the same in low-interference environment. In automatic mode these parameters are adjusted automatically. The received signal strength indication (RSSI) is updated after every successfully received package, and is available for user through register reading or analog output pin RSSI (not used in current application).

The remaining signals presented in Figure 39 are as follows. Input CMD is used to switch the module to command mode, in which it is possible to read/write registers and execute service commands through UART interface. Output pin CMD_RSP is high when the data on TXD pin is a response to command or register read value. Both signals are used to distinguish between actual data received/transmitted over air and commands. The ANT line has to be

connected to the antenna through SMA connector J2, which has transmission line impedance is 50 Ω. Components L3, C14, C15 and C16 create filter that prevents high frequency spikes from getting to power supply line.

3.6. Microcontroller

The last component considered in this chapter is microcontroller itself. All blocks described previously are connected to it as presented in Figure 40. A PIC24FJ series microcontroller is used, which is a 16-bit device with a modified Harvard architecture (separated command and data buses) and an extended command set. It has 16 general registers, a vector priority interrupt system with guaranteed response time of 5 instruction cycles, flexible addressing modes, hardware loops, multiplier and divider, built-in generator with various sources and phase-locked loop (PLL), advanced peripheral set with pin remapping and many other features [63]. A single command is executed using 2 cycles, which improves performance and significantly reduces power consumption. Up to 12M bytes of program memory and 64k bytes of data memory is supported.

Under normal operation, the supply current is 3.5 mA at 4MIPS, 3.3 V supply voltage and on-chip regulator enabled. Nano Watt XLP technology allows getting a very low deep sleep current of 20/500 nA depending on watch dog and/or real time clock settings. The power supply is connected to MCU through VDD, AVDD, VSS and AVSS lines in parallel with decoupling capacitors C69, C70, C71 and C72. Even though microcontroller has separate analog and digital power supply entries, both are internally connected to the same line and therefore only digital 3.3 V source is used along with proper ground separation. A built-in 2.5 V voltage regulator for the core is enabled by connecting DISVREG to ground. Low-ESR capacitor C73 maintains its stability. An analog 2.5 V positive reference for internal 10-bit ADC is connected to VREF+

pin. One bicolor LED connected to J3 is used for the Node status indication. Pull-ups R88 and R89 are required for I2C bus operation. Low-ppm 32768 Hz quartz resonator Y2 along with C74 and C77 is used as timer clock source for precise timing reference, while for instruction clocking fast RC (FRC) internal 8 MHz generator is used.

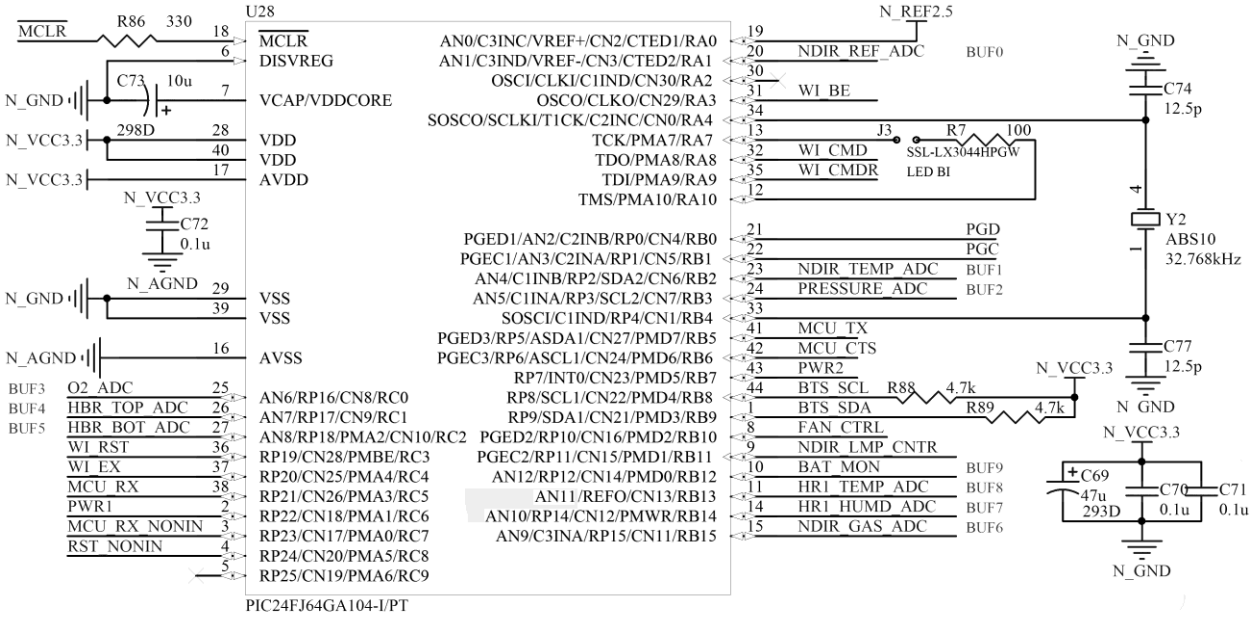

Figure 40. Controller PIC24FJ64GA104 connection circuit.

At this point, after all components have been selected, the estimated average current supplied from 2.4 V battery source was found to be 100 mA. With a battery capacity of 2 A*hr., this results in a battery life of 20 hours, meeting the system requirement. With software optimization, this can be significantly extended.

3.7. Summary

In this chapter, component definition and selection for the Node unit of the WHM project was accomplished; schematic drawings were created along with simulation. Sensor comparison was presented and decisions of which devices to use were made.

CHAPTER 4. NODE BOARD, ENCLOSURE AND FIRMWARE DESIGN

4.1. Introduction

Each node in the WHM is a mixed-signal, low-complexity, and low-power device. In this chapter, the circuit board layout for the node's circuit board will be presented, along with the design of its enclosure.

4.2. Node Board Layout

4.2.1. Selection of number of layers and ground separation

The first parameter to determine in designing the node's printed circuit board (PCB) is the number of sides to use. The simplest and least expensive option is a single or double sided board without metallization. Such boards work well for simple layouts with low component density. Their main disadvantage is low reliability resulting from the copper traces peeling after mechanical and thermal stress as well as humidity and flux absorption.

In order to improve reliability, double-sided boards with metalized vias can be used. Such boards have high isolation properties and low parasitic track capacitance. They can be fabricated with a minimum thickness and with good mechanical strength. The down for such boards, however, is with the time it takes to design such a board: 4-6 layer board equivalents can be routed within couple hours using basic layout rules and guidelines while 2-layer design may take several days and require an experienced engineer. Further, even small changes in a 2-layer board usually require complete layout redesign.

With more layers to rout traces, multi-layer PCBs greatly simplify routing a circuit - to the point that auto-routers can be used. For complex circuits, high-speed devices, and/or high density layouts containing ball-grid array chips, there may be no option other than using a multi-layer PCB. These boards have problems, however. First, they have the worst isolation

properties and lower long-time reliability under vibration and temperature cycling conditions. Special technologies and layout approaches (including microvia, via doubling, the use of blind holes, pre-metallization etching etc.) were developed to increase the board reliability, increase life-cycle, and reduce scrapping.

Double-sided PCBs with metallized via were selected for the Nodes. The small production run for this project makes cost not as important in the design process. The greater reliability and improved isolation properties are more important. Advanced Circuits provides a very affordable prototype price, high fabrication quality and fast turn-around time. The design requirements for their $33 standard double-sided board are 0.15 mm track width and clearance, 0.4 mm hole size. Board material is 1.58mm FR-4 with 1 oz. copper plating. Green solder mask and both sides silk screen for labeling are also included in price.

The minimal number of high-speed signal lines in the Node allows for this option. The high-speed lines that are on the board, such as the radio transmitter and pulse rate measurement, can be accommodated with proper internal layout and shielding.

Analog and digital ground separation techniques have been utilized in the Node's PCB to prevent current pulses in the digital device high-speed logic from affecting the analog signals. Switching power supply, digital and analog circuits are located in different areas with minimal interaction as presented in Figure 41. Since the microcontroller contains both digital and analog blocks, it covers both ground areas. In order keep noise on the ground trace from affecting the radio channel, antenna transmission line and connector ground, these are also separated from the main digital ground based upon layout recommendations from [62]. Further, analog signal traces are made as short as possible to reduce interference.

To minimize noise on the analog signals, a minimum width of the analog traces must be

maintained. The right selection of the trace widths is based on follows.

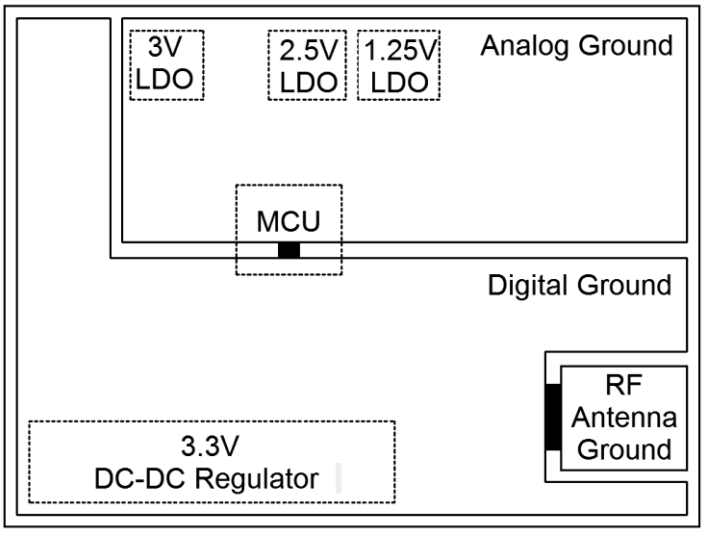

Figure 41. Ground polygon schematic location on the Node PCB (top side).

The range of the microcontroller's ADC is 2.5 V, which corresponds to a resolution ±0.5 bit or ±1.2 mV (0.049% full scale). The ADC input impedance is 2.5kΩ. The resistivity of copper at 25°C is $1.724*10^{-6}$ Ω and thickness of 1 oz. copper plating is 0.038mm. For the voltage at the A/D to be accurate within 0.049% of full scale, the trace resistance must be less than 1.2 Ω. Assuming a trace width of 0.2 mm, the maximum trace length is 1.2 Ω/2.4 mΩ/mm = 500 mm. Since this is considerably larger than the node, trace lengths are not a significant problem with this design.

4.2.2. Component placement

With trace lengths not being an issue, the placement of the components is somewhat arbitrary. The placement used in the Node is presented in Figure 42. All modules and sensors (except pressure sensor) are located on the top side. Special attention was paid for the DC-DC switching regulator component placement to maximize the efficiency and reduce noise. This includes appropriate grounding and placement of inductors and capacitors. The oxygen and

carbon dioxide sensors are connected to the board using gold-plated sockets in order to avoid overheating during soldering and simplify the procedure of sensor replacement. All decoupling capacitors are located as close as possible to the power supply pins on each chip. High-current traces (RF module and NDIR lamp) are sized for their expected currents.

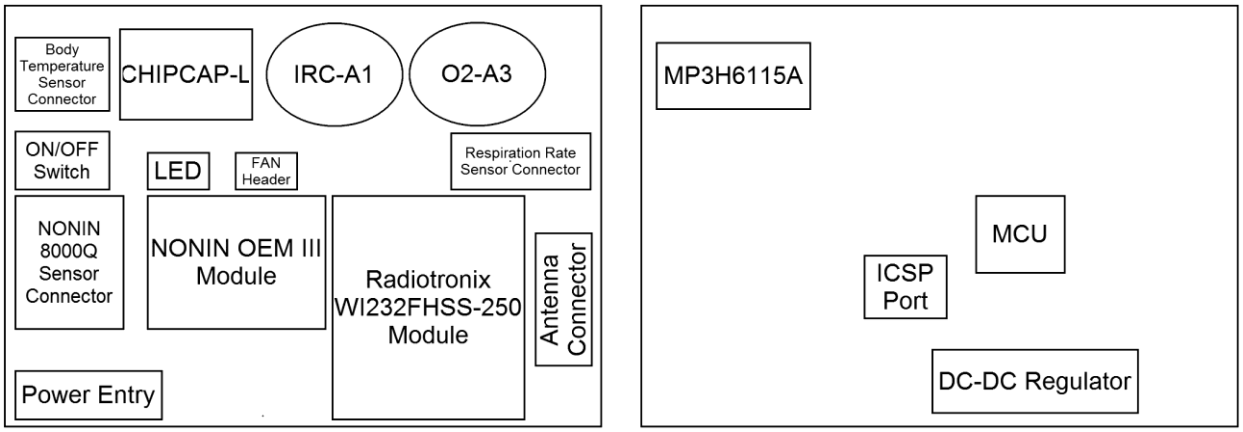

Figure 42. The placement of sensors, connectors and major parts on the bottom layer (left) and on the top layer (right) of the Node PCB.

The complete Node main board layout is shown on Figure 43 (top layer) and 44 (bottom layer). Silk screen layers with component designators and labels are shown separately from copper layers for clarification purposes. ID label represents Node wireless network address.

The antenna is connected to the main board using SMA-RP connector. A signal path between this connector and the module's RF output pin represents a transmission line which must have a characteristic impedance of 50 Ω to meet the module and antenna specification. Its lossless (frequency-independent) calculation was done using Polar Instruments Si9000 transmission line field solver software instead of using manual calculations. Based on the proximity of the bottom ground plane to the signal trace, an RF wave can mainly propagate either between the trace and bottom ground plane gap (air) or between trace and top ground

plane gap (FR-4). The former was selected for the design, in which the transmission line is called surface coplanar waveguide with ground. Its structure is presented in Figure 45 with input/output parameters presented in Table 2.

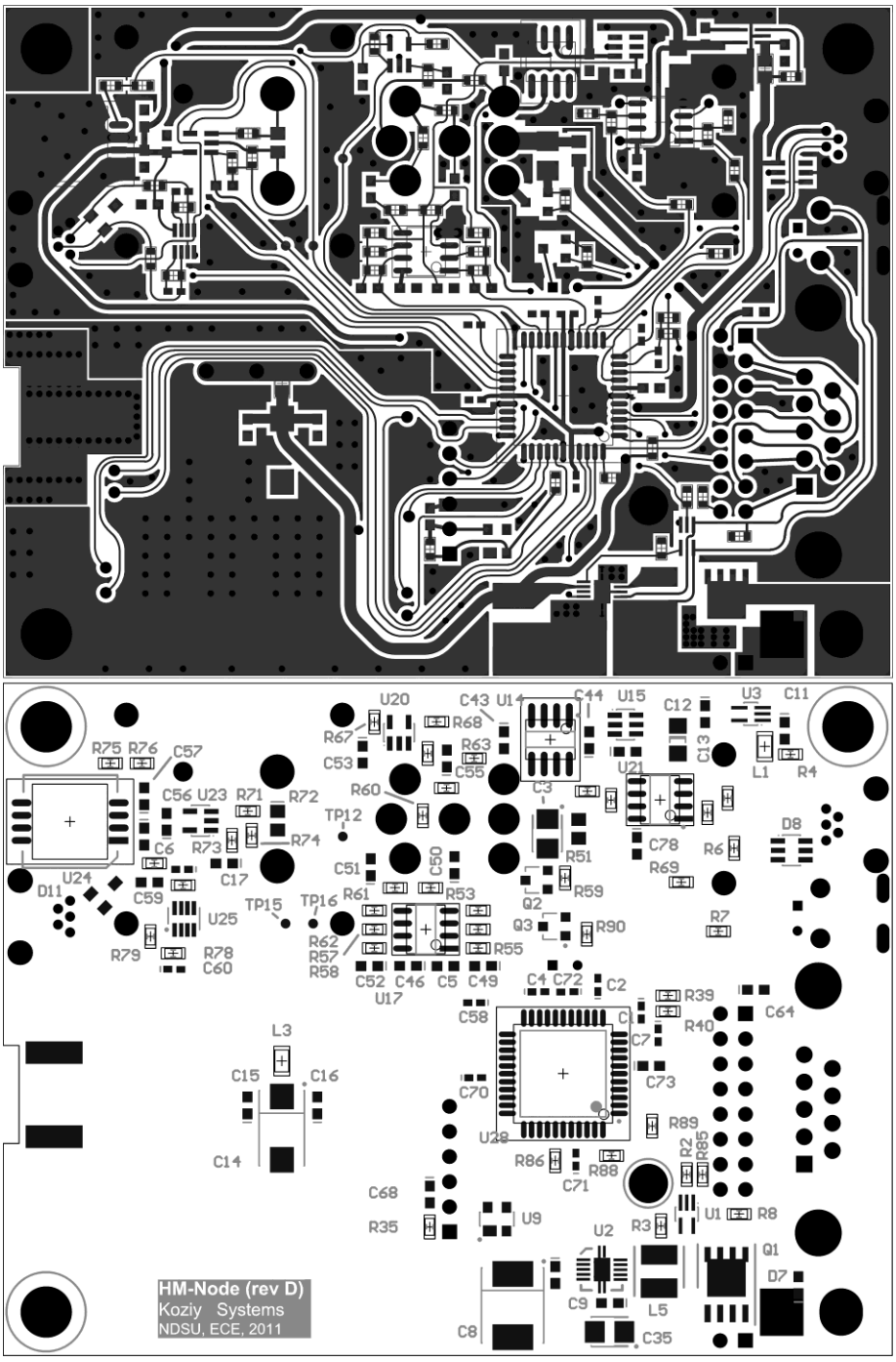

Figure 43. The Node PCB layout (copper and silk screen with pads, top layer).

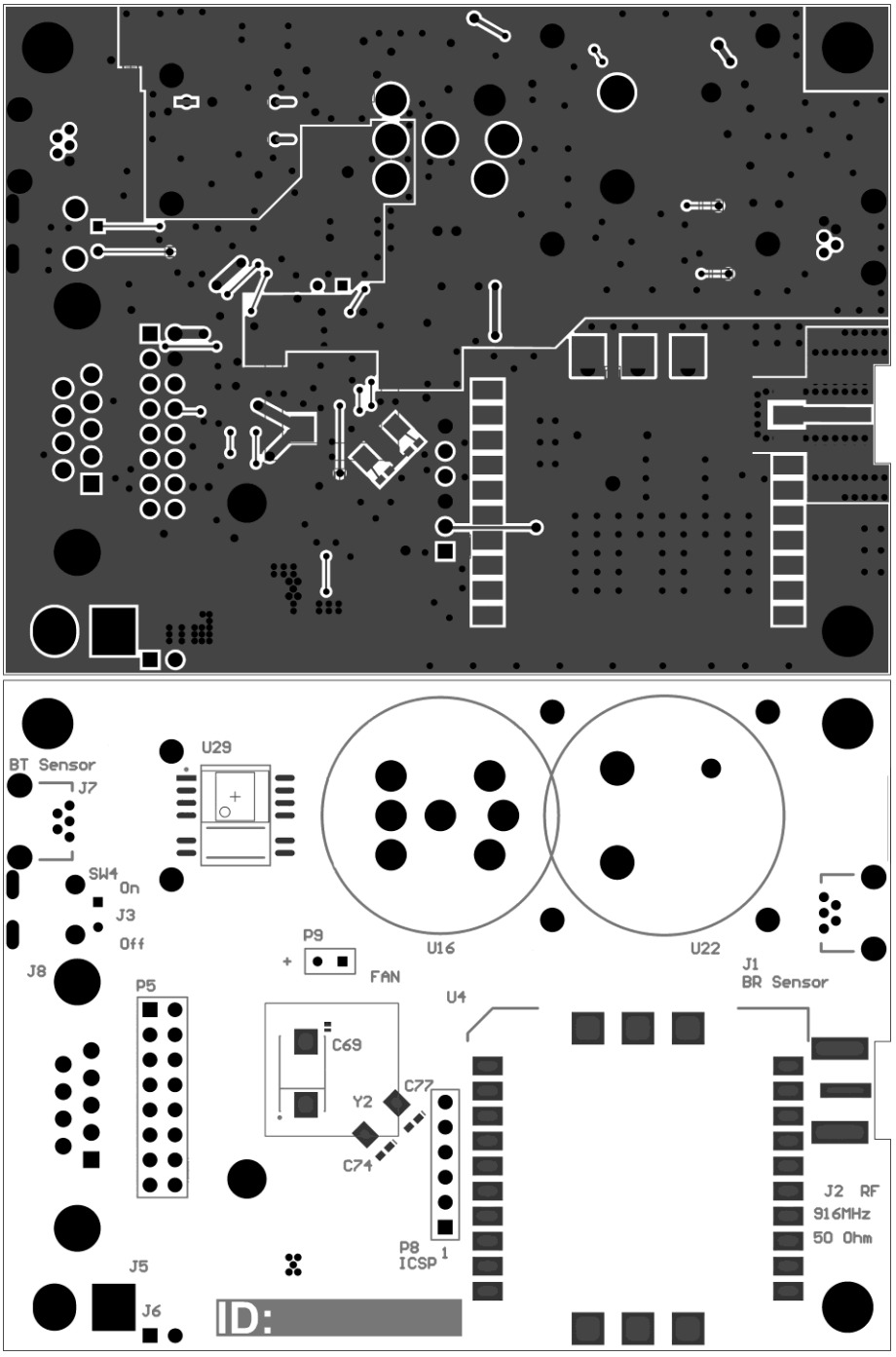

Figure 44. The Node PCB layout (copper and silk screen with pads, bottom layer).

In our case, it is assumed that W1 = W2 due to insufficient information from the PCB manufacturer about their subetching coefficient. The calculated parameter is ground strip separation D1, which is then used in the circuit board software.

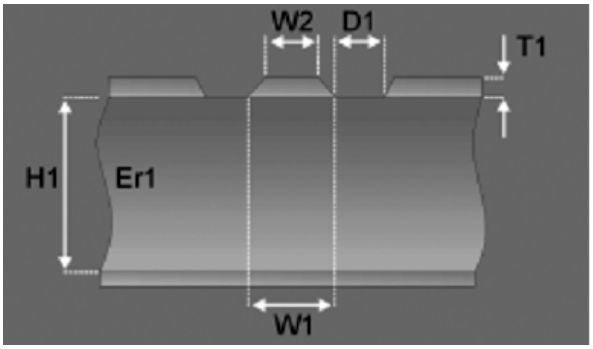

H1 - Substrate Height
Er1 - Substrate Dielectric
W1 - Lower Trace Width
W2 - Upper Trace Width
D1 - Ground Strip Separation
T1 - Trace Thickness

Figure 45. Surface coplanar waveguide with ground structure.

Figure 46 shows the photo of completely assembled Node board prototype. The overall board dimension is 90 x 68 mm.

Table 2. The transmission line parameters for the WI232FHSS module and antenna.

Parameter Name	**Units**	**Value**
Substrate Height	mm	1.58
Substrate Dielectric Permittivity @1GHz	-	4.34
Trace Width	mm	1.5
Trace Thickness	mm	0.038
Impedance	Ω	50
Calculated Ground Strip Separation	mm	0.313

4.3. Node Enclosure Design

The Node enclosure was designed using the software package Solid Works. It consists of an ABS plastic top and bottom parts (Figure 47), with the PCB clutched in between. The bottom part has a small hole connecting the inner enclosure volume with the outer space. The absolute pressure sensor is located on this side of PCB. The top part contains the gas sampling chamber that covers the sensors on PCB and separates the sensing volume. An exhaust micro fan is located inside the chamber and has to be mounted and sealed appropriately. A small hole must be drilled in the chamber wall for the fan's wires, which are connected to the header located on

the PCB (refer to Figure 48). Afterwards, the gas chamber must be covered and sealed by cap using epoxy. To make sure that top enclosure hermetically adjoined the PCB along the chamber bottom line, silicon hermetic must be applied.

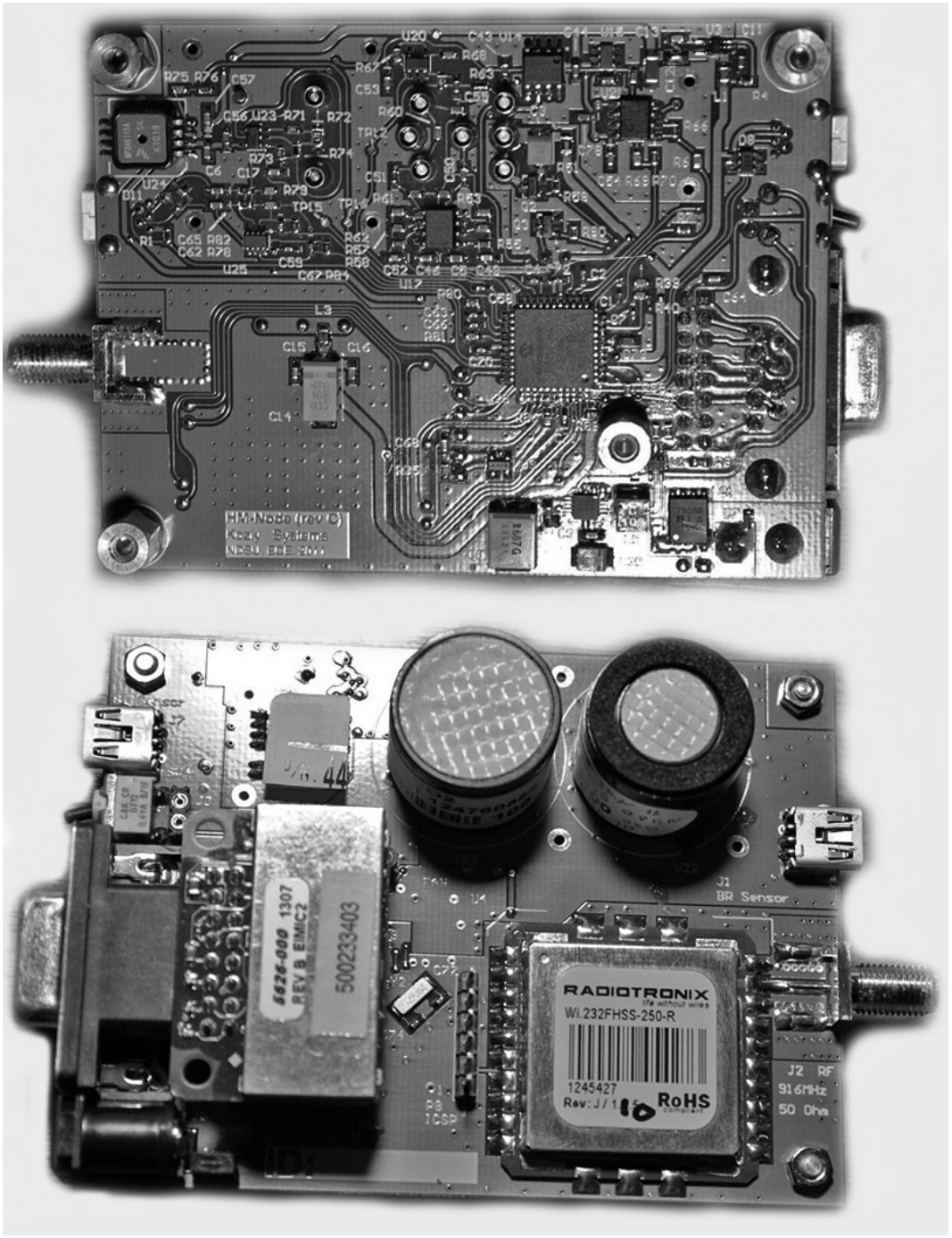

Figure 46. Completely assembled main board of the Node device.

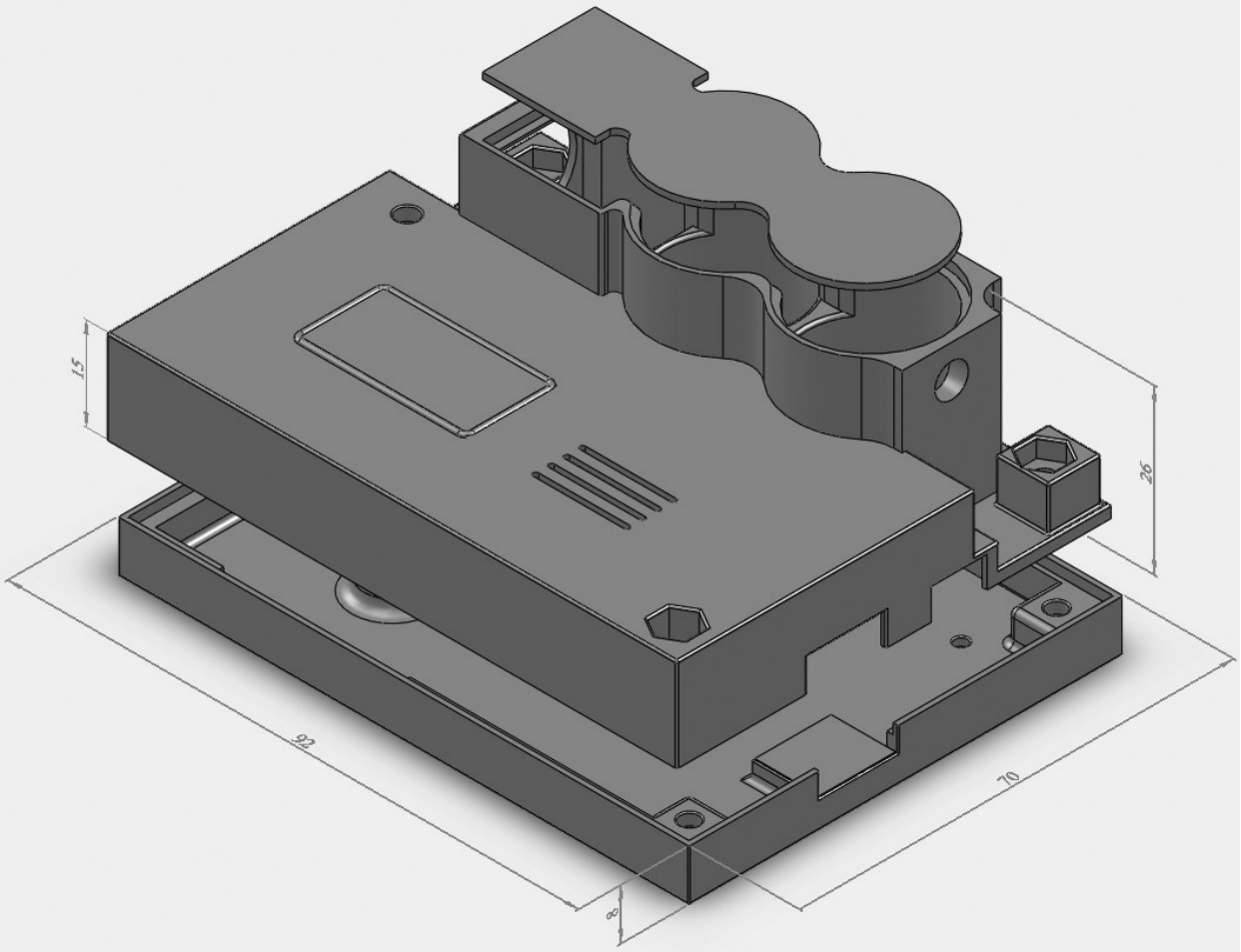

Figure 47. The Node enclosure general view and basic dimensions.

On the chamber side opposite the fan, a threaded hole ¼-28 UNF is created for a barbed straight connector. This connector is used to connect an optional flexible pipe with a 4-5mm inner diameter. One screw #3 UNF (cylindrical head shape with a rounded top) and nut pair is required to attach the PCB to the bottom part, and 3 more are needed to press the top part to the bottom. Figure 49 shows the photo of completely assembled Node device without attached external sensors. The enclosure was fabricated using a Dimension uPrint 3D printer.

The fan draws air through the gas sampling chamber and pipe (if connected). The chamber and pipe creates a resistance to air flow that depends on air speed, internal volume

geometry, inlet opening, and attached pipe diameter and length. This resistance will create some pressure drop, which consequently reduces the effective volume flow the fan can create.

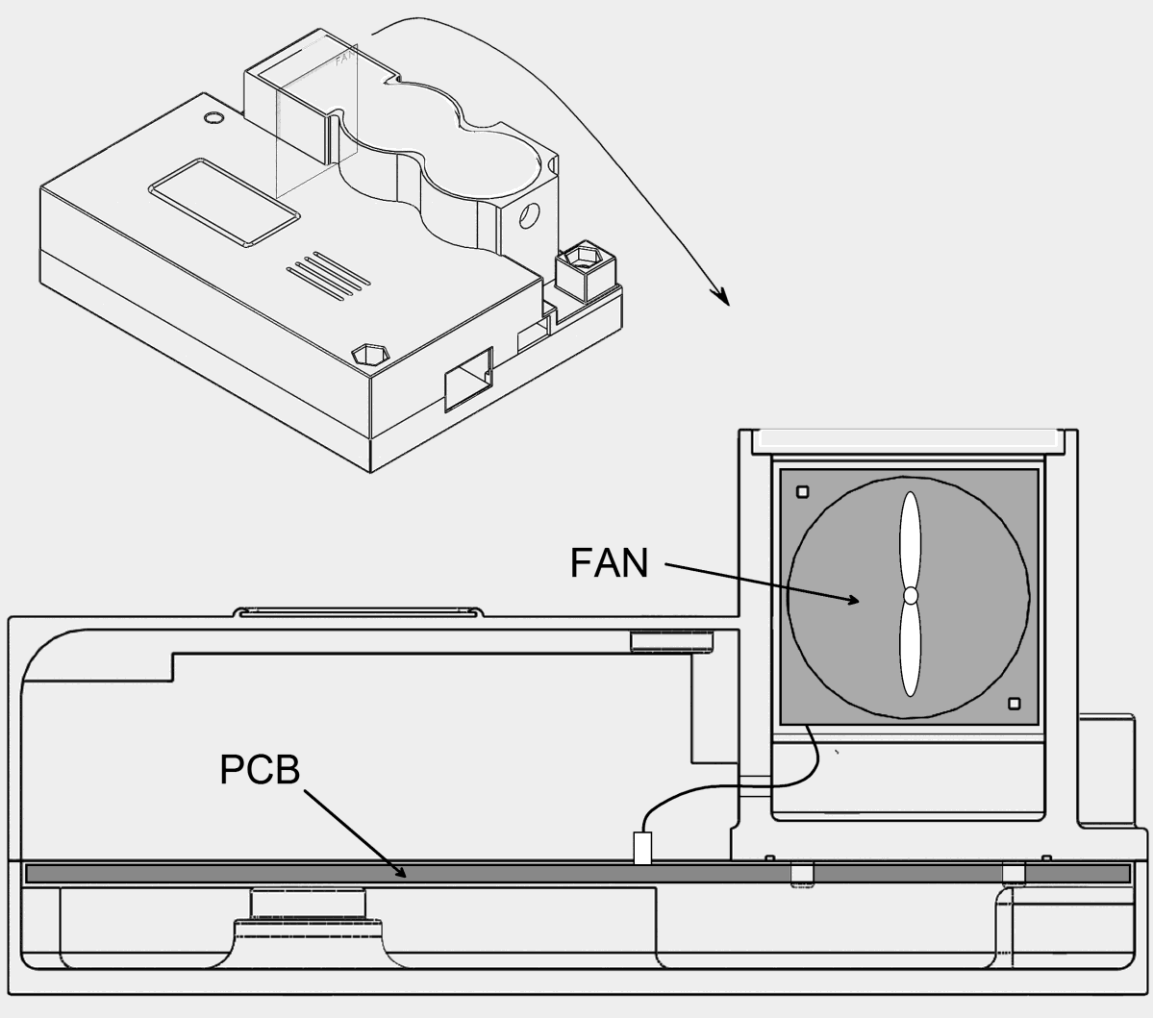

Figure 48. Gas sampling chamber sliced view and fan location.

In order verify that the air flow is sufficient, the gas flow was simulated using an Ansys FLUENT software package. The procedure for this is a follows. First, the inner chamber volume was extracted from the chamber solid model with the result presented in Figure 50. Here, two faces (marked with "+") represent the exhaust fan and inlet opening. To reduce the simulation time, symmetry was used to cut the volume in half. Next, a finite element mesh was generated.

Figure 49. Completely assembled Node device (without external sensors and antenna).

The fan was modeled as an inlet velocity boundary condition of the volume. To specify it, the flow was assumed to be 100ml/min, the minimum amount for an acceptable response time for the gas sensors. The fan's working air gap area AFAN can be calculated though fan geometry. Once known, the flow velocity AV can be evaluated:

$$A_{FAN} = (R_{OUT}^2 - R_{IN}^2) * \pi, AV = AF/A_{FAN}. \quad (32)$$

R_{OUT} and R_{IN} represent fan outer and inner radius which results in $A_{FAN} = 9.6*10^{-5}$ m^2, and AV=0.017 m/s. This sets the velocity boundary condition. The resulting simulated air flow velocity and static pressure is presented in Figure 51 and 52.

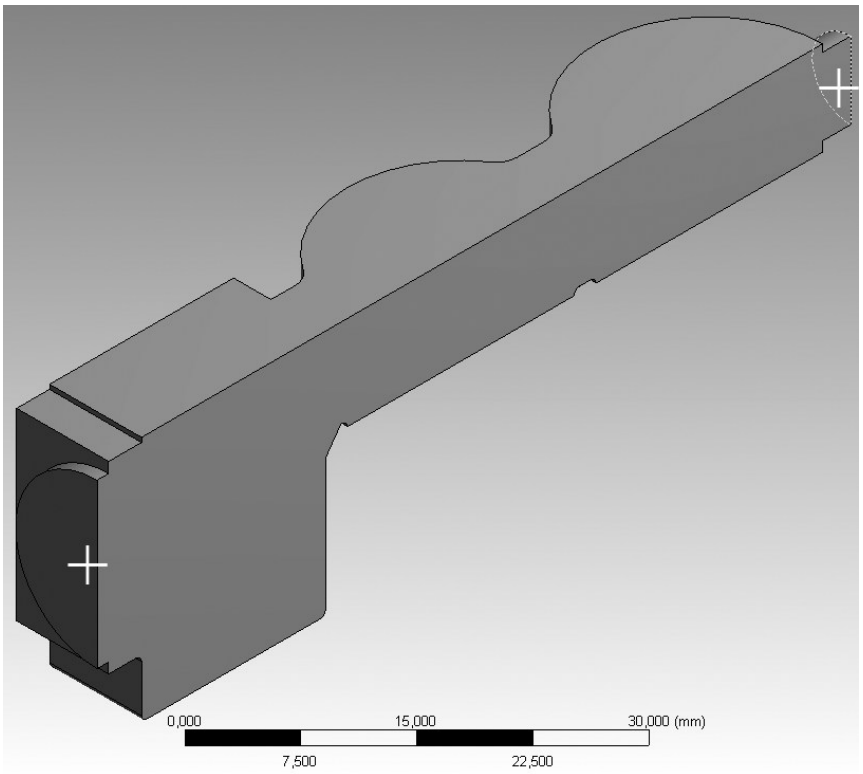

Figure 50. Gas sampling chamber air flow volume model.

The air flow volume at the opening section was found to be $1.46*10^{-6}$ m^3/s or 88 ml/min. As it can be seen in Figure 51 and 52, the pressure drop under this flow rate is very small (0.018 Pa), which will not reduce the real flow by a high degree unless a long pipe is attached. With a 60mm pipe of 5mm inner diameter and without bending, static pressure is 4.4 Pa, which is acceptable. Pipes longer than 100mm are not recommended, however, due to the increased drop in static pressure.

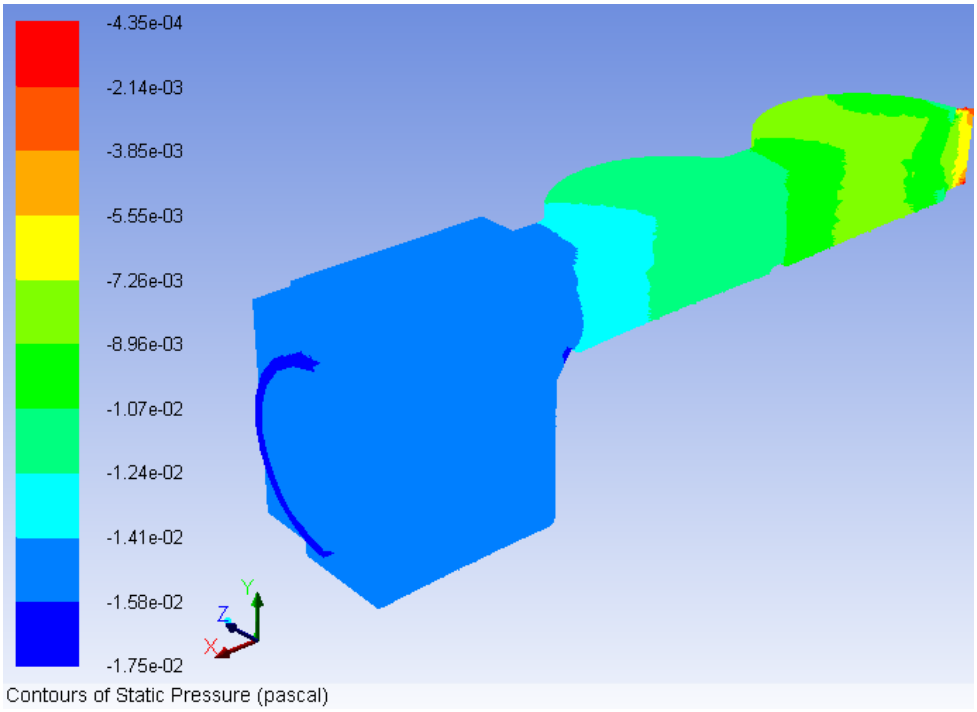

Figure 51. Static pressure distribution in gas sampling chamber volume.

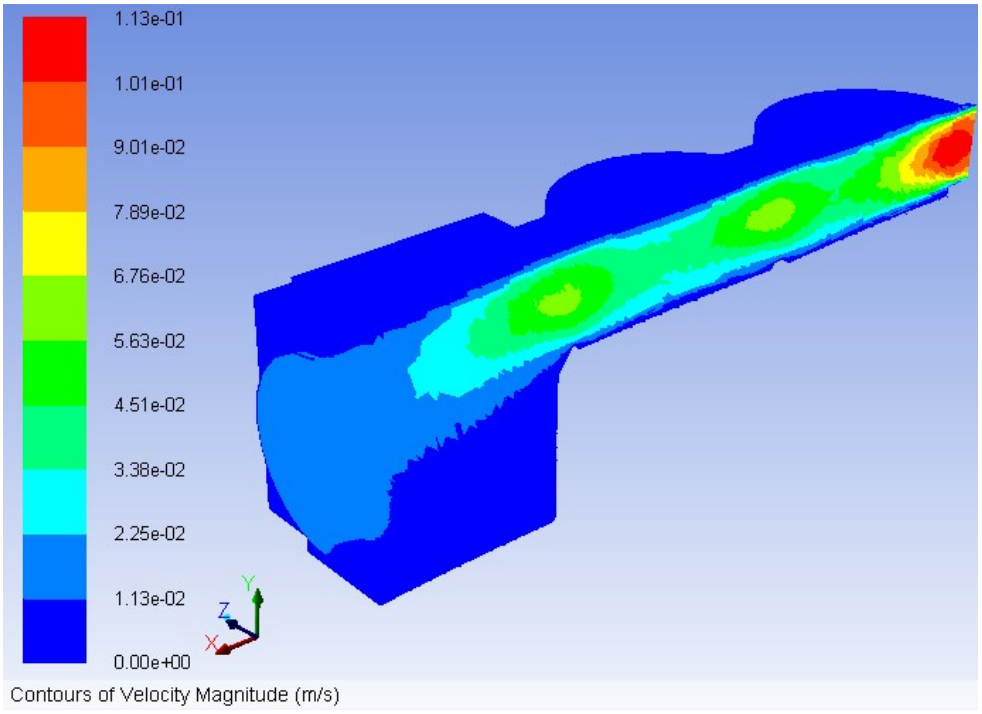

Figure 52. Flow velocity distribution in gas sampling chamber volume.

4.4. Node Software Architecture

The firmware for the microcontroller was created in MPLAB design environment, using C language and native C30 compiler for 16-bit PIC MCUs. This chapter will describe the algorithm functioning and code implementation in details. In addition, communication protocols used in the Node device will also be briefly explained.

The Node software was written with a hierarchical structure. At the top level, a main routine executes right after MCU configuration is completed. This routine contains an infinite loop, in which low-level tasks (i.e. subroutines) are sequentially called. Due to the relative simplicity of the algorithm, the decision was made not to use a third-party OS that can manage and schedule task execution and preemption. With this approach, however, each low-level task must return back to the main loop within the specified maximum amount of time to allow other tasks to be called.

For this reason, low-level tasks have been split to sub-tasks each of which can also be split to even smaller tasks to control the execution time. This results in subroutines, which can be expanded, modified, and reorganized as necessary to simplify software development and modification.

In addition to sequentially executing subroutines, the software uses interrupts for operations and events that require precise timing or a quick response. Interrupt handlers were optimized to be executed quickly in order to minimize the effect on the main loop. Shared variables are widely used for data exchange between tasks, which require additional attention in programming to guarantee information consistence. Figure 53 shows the top level block diagram of the Node firmware organization that illustrates task execution sequence along with interrupt

handlers. Figure 54 briefly reflects shared variable structures and read/write operation over them executed by tasks.

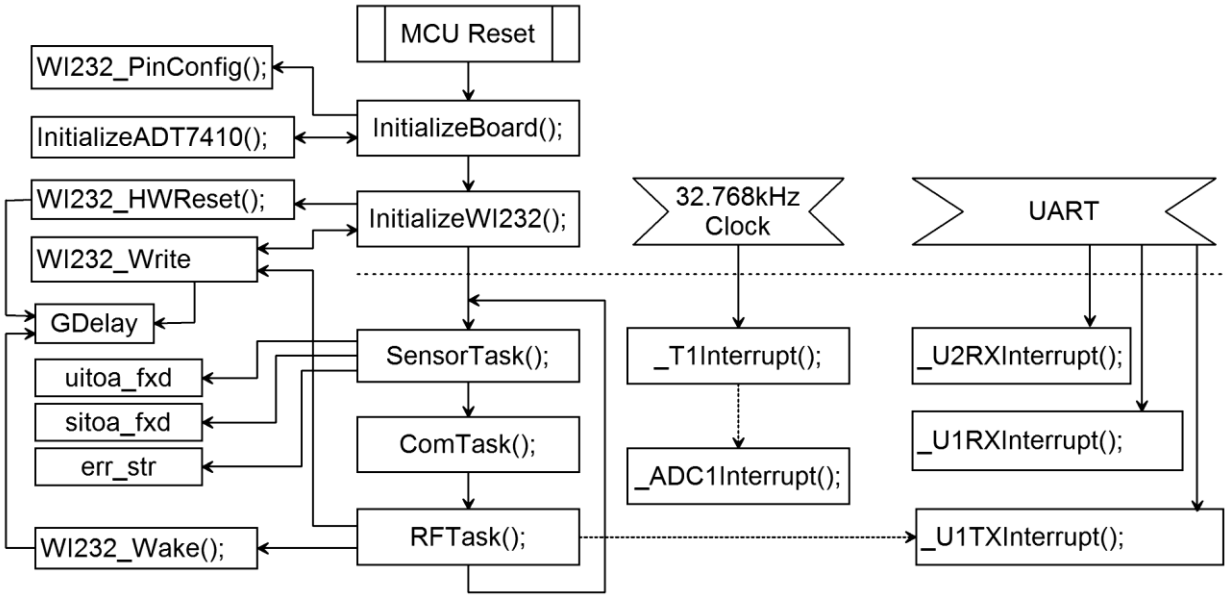

Figure 53. Top-level block diagram of the Node firmware organization.

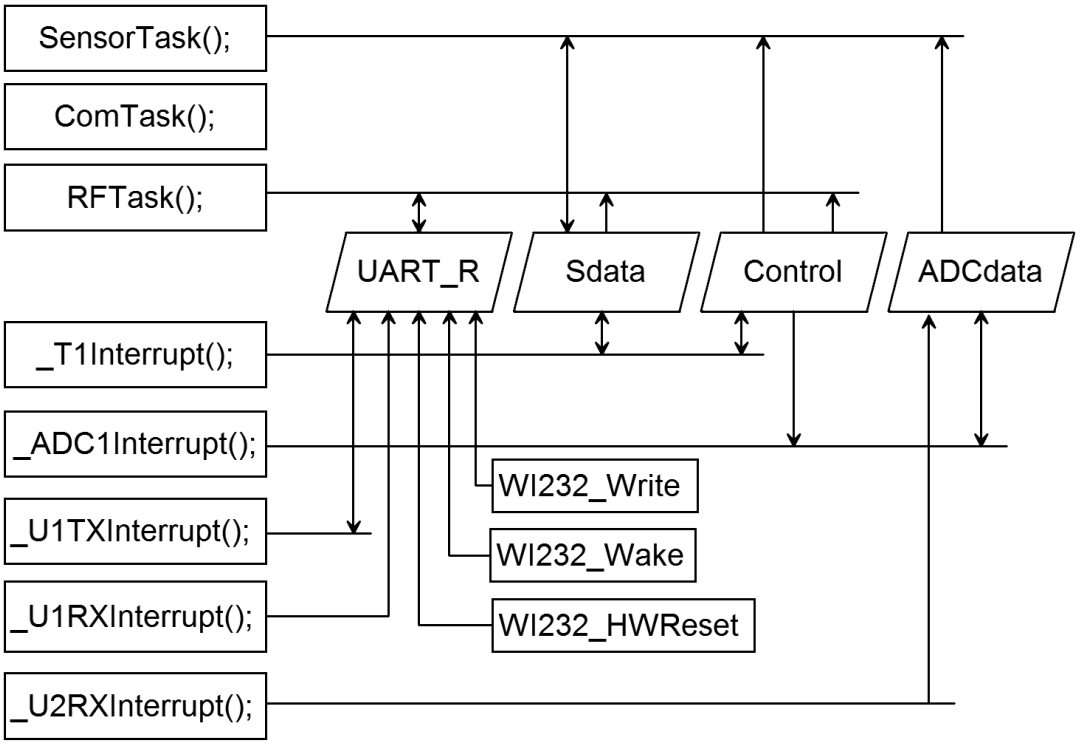

Figure 54. Major shared variables and their access by tasks and handlers.

4.4.1. Main loop

After hardware MCU reset, initialization is as follows (function InitializeBoard). First, the main instruction clock generator is configured to operate at 8MHz. A higher clock speed is possible with the MCU, but the algorithm's efficiency allows it execute at 8MHz, saving power consumption. A 32.768 kHz oscillator is also enabled and is used as a source for Timer 1 and configured to call a Timer 1 interrupt at 862.31 6Hz rate. This serves as the system's real-time clock. Timer1 also serves as the controller for the ADC module, in a sampling rate of 86Hz for all 10 analog inputs.

Second, a remap matrix is configured by connecting internal peripherals to particular pins and input/output/analog pins are set up (function WI232_PinConfig separately configures RF module control pins). Nested interrupts are enabled which allows interrupts with higher priority to suspend lower-priority interrupt routine execution, and after its completion return back to suspended one.

Third, the I2C bus is used to communicate with body temperature sensor and is configured. The presence of the ADT7410 is checked for, and if so, it is initialized to operate with 16 bit temperature resolution and a 1Hz SPS conversion rate by sending specific commands over the bus. This is also done for UART channel 1 (RF module) and 2 (NONIN pulse rate and blood oxygenation sensor module). Both channels use FIFO buffers and interrupts to efficiently process received and sent messages.

Fourth, the RF module is configured to operate on 0 hop channel, 250mW output signal power, 9.6kbps baud rate and MAC addressable network mode with acknowledgement. After configuration, the module is put in sleep mode. Function WI232_HWReset executes hardware reset of RF module, WI232_Write writes byte of command/configuration data to a specific RF

module register and function GDelay creates delay in ms that is utilized by many functions in the system.

Once initialization is complete, the program goes into an infinite loop executing 3 different tasks concurrently in addition to ISRs.

4.4.2. Timer 1 ISR

Timer 1 ISR (_T1Interrupt) has a number of functions.

- It maintains the NDIR sensor lamp ON/OFF time period at 0.4s.
- Every 4s, it initiates calculations to process of all the data that will be sent to the Base over RF by clearing appropriate flags.
- Every 5s (by default), it initiates data transmission,
- Stops sampling and starts the ADC conversion at particular rate.
- The ISR also reads and updates sensor data and control fields through shared structures Sdata and Control (refer to Figure 54).

4.4.3. ADC ISR

ADC ISR (_ADC1Interrupt) reads and filters digitized analog sensor values and update the ADCdata structure. It also determines the amplitude of NDIR sensor readings necessary for CO_2 calculation by looking for peak values within particular number of samples taken after switching the lamp on and off. In order to reduce the noise, all measurements are recorded when NDIR lamp is off and transition from “on” state is completed (which leads to smaller supply current and consequently lower switching regulator noise).

4.4.4. UART TX ISR

UART TX channel 1 ISR (_U1TXInterrupt) is responsible for initiation and transmitting data to the RF module. First, data is put to the predefined RAM buffer. Next, the ISR is called.

After that, transmission is done automatically until the last byte is sent. Within the ISR, the data is moved to the hardware FIFO buffer, and then control is returned to the main routine.

When the FIFO buffer is empty, the ISR is automatically called again to load more data. The UART RX channel 1 ISR (_U1RXInterrupt) is called when the RX FIFO buffer is full and data needs to be processed. This Routine will put all the new data to the predefined RAM buffer and update a pointer so the main routine may check it, process the data, and clear the pointer. These methods allow sending and receiving long messages to and from the bus with minimum processor time overhead.

4.4.5. UART RX ISR

UART RX channel 2 ISR (_U2RXInterrupt) tracks the first byte in a message using a state machine. Each Nonin sensor sends a 3-byte message every second. This data contains information about pulse rate, hemoglobin oxygenation, and sensor status (error flags and signal quality). When a byte is received, the ISR first checks if this is the first byte of message (by checking its MSB). If it is, the byte is temporally saved and the state machine advances. The second and third bytes are then received, saved, useful information is extracted from the complete message, the ADCdata structure is updated, and the state machine resets.

The SensorTask routine converts sensor digitized data to their corresponding values in engineering units. It contains a number of state machines for every data source, which split each calculation into subtasks. When a portion of a calculation is executed, the state machine advances and allows the processor to switch to other calculations. This approach assures that all tasks are executed in a timely manner.

The overall structure of the SensorTask routine is presented in Figure 55. As an example, the state machine and algorithm of CO_2 calculation is presented in Figure 56. The other

algorithms have a similar structure with the exception of body temperature ADT7410 reading and breathing rate calculation, which are presented in Figure 57 and 58 respectively.

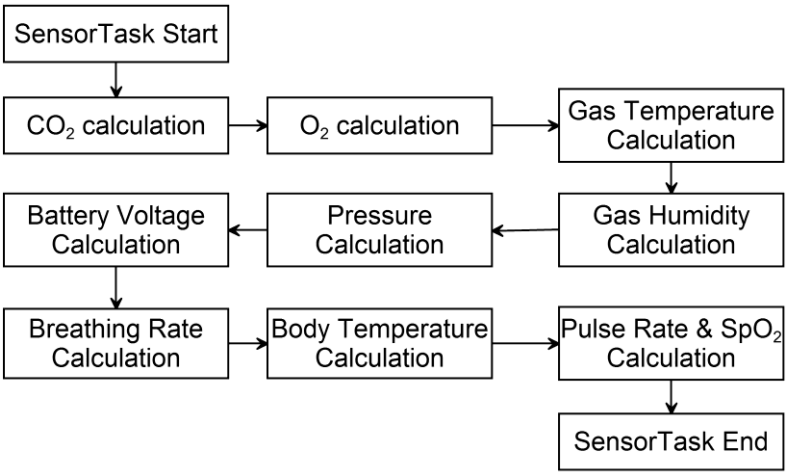

Figure 55. The top-level diagram of SensorTask routine.

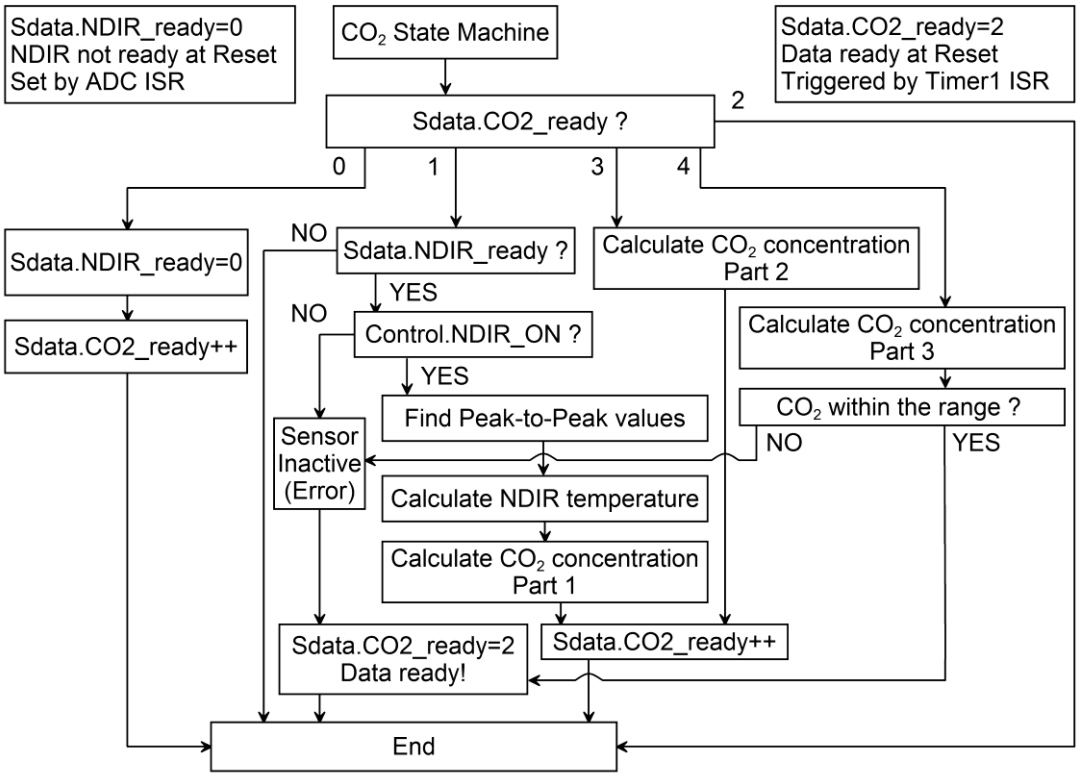

Figure 56. The diagram of CO_2 concentration calculation state machine.

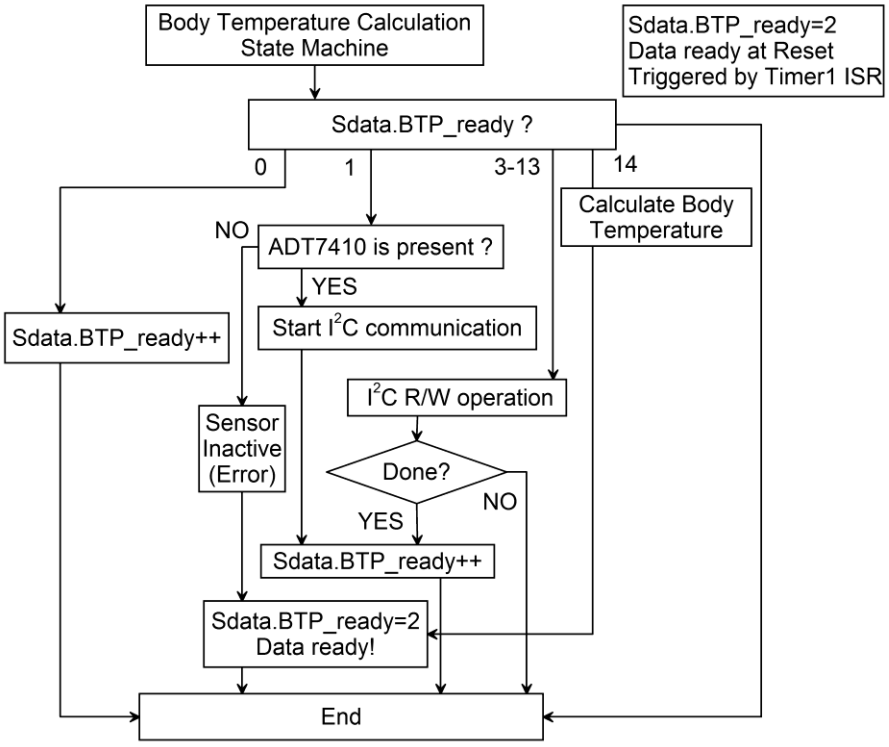

Figure 57. The diagram of Body Temperature calculation state machine.

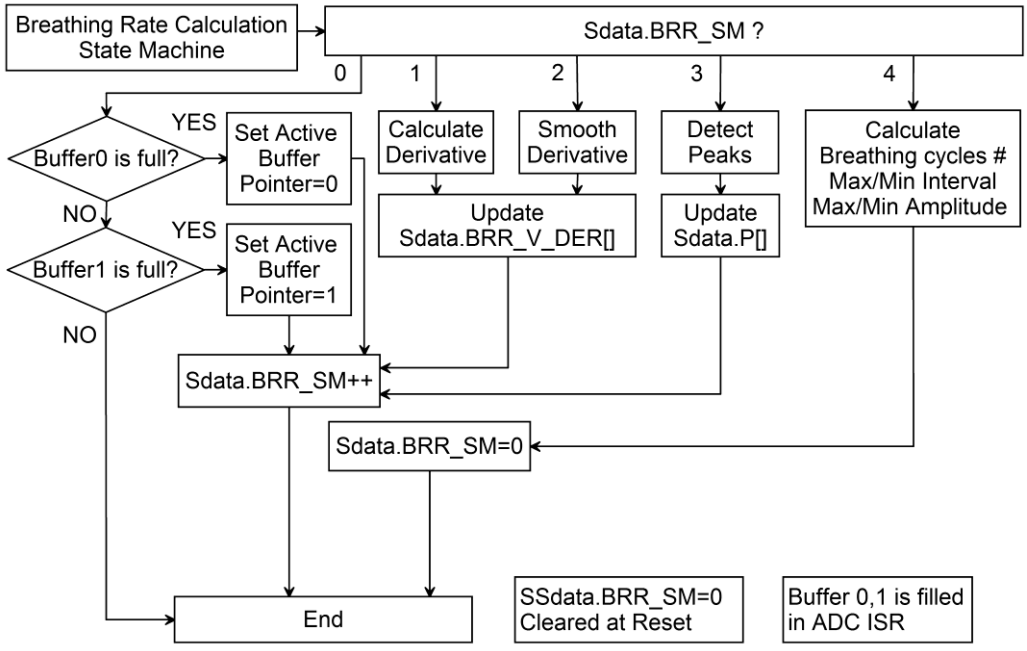

Figure 58. The diagram of Breathing Rate calculation state machine.

In the current software version, calibration coefficients are hard coded during compilation. In future versions it is planned to add automatic and user-performed calibration over the radio channel using embedded web server.

4.4.6. Body temperature calculations

During body temperature calculations, a number of bytes are sent using the I2C bus, which is a relatively slow peripheral device. Since the microcontroller doesn't have a hardware buffer to send or receive data packages using this bus, and each I2C write or read is accompanied by significant delays, wasting of CPU cycles.

In order to overcome this, the ADT7410 access sequence is divided into 12 fragments. At the beginning of each fragment, the status of previous bus command/data operations is checked. If the operation is not finished, the state machine breaks and rechecks next time. If the previous operation has finished, the state machine advances. In this way, the processor executes other routines rather than waiting.

4.4.7. Breathing rate calculation

The breathing rate calculation involves the use of two buffers that are filled alternately: when one buffer is in the process of data acquisition, the other one can be processed. The breathing rate calculation is as follows: the derivative of the breathing rate sensor data is calculated and then smoothed with the peak positions and amplitudes being saved to an array. In addition, the maximum and minimum intervals between peaks within the buffer (which has 12 second length) are calculated along with the breathing rate as presented in Figure 59. Once processed, the data is then ready to be transmitted over the radio channel.

To minimize execution time, most calculations are done using integer operations that can be executed by the processor in a single or a few instructions. However calculations require

floating point arithmetic (e.g. CO_2 concentration that needs logarithmic and root functions, final steps in body temperature and gas pressure estimation).

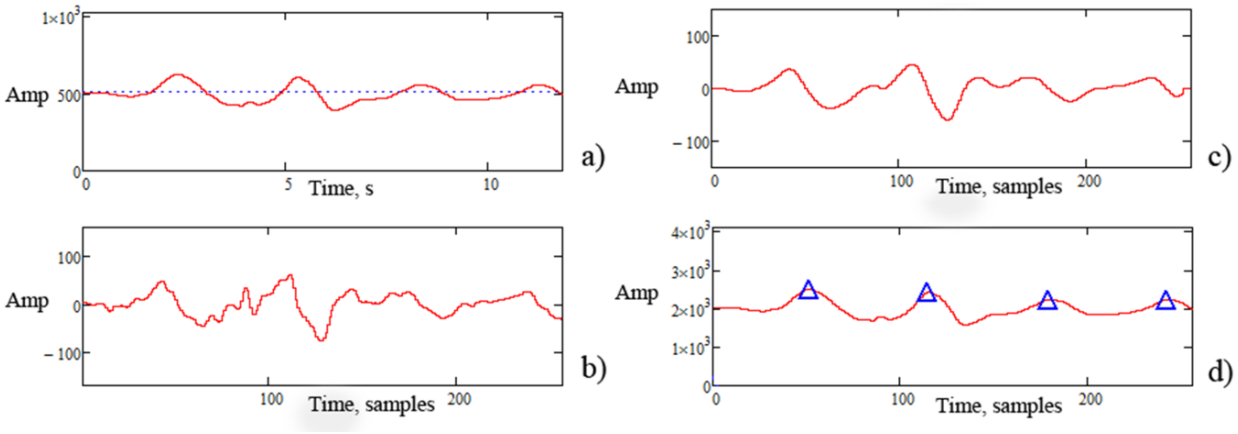

Figure 59. Acquired and processed data from respiration rate sensor: a) original signal from respiration sensor, b) derivative, c) triangular smoothing and d) peak detection.

4.4.8. Data transmission

The RFTask routine is responsible for data transmission over the radio channel. Every 5 seconds its state machine is triggered. When this happens, the most recent data is merged into a 64-byte package including control flags and sensor calibration information. When this package is created, the RF module waking up routine WI232_Wake is called to prepare the RF module to send the data. The 64-byte package is then transmitted to the module using the UART. This module is configured so that when its internal buffer received 64 bytes of data, transmission is triggered. By monitoring control pins, the program checks when the message is transmitted or when an error occurs. This module then uses an acknowledgment feature with the maximum number of retries set to 10. When transmission fails, the TX engine waits a random amount of time before retransmitting. Only after successful transmission (or if the number of retries expires) will the program reschedule the next transmission.

This simple mechanism allows the Nodes to find "empty spot" in a 5 second time frame which is safe for sending data and avoiding collisions and delays. At the end of each transmission, the module is put to deep sleep mode to reduce power consumption.

The algorithm of RFTask is presented in Figure 60. This routine uses uitoa_fxd (unsigned integer to ASCII), sitoa_fxd (signed integer to ASCII) and err_str (error string generation) functions that in addition to their main purpose allow one to set the number of digits and decimal point position in the generated string. Figure 61 shows the transmission package structure: SOH is Start Of Heading, Node # represents unique node number (system currently supports 10 Nodes, but this can be simply extended), STX is Start Of Text, BAT is Battery voltage in Volts, GPR is Gas Pressure in kPa, GHM is Gas Humidity in %, GTP is Gas Temperature in °C, O2 is O_2 concentration in %, CO2 is CO_2 concentration in %, PUR is Pulse Rate in bpm, BTP is Body Temperature in °C, OXY is SpO_2 in %, PeakCnt is number of breathing cycles per 12 seconds, IntMin and IntMax are intervals between breathing cycles in seconds, AmpMin and AmpMax are relative chest displacement levels. The third row in Figure 61 shows data that is sent for calibration purposes: CO2_REFpp_RAW is peak-to-peak value of NDIR sensor reference channel, CO2_DETpp_RAW is peak-to-peak value of NDIR sensor detector channel, CO2_TMP_RAW is NDIR thermistor temperature, O2_RAW represents oxygen sensor reading. Finally, ETX is End of Text, Reserved is unused space in package for further features and EOT is End of Transmission.

To keep the system versatile, all characters are transmitted using ASCII codes including control flags. While not efficient, ASCII allows packages to be read by any device. However, there are no delimiters, so the receiver must know the number of characters per parameter to

correctly separate the data stream. This information is not shown since the Nodes were designed to only operate with the Base station.

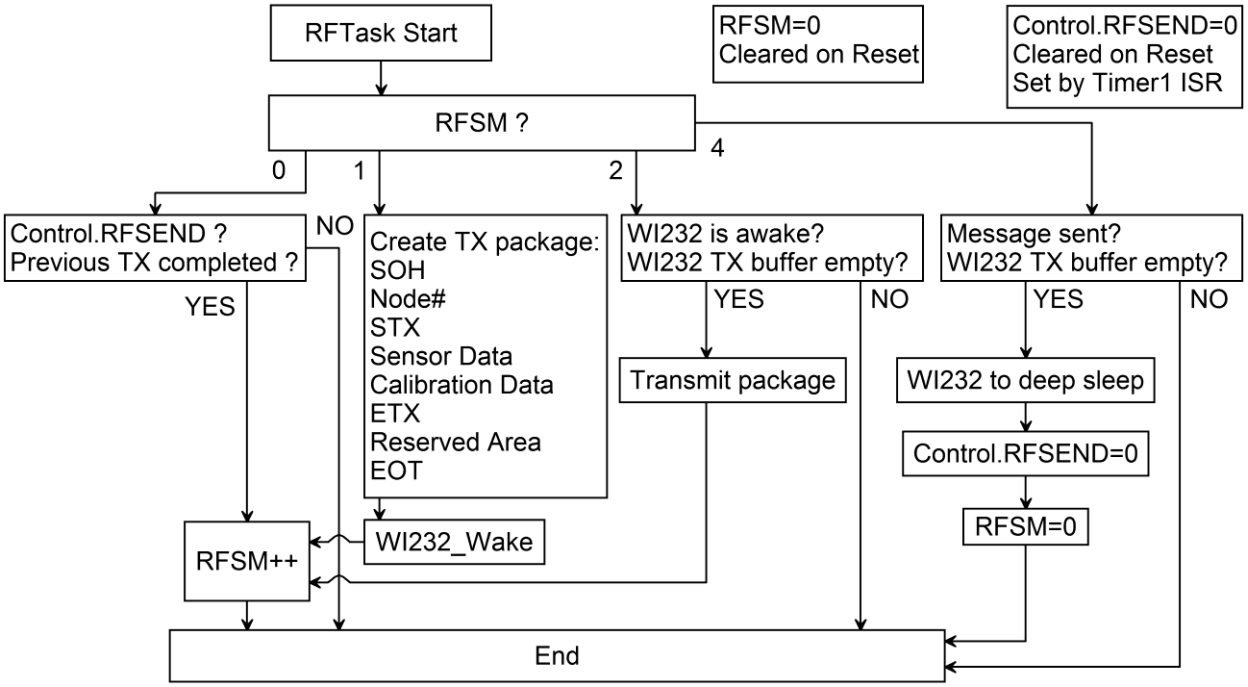

Figure 60. The top-level diagram of RFTask routine.

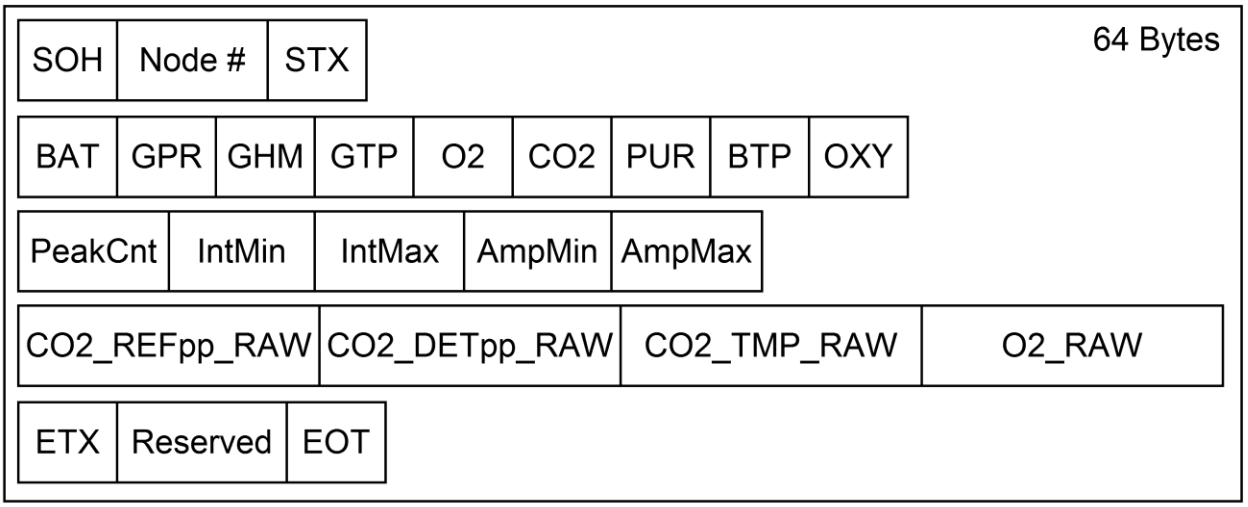

Figure 61. The transmission packet structure.

It was determined that one package requires approximately 0.3 s of transmission time. With a five second update time, up to 16 Nodes can operate with each Base. This could be increased, however, by increasing the baud rate, using additional base stations/hop channels, or by using other wireless network topologies.

Finally, the ComTask routine was created for the debugging and data validation purposes. In previous Node prototype (rev. C) it utilized UART channel to send the information to the terminal. It is not used in final Node prototype (rev. D).

4.5. Summary

In this chapter, the hardware and software for the Nodes was described. In the following chapters, the hardware and software for the Base is presented.

CHAPTER 5. BASE HARDWARE AND FIRMWARE DESIGN

5.1. Introduction

In this chapter, the hardware and software design for the base is presented. The Base station performs data collection through the radio channel from all Nodes in the network, it verifies this data, and stores it in local non-volatile memory. Information can then be retrieved using a web-enabled device. To provide standalone operation and independent from operation system settings, the Base also contains a real-time clock that makes it possible to add a time-stamp to every stored package and to restore a complete image of data when required. Figure 62 shows the block diagram of the Base station.

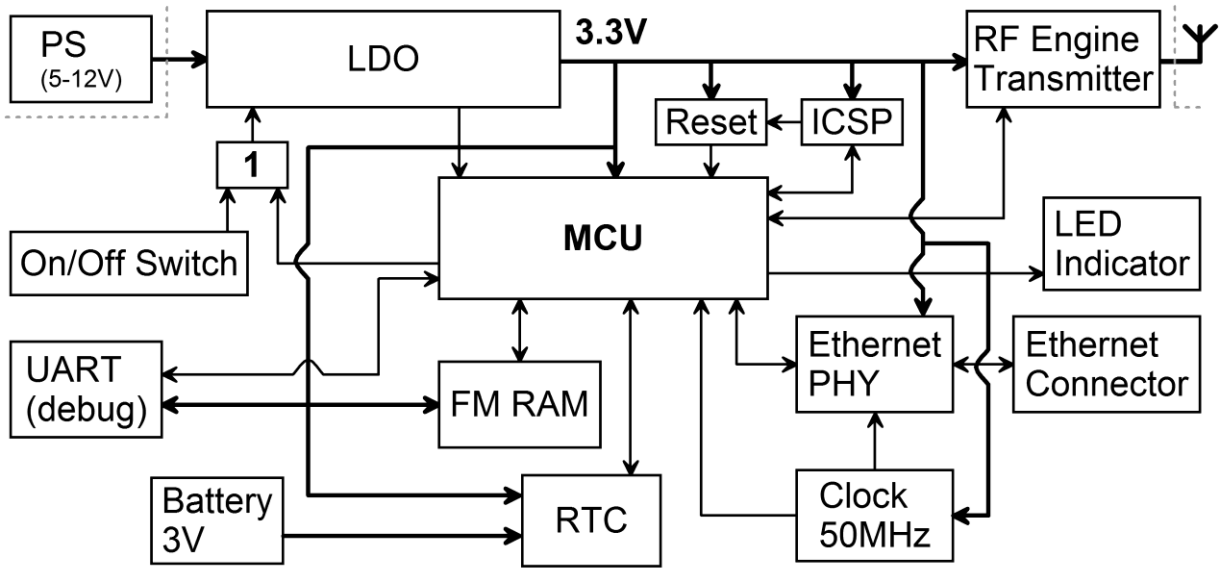

Figure 62. Block diagram of the Base unit circuit.

5.2. Base Hardware Design

The Base requires a power source between 5 V and +12 V at 0.4 A. This voltage is converted to 3.3V using a linear regulator. The complete power supply schematic is shown on Figure 63. Chip U8 LT1763-3.3 (Linear Technology) is low-noise micro-power 3.3 V @ 0.5 A regulator with shutdown, voltage sense and reverse battery protection features.

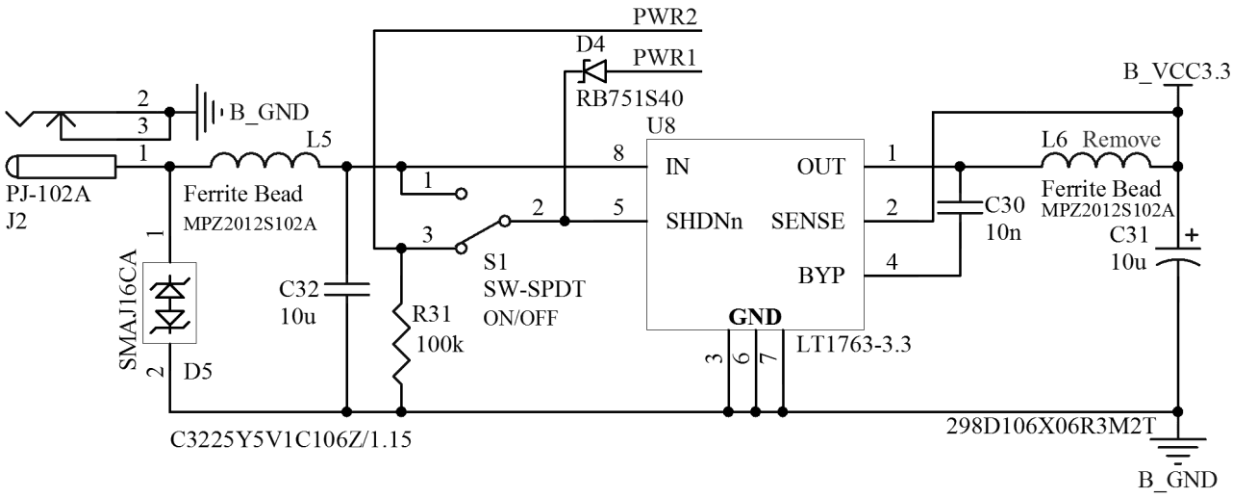

Figure 63. Power supply schematic of the Base unit.

The real-time clock circuit is built around U4 DS1374C (Maxim IC) chip as presented in Figure 64. It contains a 32-Bit binary counter that increments every second using an internal oscillator circuit. The value in counter and operation modes can be accessed and modified using I2C bus (pins SDA and SCL). An external 3V lithium battery BT1 provides supply for the chip when the main power is off. This allows the system to track the time independently and retract the timestamp when required (e.g. when data package from the Node has been received or when sensor calibration has been performed). Additional pins INT (alarm interrupt output) and SQW (square-wave output) are connected to the MCU for future modifications, but currently are not used. Input pin RST allows resetting the circuit.

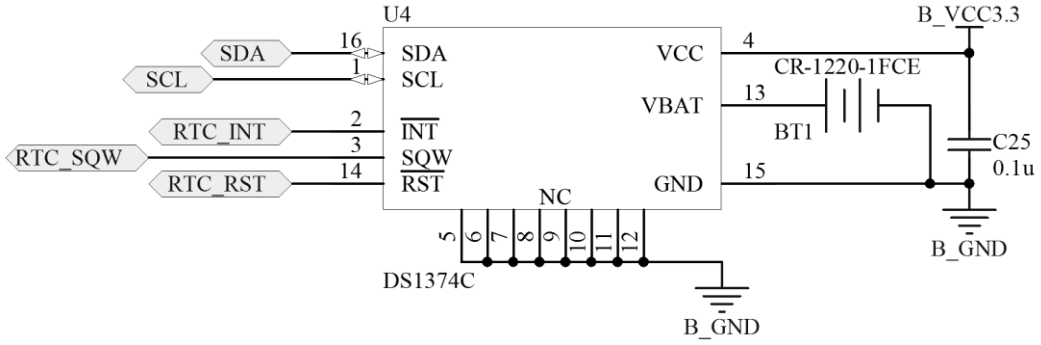

Figure 64. Real-time clock schematic of the Base unit.

For non-volatile data storage, a 1M bit low-power consumption ferroelectric memory chip U2 FM25V10 (Ramtron) was selected with its connection presented in Figure 65. This type of memory performs fast random writes and reads using high-speed SPI bus (pins DO, DIN, SCL and CS). The chip provides a reliable data retention of approximately 10 years and eliminates many problems associated with flash memory (e.g. block writes). Memory is organized as 8x128K and is sufficient to store last 6 hours of data from 1 Node with a 5 second update rate including time stamp. The write protection pin WP is not used and is pulled-up to VCC. The HOLD line is used when the CPU must interrupt a memory operation for another task (e.g. interrupt processing). During its low state any transitions on bus pins are ignored. The maximum serial bus clock speed is 40MHz. However due to MCU and system clock limitations, the chip operates on 25MHz in current Base version.

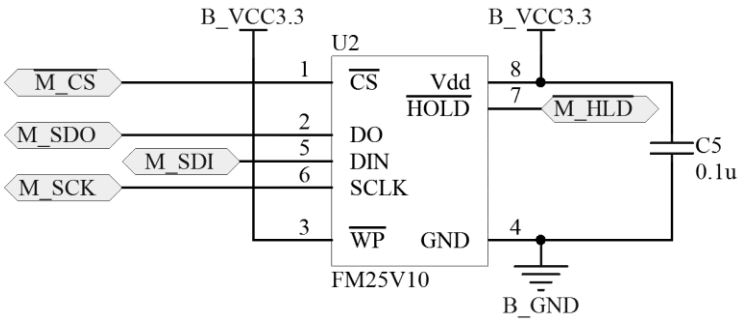

Figure 65. Non-volatile memory chip connection of the Base unit.

The microcontroller reset circuit is presented in Figure 66 (left). U9 MAX6394 (Maxim IC) is a high-accuracy open-drain supervisor in a small SOT143 package that generates 100 ms active-low pulse during power-on or when the system voltage drops below 3 V. The value of pull-up resistor R35 is based upon MCU datasheet recommendations. In-circuit serial programming and debug connector P1 (Figure 66, center) is used for firmware flashing and debug operations. Line PGC is the clock, PGD is serial data, and MCLR is connected to the

MCU reset input creating a wired OR with the supervisor circuit. Connector P2 (Figure 66, right) is used for firmware debug using the UART interface. It also provides system power to connected board with L4 reducing its noise.

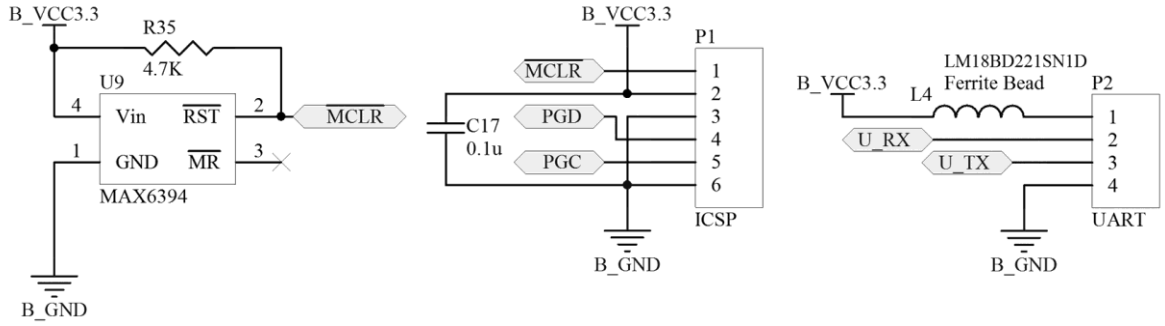

Figure 66. Schematic of the MCU reset circuit (left), ICSP debugger (center) and UART interface (right) connectors.

The radio transmitter module WI232FHSS (Radiotronix) connection circuit is the same as the one used in the Nodes and is presented in Figure 67 (left). For indication of switching on state, Ethernet and RF activity, four LEDs are used as presented in Figure 67 (right).

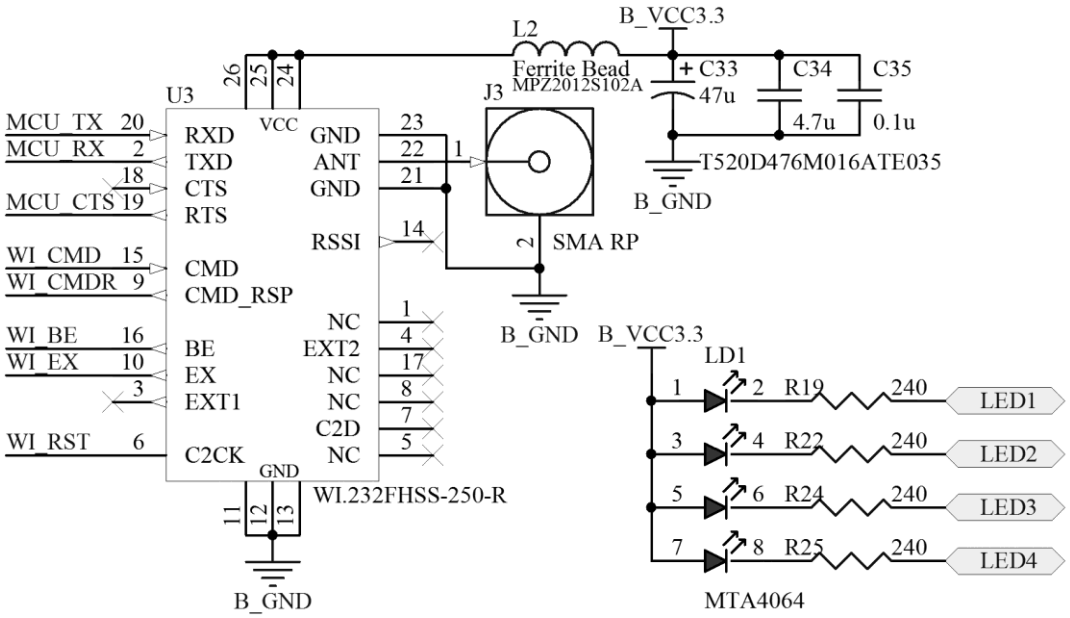

Figure 67. WI232FHSS-250-R module connection circuit (left) and indication LED bar (right).

The hart of the Base unit is a 32-Bit microcontroller U5 PIC32MX695F512H (Microchip). It can operate at 80 MHz providing high performance, contains 512K of flash ROM and 128K of RAM required for TCP/IP stack and embedded web server operation along with RF package processing from multiple Nodes. The MCU supports SPI, I^2C and UART interfaces, all utilized by external non-volatile memory as well as the RTC and RF module. In addition, 10/100 Mbit Ethernet MAC hardware with MII/RMII connection is also available on chip, which makes it possible to implement Ethernet connection with a minimal number of external components. Connections are presented in Figure 68. Chip U7 MAX3207 (Maxim IC) provides overvoltage protection on the UART debug interface pins that may happen when external board is connected. Pins CLK_MCU and EREF_CLK_MCU provide a clock to the MCU core and Ethernet engine respectively. I2C and some interrupt pins are pulled-up in accordance to the datasheet.

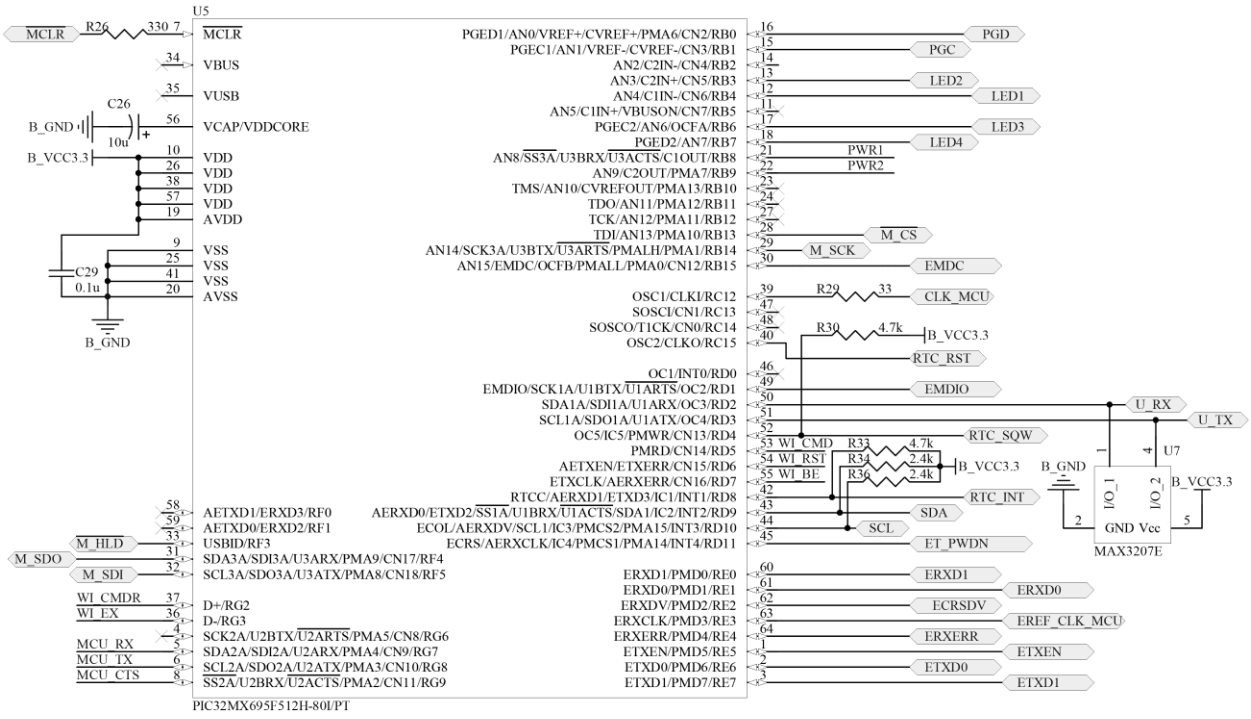

Figure 68. Microcontroller PIC32MX695F512H connection circuit.

5.3. Base Operation

In order to allow Ethernet communication between the Base and external device, the Base contains a low power consumption physical layer transceiver U1 DP83848 (National Semiconductor) that is connected to U5 PIC32 MAC layer using a reduced media independent interface RMII (refer to Figure 69). This interface reduces the number pins required. Data is transferred 2-bits at a time between layers, using 50MHz clock (EREF_CLK_PHY). C14, L3, C15 and C16 create a filter for the analog power supply line that supplies internal DAC and ADC. Differential pairs MDI_T_P/N and MDI_R_P/N are connected to transformer and RJ-45 jack (Figure 70), to which twisted pair media is then can be attached. Additionally, LED_LINK (status of link), LED_SPEED (10 or 100 Mbit) and LED_ACT (link activity) pins are used for indication. Connector J1 SI-60062 (Magjack) integrates all required magnetics, LEDs and jack simplifying the design. L1, C3 and C4 filter out noise on the power supply line. B_SHL represents a connection to the chassis (connector shielding, device enclosure and PCB edge). Additional information about U1 operation and recommended connection can be found in [64]-[65].

Because the Ethernet MAC/PHY blocks require a high-stability 50MHz clock source, it was decided to use miniature high-stability (25 ppm) CMOS silicon oscillator Y1 XOSM-533 (Vishay) along with clock buffer U6 CDCLVC1103 (TI) that creates 3 clock channels (Figure 71). A buffer is required since the total 3-input load capacitance (MCU and PHY) will exceed the maximum load for Y1 (30 pF).

To reduce power consumption, it was decided to use the same 50 MHz clock as system clock for the PIC32 MCU (CLK_MCU line) instead of using additional oscillator or built-in

FRC with PLL. This speed is sufficient for TCP/IP stack operation and the Node's service routine needs.

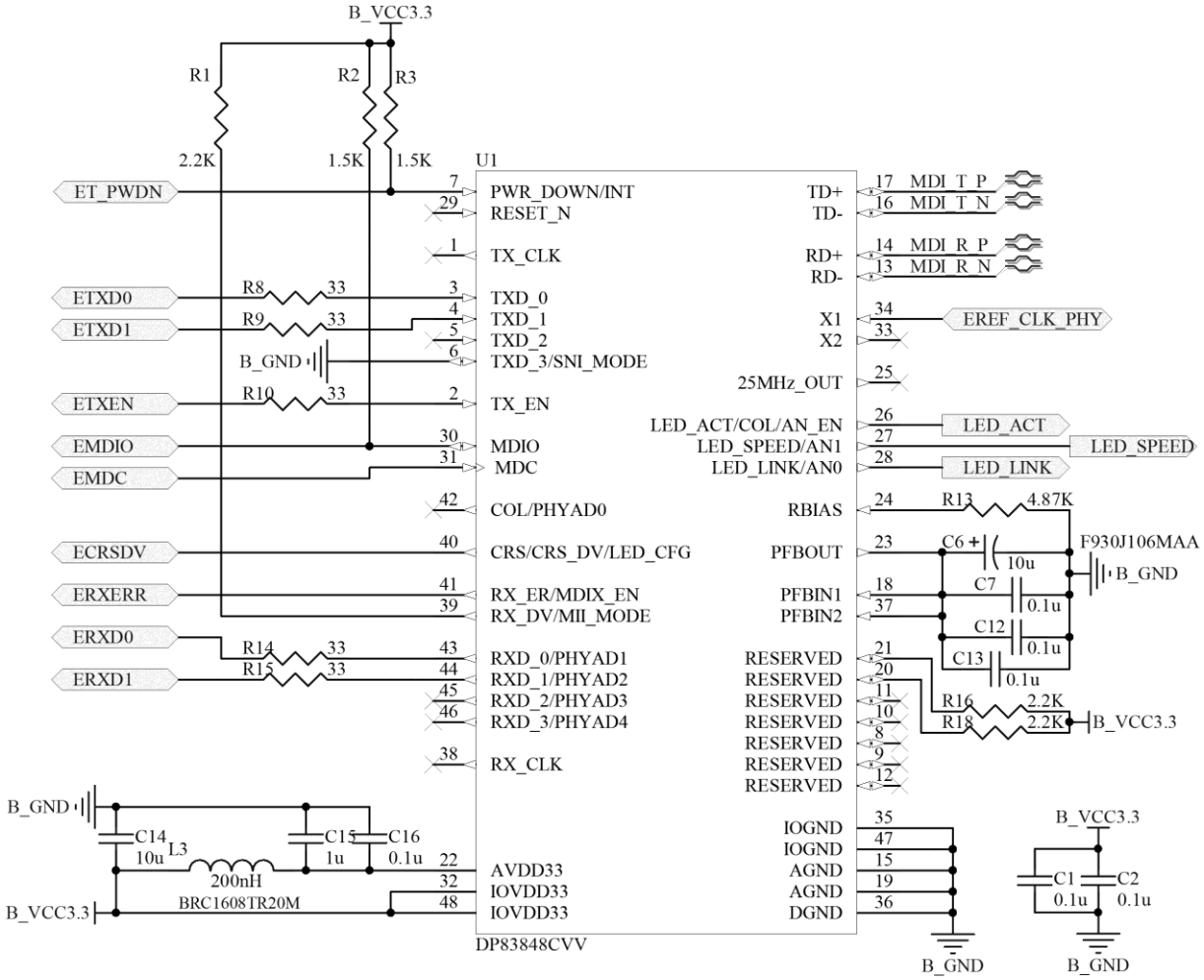

Figure 69. Ethernet PHY DP83848 connection circuit.

5.4. Base Board Layout and Component Placement

The Base station main board layout using a double-sided FR4 PCB. The same guidelines as the Node device were used with the exception of using ground plane separation due to the absence of analog blocks. Special attention was made to the differential pair routing and shielding between Ethernet magnetics and PHY chip. Figure 72 shows the coarse component placement on the top of Base PCB.

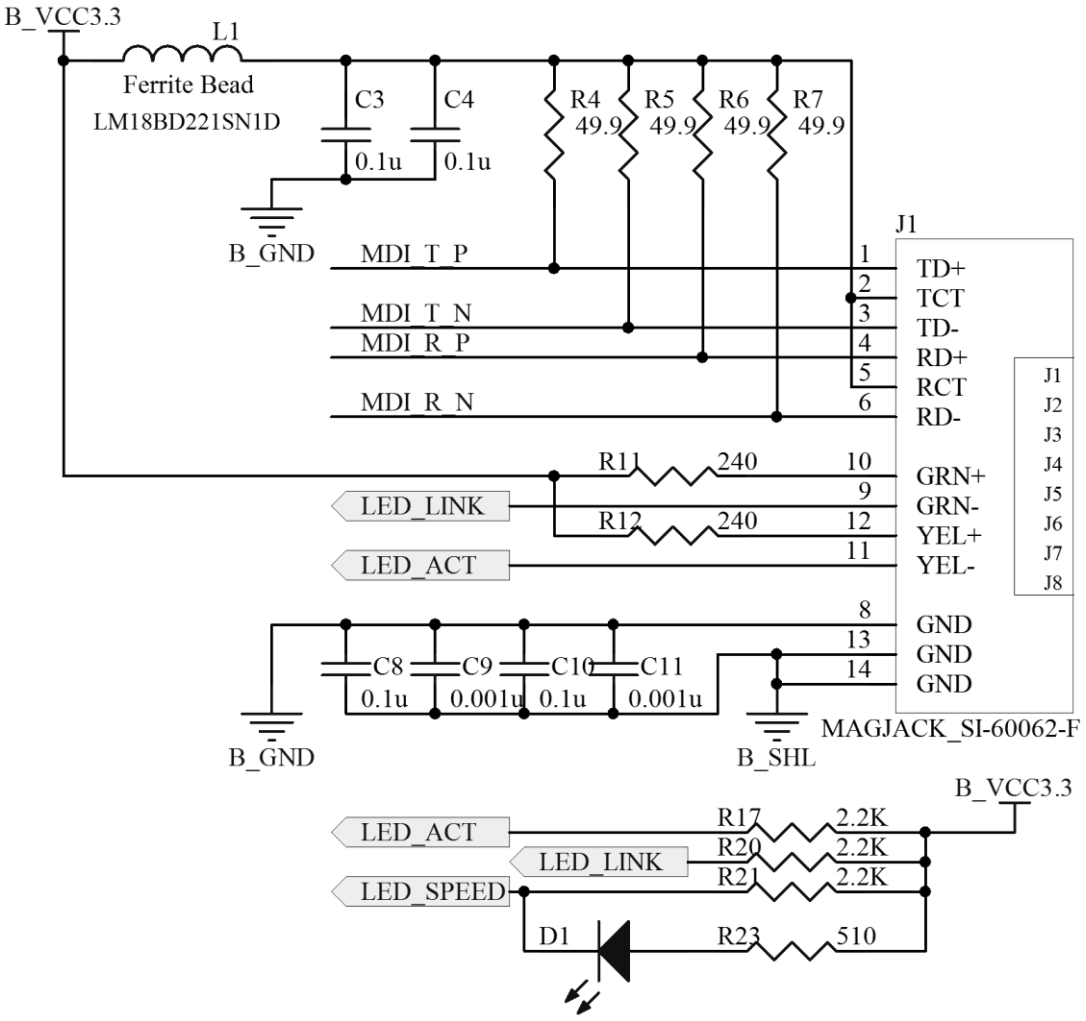

Figure 70. Ethernet magnetics and RJ-45 connector circuit.

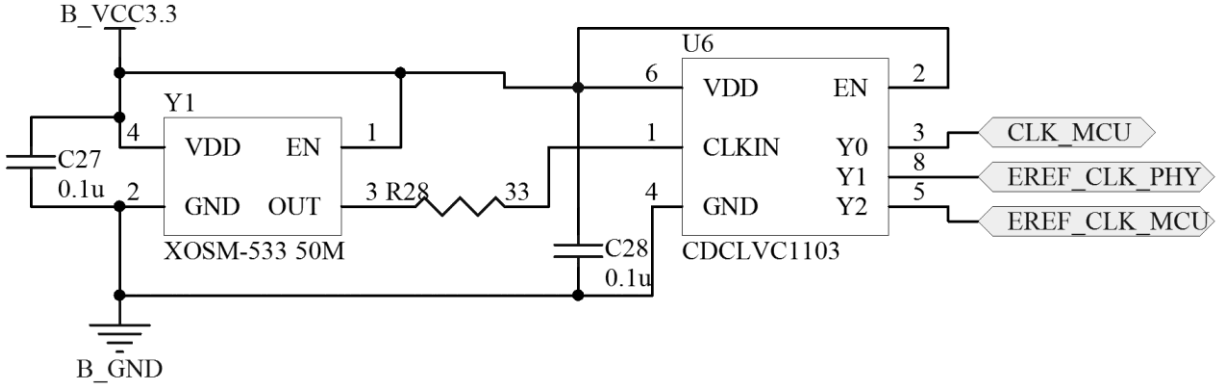

Figure 71. System and MAC/PHY clock generator schematic.

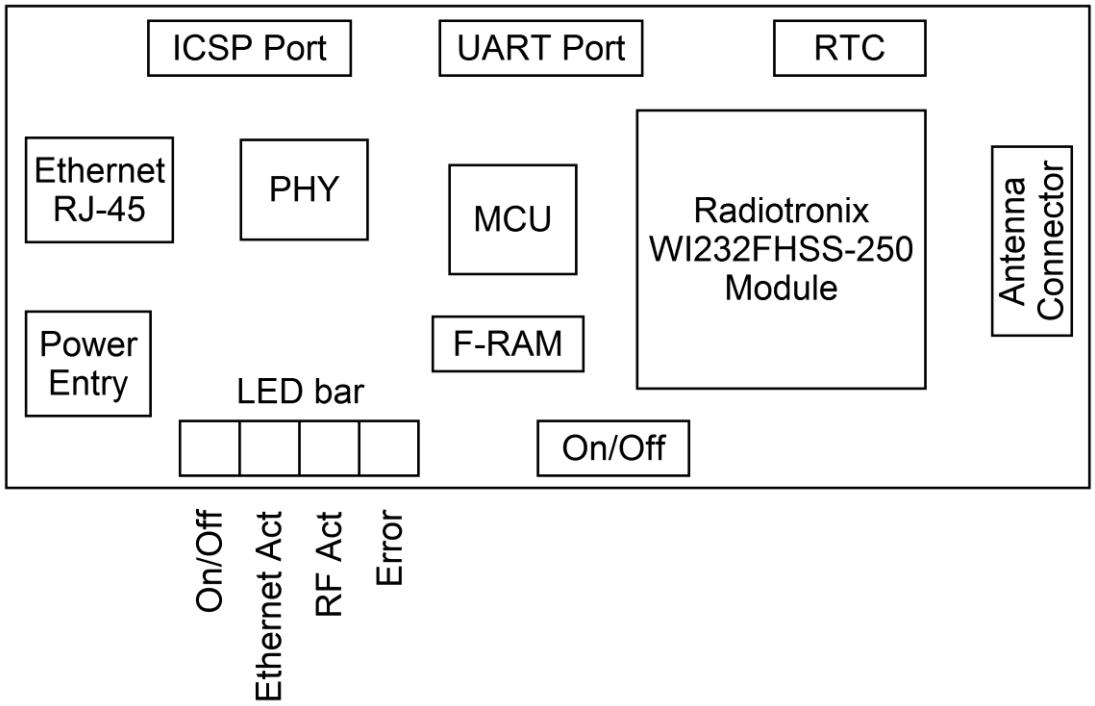

Figure 72. The placement of switch, connectors, indication LEDs and major parts on the top layer of the Base PCB.

A standard 2.1 mm ID jack is used for power entry connection. Toggle On/Off vertical switch and 4 LEDs control and indicate the unit operation. There is no opening in the enclosure for ICSP and UART ports because they are only used during programming and debugging. Antenna connector SMA-RP is located on the opposite side. Because the same RF module was used like as in Node, calculation for the transmission line between the module and antenna is the same (refer to Figure 45 and Table 2).

Top and bottom PCB layouts are shown on Figures 73 and 74 respectively. Digital ground is separated from chassis ground (mounting screws, enclosure, Ethernet shielding) by a 100 Ω resistor and 0.01/0.1 uF capacitors. This creates low-impedance path for high-frequency components and high-impedance path for DC, which improves shielding. This makes sense only if a metal enclosure is used, which is not the case for the current prototype, however, where a

plastic enclosure was used. The assembled Base PCB with the power supply, Ethernet cable and debugger is shown on Figure 75. For the test purposes, the antenna was replaced by piece of wire.

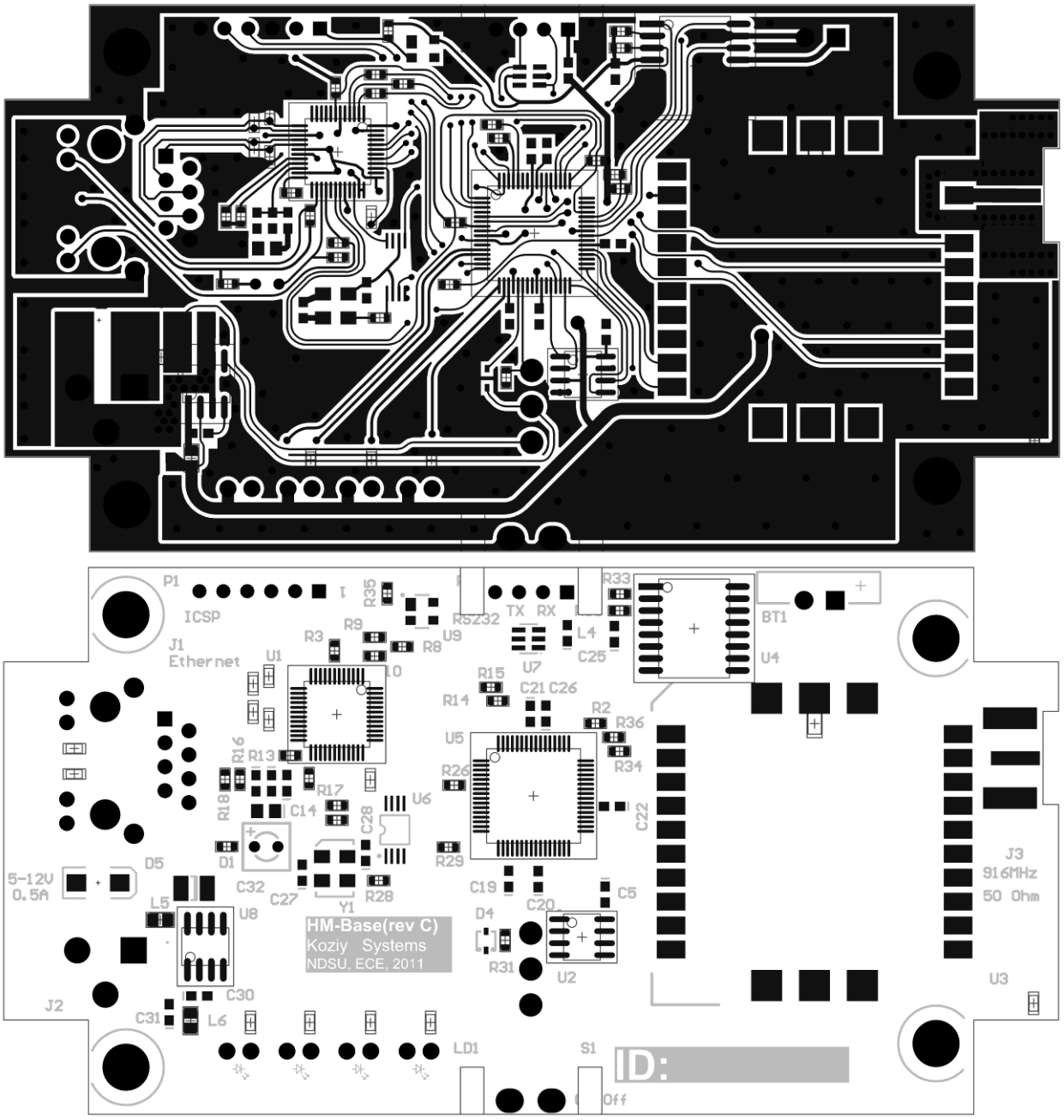

Figure 73. The Base PCB layout (copper and silk screen with pads, top layer).

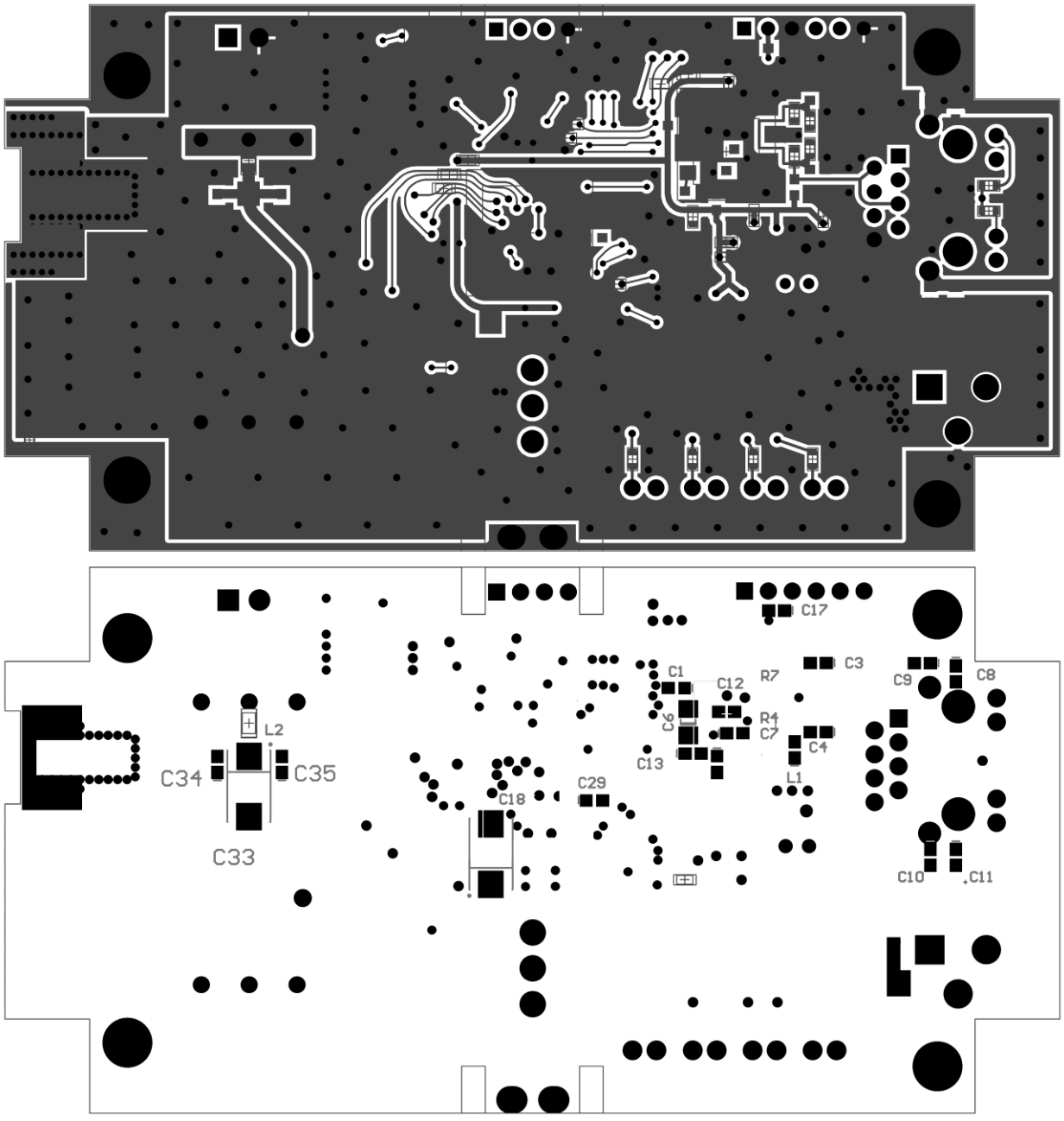

Figure 74. The Base PCB layout (copper and silk screen with pads, bottom layer).

Figure 76 represents the Base station with enclosure. There was no need in custom enclosure design, so standard enclosure p/n A9020265 was ordered from OKW.

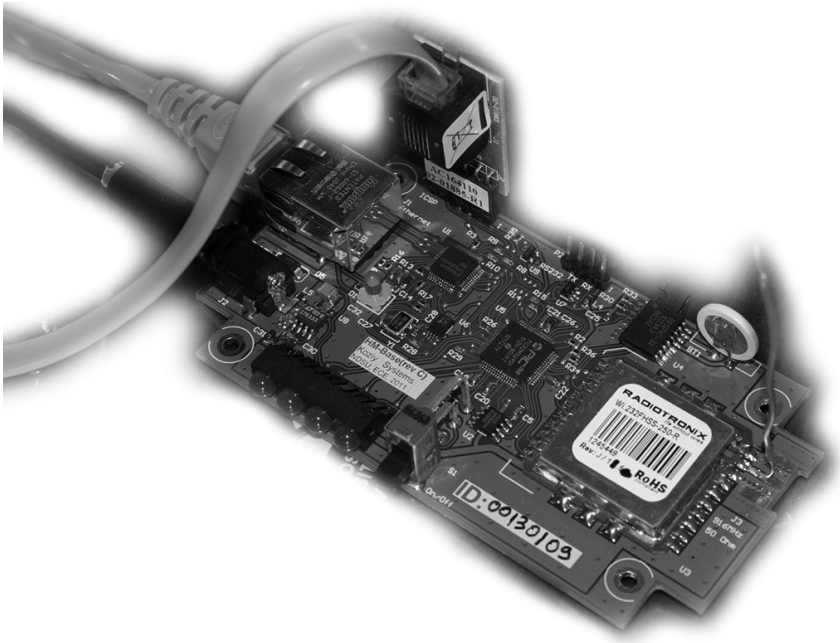

Figure 75. Completely assembled main board of the Base device (w/o antenna).

Figure 76. Completely assembled Base device (without power supply, Ethernet connections and attached antenna).

5.5. Base Station Firmware

The Base station firmware (FW) is responsible for collecting data packages from remote Nodes over the RF channel, validating and storing it in a local buffer and non-volatile memory for further use. This firmware also utilizes an embedded web server for the user interface. In the current prototype revision, remote Node control, RTC, and data logging to non-volatile memory are not implemented. Data logging is done through web interface using the local computer's storage with the time stamp coming from operation system time.

The software design for the Base is divided on two tasks – MCU firmware design and web interface. First one includes board peripherals and interrupt initialization, TCP/IP stack and embedded HTTP server configuration and integration into the main task sequence and radio channel service routines. The second part is completely related to web design, which includes a graphical user interface using HTML and JS languages, bridge to Node data, dynamic variable updates, and user request processing using AJAX and AS3. The top-level firmware block diagram is shown on Figure 77.

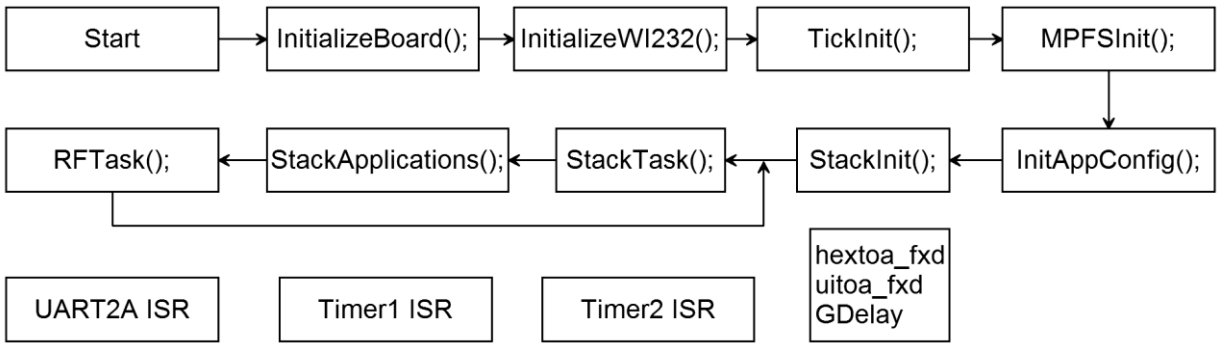

Figure 77. Top-level block diagram of the Base firmware.

The InitializeBoard routine is responsible for MCU I/O pin direction configuration, SPI bus settings to operate with F-RAM, WI232FHSS RF module pins and UART (channel 2A, interrupt on data receiving) settings, I^2C bus configuration to operate with RTC chip,

initialization of global variables, Timer2 operation and enabling of multi-vector interrupts (in this mode each interrupt has its own vector address). In addition to this, MCU system clock source is set and configuration bits required for proper operation are initialized.

The InitializeWI232 routine is used for RF module configuration, which includes module hardware reset and register settings to work in the same regime similar to the Node RF module. In the current FW version, the module only receives packages from the air and send back acknowledge.

The TickInit routine configures Timer1 and related interrupts. This timer is used by Microchip TCP/IP stack, which is open source software designed for Microchip microcontrollers. The stack itself is a set of program modules that provide services to standard TCP/IP-based applications like HTTP Server, Mail Client etc. It significantly simplifies the design of firmware because there is no need to know its operation in details unless special adjustments and functionality are required. From a programmer's point of view, it is necessary only to know how to configure the stack (which services to enable, set MCU and PHY type, device IP). Further information about stack operation can be found in [66].

The MPFSInit routine initializes Microchip File System (located on flash ROM area in MCU, or on external ROM) that contains files used by HTTP Server. These files are created during the WEB design stage and can represent HTML pages, JS and AJAX code, XML data, images etc. Files are initially put in a specific folder on the PC, and later are compressed by a special utility to create a single file image (MPFSImg2.c). This image is then attached to the whole project in MPLAB and after compilation is flashed to program memory along with the rest of the code. It is also possible to put this image file separately on external memory. However

this technique is only required when MCU with limited flash ROM is used, which is not the case for current design.

The InitAppConfig and StackInit routines initialize TCP/IP stack variables, core layers (MAC, ARP, UDP etc.) and application modules (HTTP, ICMP).

The StackTask routine performs normal stack tasks including checking for incoming packet, type of packet, and calling the appropriate stack entity to process it. The StackApplications routine invokes each of the core stack application tasks.

One important file is CustomHTTPApp.c. This contains a number of functions, each of which is executed when a special symbol sequence (any text, enclosed by "~") is detected by HTTP parser engine in file on MPFS. For example, if WEB page file index.html contains ~Variable~ sequence, then instead of printing "~Variable~" on client side, parser will call function from CustomHTTPApp.c file with name HTTPPrint_Variable. This function can simply output text or the current variable value to a web browser or execute required instructions on the MCU. It is also possible to pass parameters to these functions. This mechanism allows creating a bridge between data in code and data displayed in the WEB browser. This file also contains functions that process GET and POST requests from the client side, which are important for executing particular instructions (e.g. changing RAM variable values) by user request from WEB page. More details about HTTP Server operation can be found in [67].

The UART2A ISR is called when the FIFO receiving buffer of UART block is full. The ISR then moves all data from the RX FIFO buffer to a RAM buffer and increase the receive counter. This indicates to the main routine that there is data to be processed. The ISR is also used for data transmitting. For that purpose, data is first put to the RAM buffer and then the ISR is manually called. After this, a data chunk will be put to transmitter FIFO and automatically

transmitted. The ISR will be called again when all data from TX FIFO is transmitted and buffer is ready to accept new data. This sequence will be repeated until transmit counter is zero.

The Timer1 ISR is used by the RFTask routine to keep track of time and make required delays (by GDelay function). Timer2 ISR is used by TCP/IP stack for the same purpose. Support functions hextoa_fxd and uitoa_fxd that are used for conversion to ASCII, have the same purpose like in Node firmware.

The RFTask routine is based on a state machine as presented in Figure 78. Every time the RF module receives a valid message, this message is transmitted by an ISR to the UART2A RAM buffer (which is limited to 256 bytes) and the buffer pointer is updated. First, this routine checks for new data. If present, it looks for a SOT symbol indicating the start of package. When it is found, it locates the EOT symbol within the range. This mechanism allows recognizing incoming data packages of different sizes, which simplifies the process of adding new features. If an EOT has been detected, the RFTask routine puts the RF module into command mode to read the RSSI value. This value helps to determine the link quality between the Node and the Base. Next, the Node number information is extracted and the rest of the data is saved to a particular row in the Nodes Data Array (refer to Figure 77). This data is then used by CustomHTTPApp.c and StackApplications routines to display appropriate values on the web browser screen.

Current FW version supports 5 rows and the user can attach any Node number to any of these rows through the web interface as explained below. The number of rows limits the number of Nodes which can be displayed on the web page at the same time. It is only limited by available RAM, and with current MCU can be extended. Finally, the state machine resets and waits for a new message.

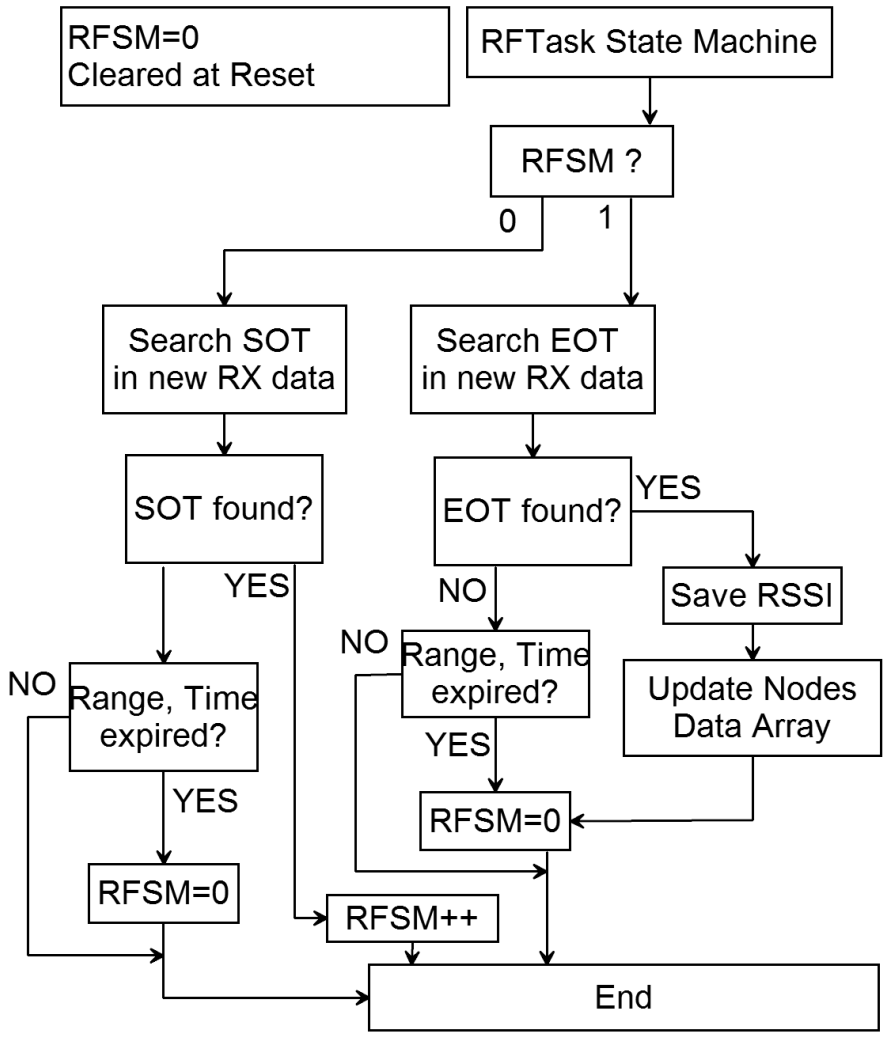

Figure 78. State machine of RFTask routine of the Base.

The RFTaskSystem also tracks the time since the last successfully received package for each active Node. This time is available for the user through the web interface, which with the signal strength indicator, allows one to monitor possible link problems.

The web graphics development and control engine were created and debugged with the help of Adobe Dreamweaver, using HTML, JS, Ajax and AS3 programming languages. Figure 79 shows a brief functional diagram of the whole web page engine along with its interaction with the main routine and data.

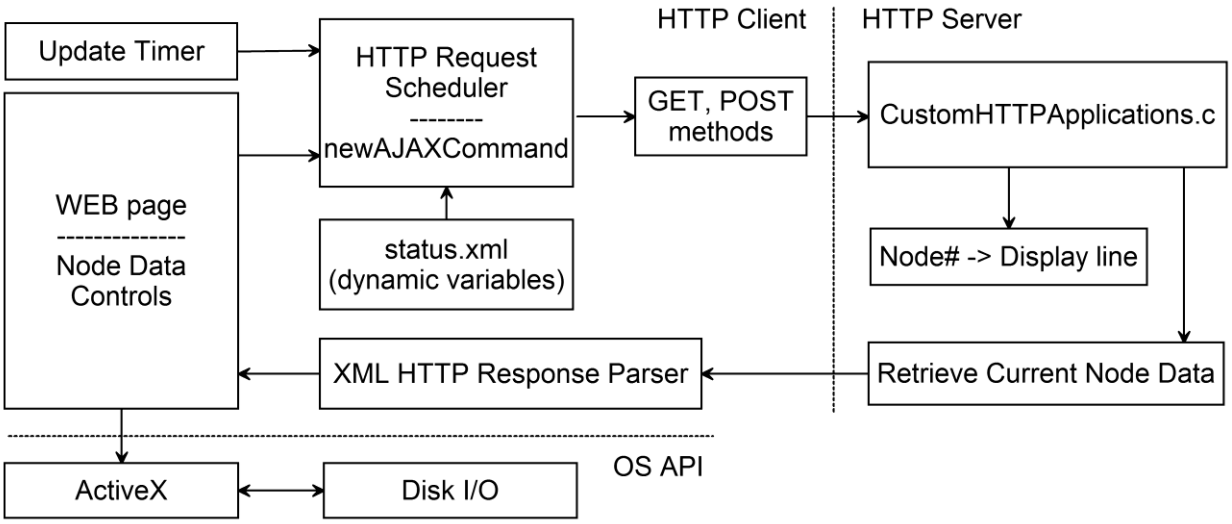

Figure 79. Functional diagram of web engine of the Base GUI.

The user can perform two types of actions from the web page: start logging Node data that is currently active (displayed on the screen) to external text file, and select data of which Node number has to be displayed in particular row. The first operation is accomplished using OS Disk I/O API calls, performed by Microsoft ActiveX component. This method allows a client web browser to create, write, and read files on a file system. File location and name can also be adjusted through the web. The other operation requires sending commands to the HTTP Server.

Every time a user selects a new Node number, the event creates a new GET call to the Server. This call contains information about the row number and selected Node number. A HTTP Request Scheduler then adds this call to the queue. Every time the Update Timer expires, a next call (if available) is popped from the queue and sent to the Server using an XMLHttpRequest component. A timer is required in order to avoid sending requests too frequently.

When a GET request finds an HTTP Server, a special routine (HTTPExecuteGet in CustomHTTPApplications.c) is executed and parameters of call are extracted. Using these parameters, this routine assigns a particular Node Data Array row to the specific user-selected Node number, which allows any new data that arrives to be sorted properly.

In a similar way the Node data is updated on the web page. The routine Update Timer is used to create an additional XMLHttpRequests that contain a list of Node names (actually numbers), enclosed in "~" symbol. These names are taken from status.xml file structure. Each time the HTTP Server receives a "~NodeData(#)~" string, where # represents the Node number, it calls a function HTTPPrint_NodeData from CustomHTTPApplications.c, and passes # as a WORD parameter. In response to this, the function generates a string that contains the current Node data (deliminated by commas) and sends it over the TCP (using stack's routine TCPPutString) back to the client. The response is then organized as an xml data structure and passed to the XML HTTP Response Parser routine, written on JS. This routine extracts the data, separating, formatting and passing it to particular locations on web page screen.

Additional features that were implemented in current revision include graphic elements for battery voltage, update counter, and signal strength indicators, and prompting messages on mouse hover.

5.6 Summary

In this chapter, the hardware and software for the Base unit were presented. Testing and validation of the entire system will be presented in the following chapter.

CHAPTER 6. VALIDATION, CONCLUSIONS AND FUTURE WORK

6.1. Introduction

In this chapter, test results used to validate the Wireless Health Monitor system are presented. Conclusions and future design improvements are then presented.

6.2. Validation

The Wireless Health Monitor system was tested outdoor in different terrain conditions (sight of vision on plain ground surface, near a water basin and close to hills) with the antenna attached directly without the use of an RF cable and at maximum output power (250mW), 1.5m above the ground. This resulted in a strong communication link for distances less than 3km between the Node and the Base. Occasionally, at margin distances in hilly terrain, the Base could miss single package. However, the link was restored during the next update time period. Battery life was found to exceed 20 hours when using 2 AA NiMH 2 A*hr. elements at maximum output power. In addition, a system of 5 nodes and one base were operated for 40 hours continuous without any faults. Figure 80 shows the completely assembled, tested and calibrated devices, ready for shipment.

Table 3 lists actual WHM system major characteristics. At different design stages and during tests, a number of future improvements and better solution (both in hardware and software) were found. Many were left for future work due to time constraints.

The breathing rate measurement works well when the operator is not moving. When the operator moves, the respiration sensor belt gets additional mechanical exposure which can be incorrectly interpreted as a breathing cycle. This problem can be solved improving the digital filtration algorithm, reading the information from an additional sensor belt located around

stomach (which is already supported), or using alternative breathing rate detectors such as air temperature, CO_2 concentration, or flow of breathing volume.

Figure 80. Completely assembled Base and Node devices.

6.3. Conclusions

The objective of the WHM project was to develop a system which can remotely monitor and log body and inner volume temperature, pressure, humidity, respiration rate, pulse rate and hemoglobin oxygenation, oxygen and carbon dioxide concentration.

The system presented here meets or exceeds most of the requirements set forth at the start of this project. In addition, it allows for future upgrades (e.g. accuracy, off-line operation time) as well as the number of nodes to be increased to 16 per base station.

6.4. Future Work

In future upgrades, it is recommended to add a Node sensor calibration feature to simplify the calibration procedure. Currently, one must disassemble the unit and flash MCU to calibrate the system. Instead, calibration could be added to the WEB GUI. At a minimum, the user should be able to update the CO_2 and O_2 coefficients through this WEB GUI interface.

Second, it is recommended to allow the Node firmware to be updated through the web interface without the need to use ICSP. This would allow the user to update their device without having to send it back to a service center.

Table 3. The Wireless Health Monitor system actual characteristics.

Parameter Name	**Units**	**Range / Value**	**Accuracy**	**Precision**
Node-Base interface	-	Radio channel, star	-	-
Tested Node-Base distance range	km	>3	-	-
Max supported number of Nodes	#	10(99)	-	-
Node-specific:				
Body Temperature meas.	°C	+25..+45	0.2	0.1
Body Surrounding Pressure meas.	kPa	20..115	1.8	0.1
Oxygen concentration meas.	% (vol.)	0..41.8	2.0	0.1
Carbon Dioxide concentration meas.	% (vol.)	0..5	0.05	0.01
Inner volume Temperature meas.	°C	-10..+50	1.2	0.1
Inner volume Humidity meas.	% (rel.)	0..100	3.1	1
Heartbeat rate meas.	# per min	40..240	5	1
Hemoglobin oxygenation meas.	%	0..100	3	1
Respiration rate meas.	# per min	0..60	N/A	1
Battery voltage meas.	V	1.8..4.8	0.051	0.01
Sensor Data update period	s	5	0.5	-
Power supply nominal voltage	V	1.8..4.8	-	-
Off-line operation time (2xAA, 2A*h)	hr.	20	-	-
Linear dimensions, LxWxH	mm	100x68x36	-	-
Unit weight	g	120	-	-
Base-specific:				
Power supply nominal voltage	V	5..12	-	-
Max linear dimensions, LxWxH	mm	200x100x80	-	-
Unit weight	g	150	-	-

The real time clock and NV ferroelectric memory in the Base unit still need a firmware code to operate. When this is done, time update/synchronization for RTC and NV memory data retrieve and logging operations should be added as well through the web interface.

The system must be able to put the Node sensor data to internal memory along with a time stamp from a RTC. To aid with monitoring the operators with the Nodes, a graphical display showing time histories are recommended. This functionality can be easily implemented using AS3 language.

The oxygen concentration algorithm must be upgraded to compensate for temperature effects. This will significantly improve accuracy up to ±0.5% vol. There is no need to change anything in hardware for this improvement.

The carbon dioxide NDIR sensor IR lamp works on a lower voltage (3.3 V instead of 5 V). This reduces power consumption and prolongs lamp lifecycle. However in this regime tungsten vaporizes after time, coats the inner glass surface reducing its transparency, and consequently degrades the sensor performance. To avoid this, it is advised to source lamp by 5 V source at device startup for about 30 seconds and then to reduce the voltage to 3.3 V. This function can be implemented by adding boost regulator or using two-output boost regulator.

The NDIR sensor lamp is currently switched on through an RC network that provides a soft start. From a power consumption point, this is a poor solution since power dissipation. Instead, PWM techniques should be used in future versions. Then different lamp switch on and off profiles can be implemented through firmware. This change requires only removing C and shorting R terminal (or putting zero-Ohm resistor).

The NDIR temperature is currently estimated using a second-order curve fit. Since the MCU has sufficient free ROM, a look-up table could be used instead. This will reduce the effect

of local gas temperature measurements and consequently reduce the error in the concentration measurement.

Astronaut's body temperature can be measured indirectly by utilizing infrared thermopile sensor that provides contactless measurement [68]. Sensor field of view can be directed to open skin area (e.g. face) for that purpose. This will reduce the number of connections to a Node. However, accuracy will drop to ±2 °C.

To further improve the CO_2 concentration measurement accuracy, current sources can replace the thermistor and/or FETs resistors. Some PIC MCUs contain programmable current source that can be used for that purpose. Alternatively, a separate IC could be utilized. In the case of using a thermistor, it may also be possible to use short current pulses for the duration of measurement. This will reduce thermistor self-heating and consequent error.

Instead of calculating p-p values for the NDIR detector and reference signals using MCU ADC, it is possible to use an RMS-to-DC converter IC (e.g. AD736 or LTC1966) for that purpose. This will further increase measurement accuracy. Because we don't need to know detector and reference signal values separately but only their ratio, it may also be possible to improve the sensor's analog front end circuit and reduce number of ADC / RMS-to-DC channels from 2 to 1.

For breathing rate measurements, it would be better to use two channels with two sensor belts. Also, due to piezo element aging problem, a new sensor belt that contains optical or magnetic encoder and magnetic strip to detect chest displacement. In any event, the algorithm needs to be improved to reduce sensitivity to motion disturbances and body/hand movements.

Because hemoglobin oxygenation level depends on the amount of O_2 in breathing volume, pulse rate and respiration rate, it may be possible to find a solution to express respiration

rate indirectly using listed parameters from available sensors reducing one more connection to a Node unit. This is another research topic, and probably the solution will require complex individual calibration.

In the current firmware revision gas sampling chamber fan works constantly. Gas flow sensor may be added to measure volume rate and PWM can be used to adjust fan rotation speed accordingly. This will reduce power consumption and noise along with prolonging the fan's life time.

In order to reduce total Node cost in volume production, it may be possible to replace the RF WI232FHSS module by special communication IC and power / low noise amplifier (e.g. CC1190) along with impedance matching circuit. Additional time will be required for communication protocol coding, but this may not be a problem because many manufacturers (TI, Microchip) provide free stacks for their ICs that can be simply customized.

The RF module provides additional information through special pins and registers about data transmission and receiving errors. The state of these pins is currently ignored by firmware (if error occurs, firmware simply clears error register to continue module operation). Communication efficiency may be improved if this information will be taken into account.

The transmitter in the Node is currently works on maximum power. Power consumption can be improved if this power will be adjusted dynamically, analyzing received signal quality and strength along with number of packet retransmissions. Base station may operate like coordinator for this purpose and transmit support information to Nodes about link quality so they may adjust their transmission power.

The current Node algorithm collects data when NDIR lamp is in off state. However it still can collect data when RF module transmits the packet which creates intensive noise in power supply lines and in sensors itself and may affect the sensor reading accuracy.

The MCU in the current firmware revision works continuously. Sleep modes could be utilized when there is no need to perform any operation.

Logging feature on the web interface is currently limited to Internet Explorer due to ActiveX component support. The web engine should be improved to work on any web browser and still have this feature operable. AS3 language can be used for this purpose.

The base station currently has a static IP address. Microchip TCP/IP stack (DNS and DHCP services) has to be configured to make it possible to use dynamic IP address to avoid problems when the device is connected to router or network with automatic configuration. In addition, the name has to be assigned to the Base station, so instead of using an IP address, the user will be able to type static device name (e.g. http://whm/).

REFERENCES

[1] Kenneth S. Thomas and Harold J. McMann, *US Spacesuits*, 1st ed., John Mason, Ed. Chichester, UK: Praxis Publishing, 2006, p. xxv-xxvi.

[2] S. M. Alekseev and S. P. Umanskiy, *High-altitude and space suits*, 1st ed., V. N. Kniazev, Ed. Moscow, USSR: Mashinostroenie, 1973, p. 35-37.
(С. М. Алексеев и С. П. Уманский, *Высотные и космические скафандры*, 1я ред., В. Н. Князев, Изд. Москва, СССР: Машиностроение, 1973.)

[3] S. M. Alekseev and S. P. Umanskiy, *High-altitude and space suits*, 1st ed., V. N. Kniazev, Ed. Moscow, USSR: Mashinostroenie, 1973, p. 37-39.
(С. М. Алексеев и С. П. Уманский, *Высотные и космические скафандры*, 1я ред., В. Н. Князев, Изд. Москва, СССР: Машиностроение, 1973.)

[4] John D. Enderle, Susan M. Blanchard, and Joseph D. Bronzino, *Introduction to Biomedical Engineering*, 2nd ed., Joseph Bronzino, Ed. Hartford, Connecticut, USA: Elsevier Academic Press, 2005, p. 101-103.

[5] M. Zimmerman et al., *Human physiology: In 3 volumes. V. 2.*, 3rd ed., P. Shmidt and G. Tevs, Eds. Moscow, Russia: Mir, 2005, p. 454-466.
(М. Циммерман и др., *Физиология человека: В 3-х томах. Т. 2.*, 3я ред., Р. Шмидт и Г. Тевс, Изд. Москва, Россия: Мир, 2005.)

[6] M. Zimmerman et al., *Human physiology: In 3 volumes. V. 2.*, 3rd ed., P. Shmidt and G. Tevs, Eds. Moscow, Russia: Mir, 2005, p. 422-426.
(М. Циммерман и др., *Физиология человека: В 3-х томах. Т. 2.*, 3я ред., Р. Шмидт и Г. Тевс, Изд. Москва, Россия: Мир, 2005.)

[7] E. Jovanov et al., "A WBAN System for Ambulatory Monitoring of Physical Activity and Health Status: Applications and Challenges," Alabama Univ., Huntsville, Paper 0-7803-8741-4, 2006.

[8] Jamil Y. Khan, Mehmet R. Yuce, and Farbood Karami, "Performance evaluation of a Wireless Body Area sensor network for remote patient monitoring," Univ. of Newcastle, Callaghan, NSW 2308, Australia, Paper 978-1-4244-1814-5, 2008.

[9] Kabir Humaun, Sultana Najnin, and Sup Kwak Kyung, "WBAN in-Body Channel: Dielectric Perspective," *International Journal of Digital Content Technology and its Applications*, vol. 3, no. 3, September 2009.

[10] Lin Zhong et al., "OsteoConduct: Wireless Body-Area Communication based on Bone Conduction," Rice Univ., , Houston, TX, Paper 2007.

[11] Sudip Misra, Isaac Woungang, and Subhas Chandra Misra, *Guide to Wireless Sensor Networks*, 1st ed., A. J. Sammes, Ed. London, UK: Springer, 2009, p. 27-44.

[12] Laura Mason, Signal Processing Methods for Non-Invasive Respiration Monitoring, 2002, Thesis, Univ. of Oxford, Dept. of Engineering Science.

[13] Amy Diane Droitcour, Non-contact Measurementof Heart and Respiration Rates with a Single-chip Microwave Doppler Radar, 2006, Thesis, Stanford Univ., Dept. of Electrical Engineering.

[14] (2007) Nonin Medical Inc. Website. [Online]. http://www.nonin.com/documents/OEM%20III%20Module%20Specifications.pdf

[15] R. C. Adams, R. S. Abramo, and D. W. Von Mueller, "COMWIN Antenna Project: Fiscal Year 2001 Final Report," SPAWAR Systems Center, San Diego, CA, Technical Report

1866 20011025063, 2001.

[16] Ian F. Akyildiz and Mehmet Can Vuran, *Wireless Sensor Networks*, 1st ed., Ian F. Akyildiz, Ed. Chichester, West Sussex, UK: John Wiley & Sons Ltd., 2010, p. 28-29.

[17] R. Jafari et al., "Wireless sensor networks for health monitoring," Dept.of Comput. Sci., California Univ., Los Angeles, CA, Paper 0-7695-2375-7, 2005.

[18] Abniman Hande, Todd Polk, William Walker, Joel Votaw, and Dinesh Bhatia, "Wireless Sensor Networks for Remote Health Monitoring," Center for Integrated Circuits and Systems, The Univ. of Texas at Dallas, Dallas, TX, Paper 2005.

[19] I. P. Abramov et al., *Russian spacesuits*, 1st ed. Moscow, Russia: Zvezda, 2005, p. 280-282. (И. П. Абрамов и др., *Космические скафандры России*, 1е изд. Москва, Россия: Звезда, 2005.)

[20] D. A. Hrustalev, Rechargable batteries, 1st ed. Moscow, Russia: Izumrud, 2003, p. 11-25. (Д. А. Хрусталев, *Аккумуляторы*, 1е изд. Москва, Россия: Изумруд, 2003.)

[21] (2008, June) Mobipower Website. [Online]. http://mobipower.ru/modules.php?name=News&file=article&sid=92

[22] Jim Williams. (2005, July) Linear Technology Website. [Online]. http://cds.linear.com/docs/Application%20Note/an101f.pdf

[23] (2011, September) Texas Instruments Website. [Online]. http://www.ti.com/lit/ds/symlink/tps61025.pdf

[24] (1994, August) International Rectifier Website. [Online]. http://www.irf.com/technical-info/designtp/dt94-8.pdf

[25] (2008, March) Vishay Website. [Online]. http://www.vishay.com/docs/73164/73164.pdf

[26] (2010, July) Microchip Website. [Online]. http://ww1.microchip.com/downloads/en/DeviceDoc/39951C.pdf

[27] (2008, January) Maxim Website. [Online]. http://datasheets.maxim-ic.com/en/ds/MAX6394.pdf

[28] Erich Gnaiger, "Polarographic Oxygen Sensors, the Oxygraph, and High-resolution Respirometry to Assess Mitochondrial Function," in *Drug-Induced Mitochondrial Dysfunction*, James Dykens and Yvonne Will, Eds. New York, USA: John Wiley & Sons, 2008, ch. 12, pp. 327-352.

[29] Richard C. Dorf, *Sensors, Nanoscience, Biomedical Engineering, and Instruments*, 3rd ed., Richard C. Dorf, Ed. Davis, CA, USA: Taylor & Francis Group, 2006, p. 112-116.

[30] (2005, June) Figaro Website. [Online]. http://www.figarosensor.com/products/O2.pdf

[31] (2001, October) City Technology Website. [Online]. http://www.citytech.com/PDF-Datasheets/ao3.pdf

[32] (2009, November) Alphasense Website. [Online]. http://alphasense.com/pdf/O2A3.pdf

[33] (2006) Linear Technology Website. [Online]. http://cds.linear.com/docs/Datasheet/600345fd.pdf

[34] (2006, January) Figaro Website. [Online]. http://www.figarosensor.com/products/4160pdf.pdf

[35] (2010, December) Alphasense Website. [Online]. http://www.alphasense.com/pdf/CO2D1.pdf

[36] Elisabetta Comini, Guido Faglia, and Giorgio Sberveglieri, *Solid State Gas Sensing*, 1st ed. New York, USA: Springer, 2009, p. 27-33.

[37] (2009) Chemical, Forensic, Food & Environmental Technology Website. [Online]. http://cffet.net/air/ch4-f.shtml

[38] John G. Webster, *Measurement, Instrumentation, and Sensors Handbook*, 1st ed., John G. Webster, Ed. Boca Raton, FL, USA: CRC Press, 1999, p. 1063-1066.

[39] (2009, August) City Technology Website. [Online]. http://www.citytech.com/PDF-Datasheets/ircelco2.pdf

[40] (2011, May) Dynament Website. [Online]. http://www.dynament.com/infrared-sensor-data/tds0037.pdf

[41] (2009, June) Alphasense Website. [Online]. http://www.alphasense.com/pdf/NDIR_carbon_dioxide_IR.pdf

[42] (2009, March) Alphasense Website. [Online]. http://alphasense.com/alphasense_sensors/ndir_specs.html

[43] (2009, March) Alphasense Website. [Online]. http://www.alphasense.com/pdf/NDIR/AAN_205-02.pdf

[44] (2006, March) Texas Instruments Website. [Online]. http://www.ti.com/lit/ds/symlink/opa333.pdf

[45] Jacob Fraden, *Handbook of modern sensors: physics, designs, and applications*, 3rd ed., Jacob Fraden, Ed. New York, USA: Springer, 2003, p. 470-472.

[46] (2009, March) Alphasense Website. [Online].

http://www.alphasense.com/pdf/NDIR/AAN_202-03.pdf

[47] John G. Webster, *Measurement, Instrumentation, and Sensors Handbook*, 1st ed., John G. Webster, Ed. Boca Raton, FL, USA: CRC Press, 1999, p. 643-651.

[48] (2011, August) Freescale Website. [Online]. http://cache.freescale.com/files/sensors/doc/data_sheet/MP3H6115A.pdf

[49] John G. Webster, *Measurement, Instrumentation, and Sensors Handbook*, 1st ed., John G. Webster, Ed. Boca Raton, FL, USA: CRC Press, 1999, p. 964-1022.

[50] Milind Gupta. (2010, January) EDN Website. [Online]. http://www.edn.com/article/458210-Determine_your_IC_s_transient_thermal_behavior_to_prevent_overheating.php

[51] Jacob Fraden, Handbook of modern sensors: physics, designs, and applications, 3rd ed., Jacob Fraden, Ed. New York, USA: Springer, 2003, p. 398.

[52] (2008) GE Website. [Online]. http://www.cdiweb.com/datasheets/ge_generaleastern/920_426A_E_LR.pdf

[53] (2011) Analog Devices Website. [Online]. http://www.analog.com/static/imported-files/data_sheets/ADT7410.pdf

[54] John D. Enderle, Susan M. Blanchard, and Joseph D. Bronzino, *Introduction to Biomedical Engineering*, 3rd ed., Joseph D. Bronzino, Ed. Hartford, Connecticut, USA: Elsevier Academic Press, 2005, p. 530-534.

[55] (2007) Nonin Medical Website. [Online]. http://www.nonin.com/documents/OEM%20III%20Module%20Specifications.pdf

[56] (2006, June) Nonin Medical Website. [Online]. http://www.nonin.com/documents/Technical_Bulletin_OEM_III.pdf

[57] Tobey Clark . (2007) The University of Vermont Website. [Online]. http://its.uvm.edu/medtech/module.html

[58] I. Y. Immoriev, S. N. Pavlov, S. V. Samkov, and E. V. Solodov. (2005, December) UWB Russian Group. [Online]. http://uwbgroup.ru/pdf/05_mvturus_id01p.pdf

[59] (2010) Xavitech Website. [Online]. http://www.xavitech.com/images/datasheets/p200_gas_100401.pdf

[60] (2005, June) Bartels Microtechnik Website. [Online]. http://www.pro-4-pro.com/media/product_data/42b6c691a40f1/download.pdf

[61] Copal Website. [Online]. http://www.nidec-copal-usa.com/pdfs/F16fan.pdf

[62] (2005, September) Radiotronix Website. [Online]. http://www.radiotronix.com/datasheets/datasheets/WI232FHSS-250-R_25-RUsersManualrev1_0_0.pdf

[63] (2009) Microchip Website. [Online]. http://ww1.microchip.com/downloads/en/devicedoc/39951b.pdf

[64] (2008, May) National Semiconductor Website. [Online]. http://www.ti.com/lit/ds/symlink/dp83848c.pdf

[65] (2008, April) National Semiconductor Website. [Online]. http://www.ti.com/lit/an/snla079c/snla079c.pdf

[66] Rajbhart Niles. (2008) Microchip Website. [Online].

http://ww1.microchip.com/downloads/en/AppNotes/00833c.pdf

[67] Sea Justic. Microchip Website. [Online].

http://ww1.microchip.com/downloads/en/AppNotes/HTTP_Server_BSD_01107B.pdf

[68] (2011, July) Texas Instruments Website. [Online].

http://www.ti.com/lit/ds/symlink/tmp006.pdf

[69] (2009, June) Alphasense Website. [Online].

http://www.alphasense.com/pdf/NDIR/AAN_201-05.pdf

APPENDIX A. USER INTERFACE AND QUICK STARTING GUIDE

User Interface

The Base and Node devices were designed to reduce the complexity of the system use. The Node's external connections and controls are shown on Figure A.1, assuming that the device is not installed in the spacesuit.

First, user must attach all required external sensors (Breathing rate, Pulse rate and hemoglobin oxygenation, Body temperature sensors and pipe to input gas sampling chamber terminal if required). The user must ensure that the gas sampling blow-out fan and ventilation holes will not be covered with any obstacles within 4-6 inches.

Next, the antenna or RF cable with antenna must be connected (rev. C device has SMA-RP, and rev. D has SMA-F connector). Once connected, the power supply cable can be connected and the Node device can be switched on using toggle switch located near the Body temperature sensor connector.

Once turned on, the Node will start to operate. Every 5 seconds, a green LED (located above the power switch) will blink indicating a data package has been sent to the Base. If some external sensors are not attached or fail to operate, the device will still function properly and sensor errors will be shown on GUI. The Node number and device revision is shown on the top sticker.

The base connections and controls are shown on Figure A.2. First, the Antenna or RF cable must be attached to SMA-RP connector. Next, the power supply can be connected along with RJ-45 plug and Ethernet cable. The PHY chip in the Base supports automatic detection of crossover and direct cable wiring, but this will only work if Ethernet controller on the opposite side also supports this functions.

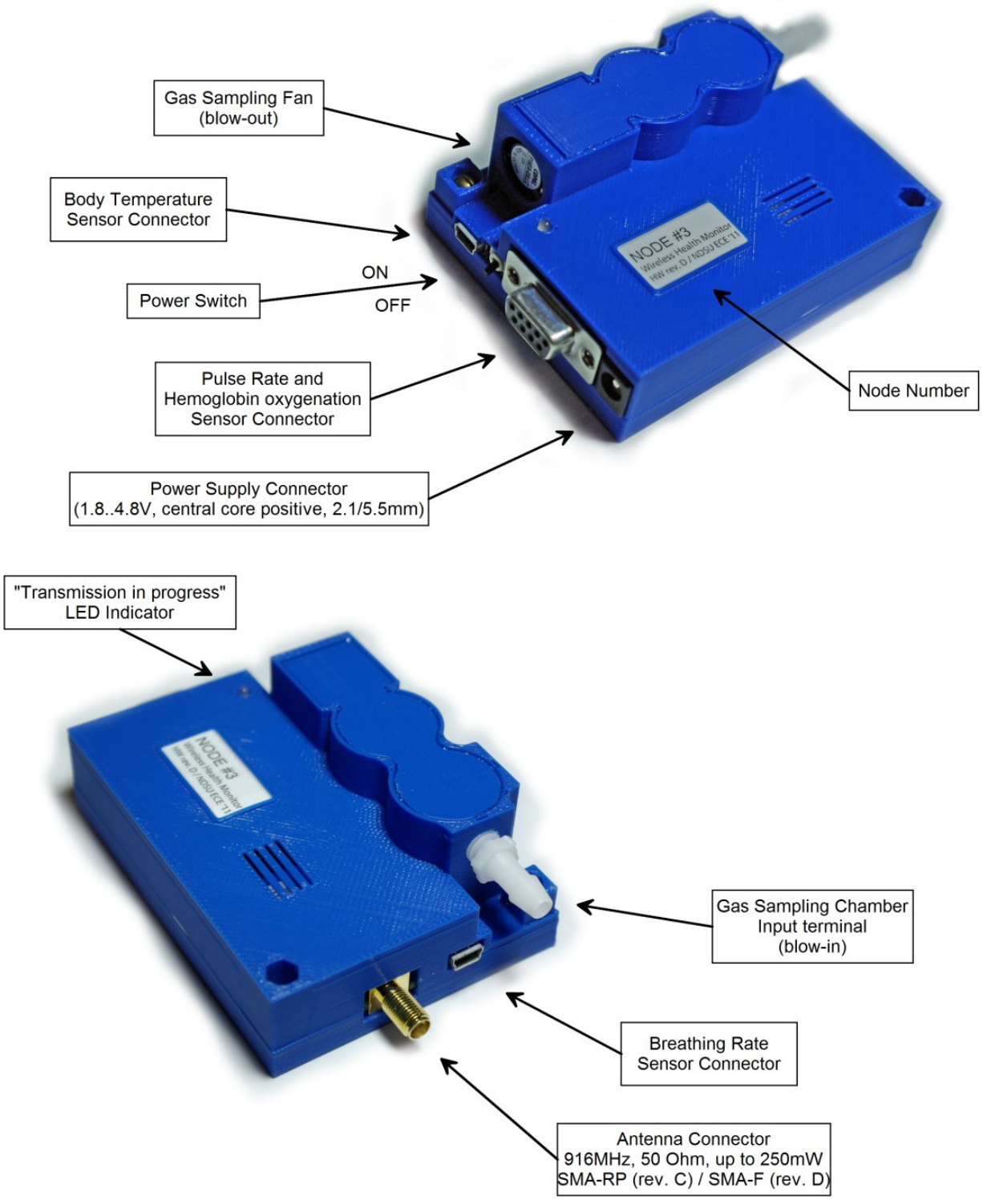

Figure A.1. Node device external connections and controls.

Since all modern controllers have this function, there should be no problems with using any cable type and connecting to any Ethernet-enabled equipment. However, if the problem with connection occurs, one must try to use crossover cable while connecting directly to a PC, or direct cable (patch cord) while connecting to switch or router. In this manual, it is assumed that the Base is connected directly to PC.

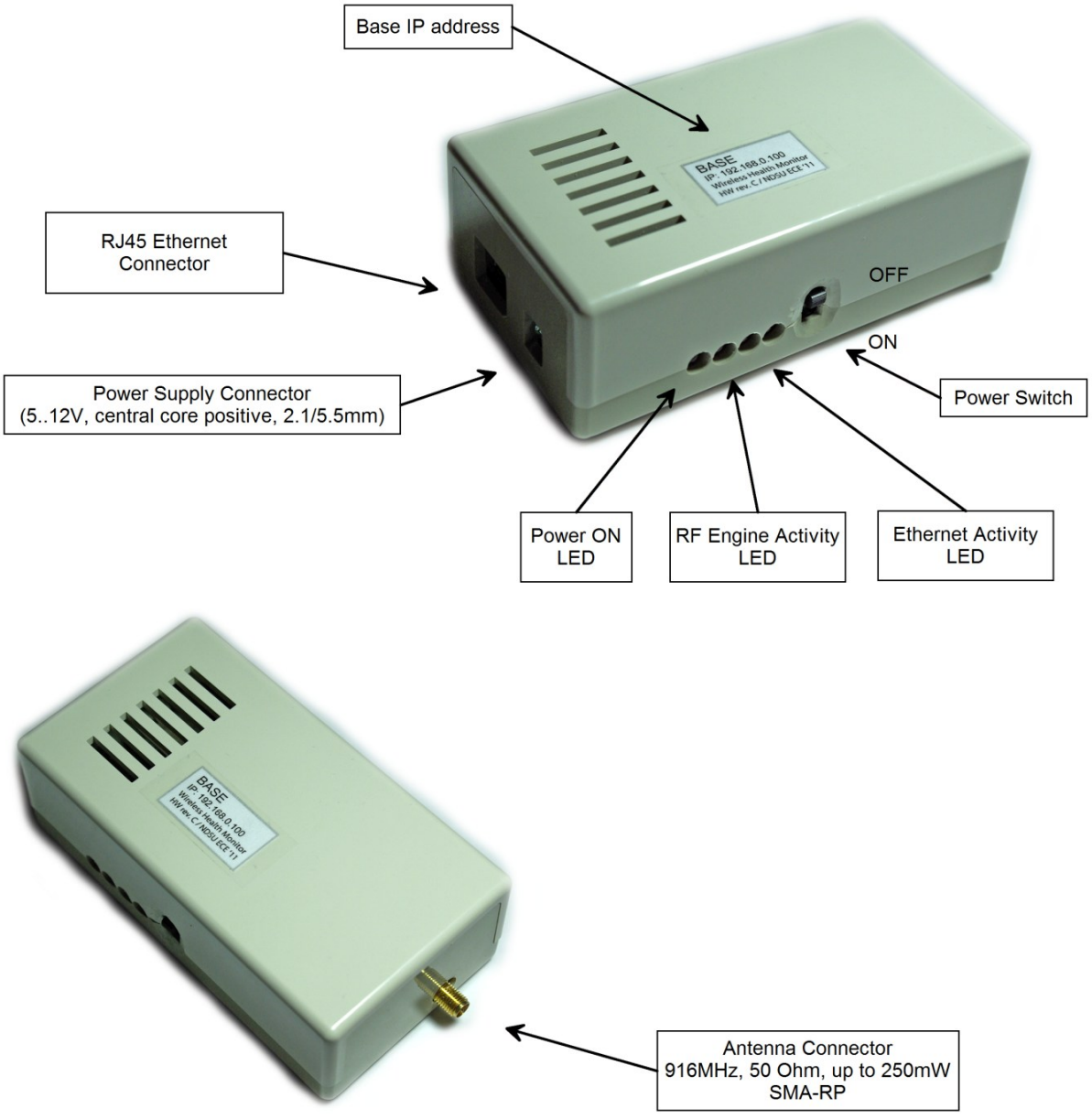

Figure A.2. Base device external connections and controls.

Once connected to the power supply, the power switch can be put to bottom position in order to switch the device on. The Power ON red LED will light and the RF Engine Activity LED will blink every time the Base receives a valid package from a Node. If the Ethernet connection with the PC has been established successfully, green LEDs on Ethernet connectors on both sides will constantly light and red LEDs will blink when packages are transmitted or received. The Ethernet Activity LED on the Base will blink only when the client web browser sends request to the HTTP Server.

The Base should work with any web browser (it was tested on IE, Mozilla, and Chrome), however data logging to file feature will only work in IE. This limitation is due to IE support of Active X components required for OS file system operations.

Before connecting to the Base, some IE settings must be adjusted in order to properly display the page. In browser Setting - Security, the user must enable File loading, ActiveX, and JavaScript components. After a browser restart, connection with Base HTTP Server can be established by typing 192.168.0.100 in address field and pressing Enter. Current firmware revision uses a static IP address, which is shown on the top sticker of the Base. After that, web page will be loaded as presented in Figure A.3.

Node information is organized in a table. The top row contains short name abbreviations of every column parameter. The user can hover the mouse pointer on the abbreviation text area to get more detailed information, as is shown for GTP (Gas Temperature). All abbreviations used on the web page are summarized and explained in Table A.1.

The user interface is fairly simple. In the Node ID drop-down menu, the user must select one of the available Node names that must be displayed in the current row. After selection, every field in the row will be updated every 5 seconds with the data from Node

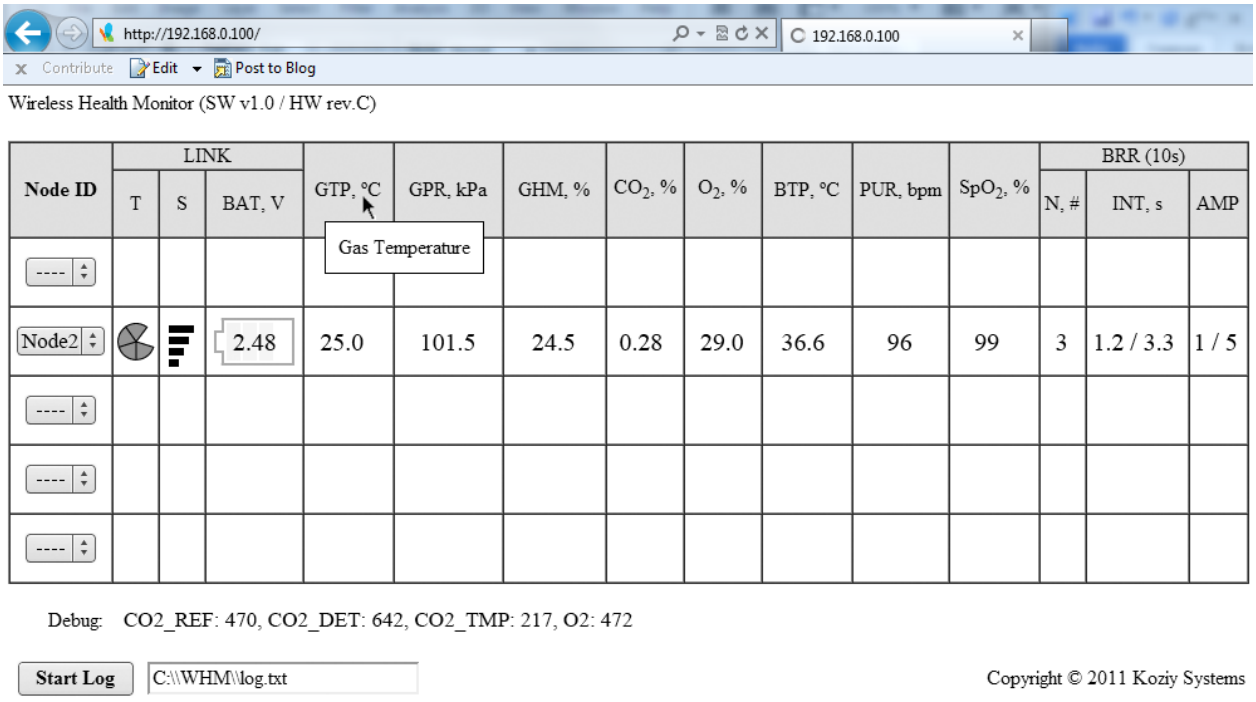

Figure A.3. Web page with GUI for the WHM system.

Table A.1. Parameter description on Web page GUI.

Parameter	Units	Description	Range
T	s	Node data update timer. Graphic symbol	0..10
S	dBm	RF signal strength indicator. Graphic symbol	-105...-20
BAT	V	Battery voltage	0.8...4.2
GTP	°C	Temperature in gas sampling chamber (SC)	-10...+50
GPR	kPa	Pressure in the outer volume	15..115
GHM	% (rel.)	Humidity in gas SC	0...99
CO_2	% (vol.)	Carbon dioxide concentration in SC	0...5
O_2	% (vol.)	Oxygen concentration in SC	0...50
BTP	°C	Body temperature	+25...+45
PUR	#/min	Pulse rate	40...240
SpO_2	%	Hemoglobin oxygenation level	0...100
BRR- N	#/12s	Respiration rate – number of cycles	0...60
BRR- INT	s	Respiration rate – max/min interval between cycles	0...12
BRR- AMP	-	Respiration rate – max/min displacement amplitude	0...9
CO2_REF	-	CO_2 sensor – reference channel – direct ADC value	0...1023
CO2_DET	-	CO_2 sensor – detector channel – direct ADC value	0...1023
CO2_TMP	-	CO_2 sensor – temperature – direct ADC value	0…1023
O2	-	O_2 sensor – direct ADC value	5...440

(if it is active and within range). Figure A.3 gives an example of Node2 selection in row 2. The Node data update timer is shown as a pie diagram symbol that counts using light color sections during the first 5 seconds. If a message has not been received in 5 seconds, it proceeds to count for 5 more seconds using dark color sections. If no update is received within 10 seconds, the update timer will become completely dark and the signal strength indicator will show link error symbol. Once connection is reestablished, the timer will again start to count and S indicator will show the most recent RF signal level.

The Node battery voltage field shows both voltage level and approximate battery capacity as graphic symbol. System was adjusted for NiCd/NiMH and Li-Ion battery voltage ranges. However, due to some overlap between maximum NiCd and minimum Li-Ion voltages, or in case of using other power supply sources, there may be errors in graphic symbol representation of current battery capacity.

The user may change the Node name in row by simply selecting another Node name. It is also possible to clear the row from data by selecting "---" name in Node ID drop-down menu. If the Node sensor fails to operate, the user will see "---" in the corresponding field. In the current Node FW revisions (C and D), the body temperature sensor operation is verified only at power on; if it fails during operation, the body temperature reading will show the last valid temperature.

A debug line is at the bottom of the table for test and calibration purposes. To use it properly, only one Node name must be selected for displaying. The debug line will show most recent calibration data for this Node.

In order to log data to a text file, first it is required to select the path to file and file name with txt extension in field near "Start Log" button. In the file path, "\" symbols must be replaced

by the "\\" string. By pressing the "Start Log" button, the system will check if the path to the text file (drive letter and folder structure) exists. If not, the appropriate folders will be created.

If a file with the specified file name already exists, the new data will be appended to the end. If not, file will be created. Data will be recorded to file in the same sequence as the web page, delimited by comma. Every Node data will be added to new line. In addition, Node name, OS date and time stamp will be provided. "Start Log" button label will change to "Stop Log" indicating that logging process is in progress. Only Nodes selected in Node ID will be logged. If error occurs during file access or creation, pressing "Start Log" button will not change its label to "Stop Log", and error message "I/O Error" will be displayed. Pressing "Stop Log" button will stop logging process. Later it can be resumed if required.

If the web page will be reloaded, all most recent settings (selected Node names and log state) will be restored. However, if the Base device will lose power, the user will need to select Nodes again and probably to restart logging procedure.

APPENDIX B. SENSOR CALIBRATION PROCEDURES

In the current Base and Node firmware revisions, automatic sensor calibration has not been implemented. Instead, manual calibration is required for every Node module before it can be used in the system. This appendix describes the sensor characteristics and calibration procedures (when applied). For all formulas used below, ADC means raw ADC readings under unknown environment and conditions, and ADCX means raw ADC readings under known (set and fixed) conditions.

Oxygen Sensor

Oxygen sensor O2-A3 response raw ADC value has to be recorded for two conditions: in pure nitrogen (0% vol. O_2, zero point) and in 20.9% vol. O_2 in nitrogen. Temperature has to be the same for both points. O_2 concentration then can be calculated:

$$O_2(ADC) = 20.9 * \frac{ADC - ADC_0}{ADC_{20.9} - ADC_0} \quad (33)$$

where ADC is raw ADC value in unknown O_2 concentration, ADC_0 - raw ADC value at zero point, and $ADC_{20.9}$ - raw ADC value at 20.9% vol. O_2 point. ADC range is 5...440.

For oxygen sensor calibration, zero point was set connecting a nitrogen tank to Node gas chamber terminal, setting gas flow to 1L/min for about 2 minutes and recording temperature and raw ADC O_2 data from debug string on web page GUI. The 20.9% vol. O_2 point was approximately set by leaving the Node device on open area outdoor and recording the same parameters. Coefficients then had to be put to Node MCU flash ROM. For more precise results, a calibrated gas mixture should be used. Under normal sensor use, calibration procedure has to be done every 6 month. However if sensor is used for a long time at higher (> 20.9% vol.) oxygen concentrations, the procedure has to be accomplished every week to keep high measurement accuracy.

Carbon Dioxide Sensor

The Carbon dioxide sensor IRC-A1 also requires calibration. The sensor produces 3 parameters: local gas temperature, detector output and reference output. For temperature measurement, an internal thermistor is used. Its resistance values under different temperatures can be obtained from the sensor's datasheet. Based on this data, a second order polynomial was defined to approximate the data:

$$GTP_{CO_2}(ADC) = ADC^2 * 0.00007174 - ADC * 0.1557624 + 76.07396 \quad (34)$$

The ADC range is 0…1023. Figure B.1 shows dependence of actual (Y_N) and approximated (YA_N) temperature from raw ADC readings.

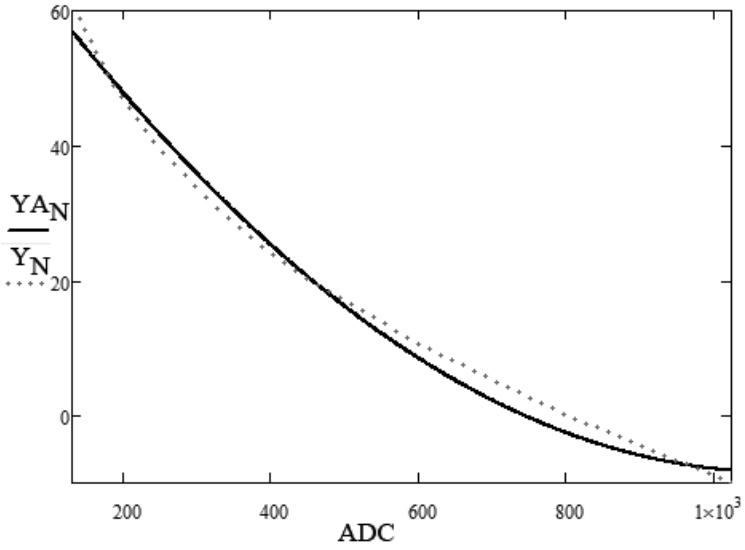

Figure B.1. Actual and calculated gas temperature versus ADC readings.

Before CO_2 concentration can be calculated, constants and calibration coefficients must be defined. Constants were taken from the sensor datasheet: α = 0.0007, β = 0.0014, b = 0.52, c = 0.68. Local gas temperature T_{cal} (during calibration) at 0% and 2.5% vol. CO_2 in bump gas (nitrogen) points must be determined reading CO2_TMP value in the web page debug string. The next values for every sensor must be retrieved individually also using debug information:

ACT_0 and ACT_4 (ADC raw p-p value of detector output at 0% and 2.5% vol. CO_2 environment respectively), REF (ADC raw p-p value of reference output). A gas calibration mixture was purchased to produce 2.5% vol. CO_2 environment. Based on these values, the calibration coefficients can be obtained:

$$ZERO = \frac{ACT_0}{REF},\ ABS_4 = 1 - \frac{ACT_4}{REF*ZERO},\ SPAN_4 = \frac{ABS_4}{1-\exp(-b*x^c)} \tag{35}$$

where ZERO is the ratio of detector to reference p-p signals in the absence of CO_2, ABS_4 is absorbance at known CO_2 concentration (2.5% vol. for 0…5% NDIR sensors) and $SPAN_4$ is a proportion of radiation that impinges on the active element of the detector that has the ability to be absorbed by the target gas. Using (35), temperature corrected CO_2 concentration $CO2_C$ can be estimated as [69]:

$$CO2_C = \frac{T}{T_{cal}} * \left(\frac{\ln\left(1-\frac{\left(-\frac{ACT}{REF*ZERO}\right)*(\alpha*(T-T_{cal})+1)+1}{SPAN_4+\beta*(T-T_{cal})}\right)}{-b}\right)^{\frac{1}{c}} \tag{36}$$

where T is current local gas temperature measured by the internal thermistor. This formula after significant optimization for fixed and floating point calculations was used in MCU algorithm. Accuracy for CO_2 concentration measurement in the current system is better than ±1% FS, which leads to an error of ±0.05% vol. CO_2. Accuracy can be improved by using higher-resolution ADC and by scaling sensor outputs for every sensor individually to use full ADC input range for gas concentration measurement range.

Other Sensors

The rest of sensors used in the system don't require calibration. Omitting intermediate calculations, humidity can be estimated (for ADC range 0…1023):

$$GHM(ADC) = ADC * 0.09769 \tag{37}$$

Gas temperature is calculated using equation (for ADC range 385…962):

$$GTP(ADC) = ADC * 0.10391 - 500 \quad (38)$$

Gas pressure is calculated using the next equation (for ADC range 40…945):

$$GPR(ADC) = ADC * 0.10391 - 500 \quad (39)$$

Node battery voltage equation (for ADC range 240...865) is

$$BAT(ADC) = ADC * 0.00489 \quad (40)$$

APPENDIX C. PROJECT BUDGET

The cost of this project was calculated based on bill of materials used and engineer time spent on design, prototypes fabrication, testing and calibration. The real cost was lower, because some components were in NDSU stock or left from previous groups that were working on a similar projects, some were ordered as free engineering samples.

Table C.1. Node rev. D device budget for 1 unit. Includes components and materials.

Comp. / Mat.	**Quan.**	**Brief description**	**Price, $**
IRC-A1, 0..5% range	1	NDIR CO2 Sensor, 0..5% range	106
O2-A3	1	O2 Sensor, 3 years, electrochemical cell	42
Nonin OEM III	1	NONIN Pulse/SpO_2 measurement unit	300
Nonin 8000Q	1	NONIN Ear Clip Sensor	120
GRM1555C1H120JZ01D	2	Cap Chip 12pF 50V 0402	0.04
C1005X7R1H471K	1	Cap Chip 470pF 50V 0402	0.02
GRM188R71H103KA01D	4	Cap Chip 10nF 50V 0603	0.08
C1005X5R1A104K	5	Cap Chip 0.1uF 10V 0402	0.1
C1005X5R0J105K	2	Cap Chip 1uF 6.3V 0402	0.08
T520D476M016ATE035	2	Cap 47uF 16V 7343	5.74
C1608X7R1H471K	1	Cap Chip 470pF 50V 0603	0.03
C1608Y5V1C104Z	10	Cap Chip 0.1uF 16V 0603	0.3
GRM188F51C474ZA01J	2	Cap 470nF 16V 0603	0.12
GRM155R61A564KE15D	2	Cap Chip 0.56uF 10V 0603	0.26
C1608Y5V1C105Z	6	Cap Chip 1uF 16V 0603	0.24
C1608Y5V1C225Z	1	Cap Chip 2.2uF 16V 0603	0.08
C1608X5R0J475M	2	Cap Chip 4.7uF 6.3V 0603	0.18
298D106X06R3M2T	1	Cap 10uF 6.3V 0603	1.21
GRM31CR60J476KE19L	1	Cap 47uF 6.3V 1206	0.42
T520B107M006ATE018	1	Cap 100uF 6.3V 18mOhm	1.52
ERJ-6GEYJ100V	1	Res 10 Ohm 5% 0.125W 0805	0.04
754-RG2012N-470-W-T1	1	Res 47 Ohm 0.05% 0805	1.32
CR0603-JW-101GLF	1	Res 100 Ohm 5% 0.1W 0603	0.02
CR0603-JW-331GLF	1	Res 330 Ohm 5% 0.1W 0603	0.02
CR0603-JW-471GLF	1	Res 470 Ohm 5% 0.1W 0603	0.02
CR0603-JW-102GLF	2	Res 1kOhm 5% 0603	0.04
RG1608P-1071-B-T5	1	Res 1.07kOhm 0.1% 0603 25ppm	0.41
TNPW06031K30BEEA	2	Res 1.3kOhm 0.1% 0603	1.28

Table C.1 (cont.) Node rev. D device budget for 1 unit. Includes components and materials.

Comp. / Mat.	Quan.	Brief description	Price, $
302-1.5K-RC	1	Res 1.5kOhm 1% 0603	0.04
CR0603-JW-472ELF	2	Res 4.7k Ohm 5% 0.1W 0603	0.04
ERJ-3EKF6801V	1	Res 6.8k Ohm 1% 0603	0.04
CR0603-JW-103GLF	1	Res 10k Ohm 5% 0.1W 0603	0.02
RG1608P-1132-B-T5	1	Res 11.3kOhm 0.1% 0603 25ppm	0.41
CR0603-JW-363ELF	2	Res 36kOhm 5% 0603	0.04
288-0603-38.3K-RC	1	Res 38.3kOhm 0.1% 0603 10ppm	0.75
TNPW060347K5BEEA	3	Res 47.5kOhm 0603 0.1% 25ppm	1.65
RK73H1JTTD6652D	2	Res 66.5kOhm 0603 0.5% 100ppm	0.3
CR0603-JW-104GLF	5	Res 100k Ohm 5% 0.1W 0603	0.1
754-RR0816P-104D	4	Res 100kOhm 0.5% 0603	0.52
CRT0603-BY-1003ELF	4	Res 100k Ohm 0.1% 0603	1.0
ERA-3AEB334V	1	Res 330kOhm 0.1% 0603	0.54
660-RK73H1JTTD3903F	4	Res 390kOhm 1% 0603	0.32
CR0603-JW-105GLF	1	Res 1MOhm 5% 0.1W 0603	0.02
CR0603-JW-515ELF	2	Res 5.1MOhm 5% 0603	0.04
MPZ2012S102A	2	Ferrite 1kOhm 1.5A 0805	0.14
563-1106-ND	1	Fan 3.3V 20mA	11.16
CP-037A-ND	1	Power Jack	0.79
GT12MABE	1	Switch SPST	7.16
NC7SZ32P5XCT-ND	1	Logic, 2OR Gate, SC70-A	0.66
LT6003CS5#TRMPBF	1	Op Amp	1.76
SSL-LX3044HPGW	1	LED Bi-color	1.05
ABS10-32.768KHZ-T	1	Crystal 32.768kHz 12.5pF	1.02
750-CPDU5V0	1	TVS BI 5V	0.48
OPA2333AIDR	2	Op Amp	8.88
54819-0519	2	USB Socket	4.2
GLFR1608T470M-LR	1	Inductor 47uH 30mA	0.3
Wi.232FHSS-250-R	1	RF Module	38
CHIPCAP-L	1	Temperature / Humidity Sensor	22.5
TPS61025DRCR	1	Switching Regulator	1.9
MP3H6115A6U	1	Pressure sensor	9.25
OPA2347	1	Op Amp	1.89
ADT7410	1	Temperature Sensor	3.15
142-0701-871	1	SMA, Jack, Female Socket	4.96
SI2312BDS-T1-E3	2	MOSFET N-ch, 20V, 31mOhm	1.28
Si7858	1	MOSFET 12V 29A 26mOhm	2.3

Table C.1 (end). Node device rev. D budget for 1 unit. Includes components and materials.

Comp. / Mat.	Quan.	Brief description	Price, $
XAL4040-103	1	Inductor 10uH	1.6
ERJ-3EKF1003V	10	Res 100k Ohm 1% 0603	0.4
NOSV687M004R0075	1	Cap Polymer 680uF 4V	11.9
MAX8510EXK30	1	LDO 3V	0.9
MAX6166A	1	REF 2.5V	4.5
ADR127	1	REF 1.25V	3.7
PIC24FJ64GA104-I/PT	1	MCU	4.71
MAX6394	1	Supervisor, 3.1V	1.8
T491B157M004AT4394	1	Cap Chip 150uF 4V 1210	1.6
EDBS06TTE5V0	1	ESD	0.2
SSW-150-01-G-D	1	Header 2x8	0.15
PGB102ST23	1	ESD	0.08
372-0-15-15-13-27-10-0	9	Pin Receptacle	8.5
PCB	1	PCB fabrication (Advanced Circuits)	37
Enclosure (material)	1	Custom enclosure fabrication	25
KS5	1	Threaded connector ¼-28 UNF, 5.8mm	0.25
HH-3632	1	2 AA battery holder	1.7
Total:			813.82

Table C.2. Base device rev. C budget for 1 unit. Includes components and materials.

Comp./Mat.	Quan.	Brief description	Price, $
GRM188R71H104KA93D	50	Cap Chip 0.1uF 50V 0603	1.85
C1608Y5V0J475Z	10	Cap Chip 4.7uF 6,3V 0603	1.21
T520D476M016ATE035	4	Cap 47uF 16V 7343	11.48
132289RP	2	SMA RP Receptacle	16.58
ERJ-3EKF4701V	20	Res 4.7k Ohm 0603	0.8
MPZ2012S102A	10	Ferrite 1kOhm 1.5A 0805	0.69
C1608Y5V1A105Z	10	Cap Chip 1uF 10V 0603	0.35
GRM188R71H103KA01D	10	Cap Chip 10nF 50V 0603	0.17
ERJ-3GEYJ330V	20	Res 33 Ohm 0603	0.6
ERJ-3EKF1501V	20	Res 1.5k Ohm 0603	0.8
ERJ-3EKF2201V	20	Res 2.2k Ohm 0603	0.8
CC0805ZKY5V6BB106	10	Cap Chip 10uF 10V 0805	1.19
BRC1608TR20M	2	Inductor 200nH 980mA	1.16
ERJ-3EKF4871V	10	Res 4.87k Ohm 0603	0.4

Table C.2 (end). Base device rev. C budget for 1 unit. Includes components and materials.

Comp./Mat.	Quan.	Brief description	Price, $
F930J106MAA	2	Cap Chip 10uF 6.3V 1206 3Ohm	0.88
ERJ-3EKF3300V	10	Res 330 Ohm 1% 0603	0.4
ERJ-3EKF2401V	20	Res 2.4k Ohm 0603	0.8
CR-1220-1FCE	1	Battery Lithium 3V 35mA*H	1.25
ERJ-3EKF2400	20	Res 240 Ohm 0603	0.8
CDCLVC1103PWR	2	Clock Buffer	6.3
BLM18BD221SN1D	10	Ferrite 220 Ohm 200mA 0603	0.54
W0603LF-03-49R9-B	5	Res 49.9 Ohm 0.1% 0603	2.8
ERJ-3EKF2400	20	Res 240 Ohm 0603	0.8
GRM188R71H102KA01D	10	Cap Chip 1000pF 50V 0603	0.19
SI-60062-F	1	RJ45 Jack With Magnetics	5.09
PJ-102A	1	Power connector	0.4
SMAJ16CABCT-ND	2	TVS 16V 400W B	0.38
C3225Y5V1C106Z/1.15	10	Cap Chip 10uF 16V 1210	0.76
EG2480-ND	1	Switch	3.6
RB751S40	2	Schottky 30mA 40V	4.07
Wi.232FHSS-250-R	1	RF Module	38
298D106X06R3M2T	2	Cap 10uF 6.3V 0603	2.42
DP83848CVV	1	Ethernet PHY	6.8
FM25V10-G	1	Ferroelectric memory	12.91
PIC32MX695F512H	1	MCU	8.92
MAX3207E	1	ESD	0.95
MAX6394	1	Reset circuit	1.97
DS1374C	1	RTC	6.97
MV57124A	4	LED Red	0.88
XOSM-533 50M	1	Silicon oscillator	1.6
LT1763-3.3	1	LDO 3.3V 0.5A	4.13
PCB	1	PCB fabrication (Advanced Circuits)	37
A9020265, A9210290	1	Enclosure and non-slip fit (OKW)	2.5
Total:			192.59

Table C.3 presents the hours spent to design and build five Node devices and one Base device. This also includes time for the first prototype design (Node rev. A, B, C and Base rev. A, B), time spent on analysis, calculations, adjustments and various tests. Time spent for

documentation is not included because this thesis work is a final document for the WHM project.

Table C.3. Engineer work cost (based on fixed payment rate of $15/hour).

Job	Hours	Brief description	Cost, $
Requirements	30	Project requirements definition	450
Components definition	65	Selecting components, initial prototyping	975
Schematic design	140	Schematic entry and simulations	2100
PCB design	180	Circuit layout and verification, DRC	2700
Prototype assembly	50	Hand soldering and assembly procedures	750
Firmware design	160	Algorithms and MCU firmware coding	2400
Web design	40	Web GUI design	600
Node enclosure design	15	Solid design and air flow simulations	225
Sensor calibration	5	CO_2 and O_2 sensor calibration	75
Field test	15	System test under certain conditions	225
Total:			10500

Summarizing the above expenses, total cost of the whole project is $14,762.